ITER Relevant Runaway Electron Studies in the FTU Tokamak

by

Žana Popović

A dissertation submitted in partial fulfilment of the
requirements for the degree of
Doctor of Philosophy in

Plasmas y Fusión Nuclear

Universidad Carlos III de Madrid

Directors:

Prof Dr José Ramón Martín Solís
Dr Basilio Esposito

Tutor:

Prof Dr José Ramón Martín Solís

July 2019

Dedication

To my family,

VVBM

Acknowledgements

I would like to thank an exceptional man, my thesis director and supervisor Prof José Ramón Martín Solís. I have been lucky to be his student and am very grateful for all the help and caring guidance he has given me, for his patience and organisation throughout this work, especially during one of the most challenging years I have had. I appreciate immensely his expertise and dedication to teaching, which made this thesis possible. I would also like to thank my thesis co-director, Dr Basilio Esposito, for the invaluable mentoring and direction over the years, and for the delightful hospitality he and his family provided during my research visits in Frascati.

Many thanks to the people I collaborated with as a part of the FTU team at ENEA Research Centre, especially Drs Daniele Carnevale, Daniele Marocco, Federica Causa and Mateusz Gospodarczyk, as well as the other members of the FTU team and supporting staff for creating a stimulating and cheerful work environment during long experiments.

This journey was filled with interesting times spent with the people from the Department of Physics at Universidad Carlos III de Madrid. I appreciate the atmosphere created by my colleagues from the office - despacho and all the professors who made me feel as a part of their wonderful community, always with their doors open for me. I am particularly grateful for great advice and support from our Director, Prof Luís Raúl Sánchez Fernández, as well as the members of the Plasma group for constructive counsel they offered and motivating talks they organised. Also, special thanks to the Physics Laboratory coordinators, as well as the technicians Domingo and Josué, for their assistance and good spirit during my lab sessions with students.

I would like to thank Profs Milorad Kuraica, Maja Burić and Jovan Puzović, from the Faculty of Physics of Belgrade University, for being extraordinary teachers and enabling me to start on this path years ago. I am grateful

to Associate Research Prof Zoran Simić from the Astronomical Observatory of Belgrade and Dr Mihailo Martinović for their support and advice.

Above all, I would like to thank my loving parents Živko and Ljiljana and my brother Goran, for their incessant encouragement and belief in me, regardless of the physical distance and all it brings. Your love, goodness and playfulness carries and inspires me every day. I am blessed to have you. This accomplishment is yours as much as it is mine. Hvala vam.

Published and Submitted Content

Articles or other contributions (co)-authored by the Doctoral candidate that are included as part of the thesis and that have been published:

- G. Pucella et al., "Overview of the FTU results" (FTU Team and collaborators; includes Z. Popovic as a collaborator), *Nucl. Fusion* **55** *(2015) 104005*

  https://doi.org/10.1088/0029-5515/55/10/104005

- Z. Popovic, B. Esposito, J.R. Martín-Solís et al., "On the measurement of the threshold electric field for runaway electron generation in the Frascati Tokamak Upgrade", *Phys.Plasmas* **23** *(2016) 122501*

  https://doi.org/10.1063/1.4968839

- G. Pucella et al. (FTU Team and collaborators; includes Z. Popovic as a collaborator), "Overview of the FTU results", *Nucl. Fusion* **57** *(2017) 102004*

  https://doi.org/10.1088/1741-4326/aa6239

  These items are partly included in Chapter 4 and are mentioned in the introduction of the chapter. The material from these sources that is included in this thesis has not been singled out with typographic means; appropriate references are made. Reproduced here with permission of the copyright owners, AIP Publishing and Institute of Physics (IOP) Publishing Ltd.

- B. Esposito, L. Boncagni, P. Buratti, D. Carnevale, F. Causa, M. Gospodarczyk, J.R. Martin-Solis, Z. Popovic et al., "Runaway electron

generation and control", *Plasma Phys. Controll. Fusion* **59** *(2017) 014044*

https://doi.org/10.1088/0741-3335/59/1/014044

- D. Carnevale et al. (EUROfusion MST1 Team, includes Z. Popovic as a collaborator), "Runaway electron beam control", *Plasma Phys. Controll. Fusion* **61** *(2019) 014036*

  https://doi.org/10.1088/1361-6587/aaef53

  These items are partly included in Chapters 3, 4 and 5 and are mentioned in the introduction of the chapters. The material from these sources that is included in this thesis has not been singled out with typographic means; appropriate references are made. Reproduced here with permission of the copyright owners, Institute of Physics (IOP) Publishing Ltd.

Articles or other contributions (co)-authored by the Doctoral candidate that are included as part of the thesis and that have been submitted for publication:

- F. Causa et al. (includes Z. Popovic as a collaborator), "Runaway Electron Imaging Spectrometry (REIS) system", *submitted to Rev. Sci. Instrum. (2019)*

  This item is partly included in Chapter 3 and is mentioned in the introduction of the chapter. The material from this source that is included in this thesis has not been singled out with typographic means; appropriate references are made.

Abstract

Disruptions represent a serious danger for the operation of future magnetic confinement fusion devices based on the tokamak concept, as the international ITER (International Thermonuclear Experimental Reactor) project, currently under construction in Cadarache (France). During a disruption, a violent instability occurs that causes a sudden loss (in characteristic times of milliseconds) of the plasma energy and current. As a consequence, large heat loads and electromagnetic forces take place on the first wall components and device structures that can seriously limit its lifetime. Besides, during disruptions, large electric fields are produced that can lead to the generation and acceleration of a fraction of the plasma electrons to very high energies (up to tens or hundreds of MeV): the **runaway electrons**. The interaction of these energetic electrons with the first wall components can cause severe damage and even oblige to a temporary stop of the tokamak operation. Thereby, controlling and mitigating the effects associated with the disruptions and, in particular, with the runaway electrons constitutes currently one of the critical areas of research in magnetic confinement fusion with views to the future ITER project.

This doctoral thesis includes a collection of studies on runaway electrons carried out in the FTU (Frascati Tokamak Upgrade) tokamak in Frascati (Rome), a medium sized tokamak whose high magnetic field and density make it especially adequate to make extrapolations for ITER. The work is the result of collaborations with the FTU tokamak team within the framework of the european EUROFUSION projects, WP14-MST2-9, WP15-MST2-15 ("Runaway Electron Studies in FTU"; 2014 - 2016), WP18-MST2-15 ("REIS activities"; 2018), MST1-2017 and MST1-2018 ("Medium Sized Tokamaks"; 2017 and 2018), as well as the national projects ENE2012-31753 ("ITER-relevant disruption and runaway electron studies"; 2013 - 2016) and ENE2015-66444-R ("Runaway electron generation, control and dissipation during disruptions:

implications for ITER"; 2016 - 2019), all of them oriented to ITER.

The thesis has been divided into three parts. The first part consists of two chapters introducing the basic concepts: the controlled thermonuclear fusion, the tokamak scheme, the ITER project, and the FTU tokamak on which the work has been performed (Chapter 1), and the Chapter 2 which introduces the basic ideas regarding the runaway electrons in tokamaks, including basic elements of runaway physics, in particular the critical electric field for runaway electron generation, to which a chapter on FTU results is devoted, the generation and energy dynamics of the runaway electrons, as well as the runaway electrons during disruptions.

The second part of the manuscript consists of three chapters in which the results related to the runaway electrons in the FTU tokamak are presented. The Chapter 3 introduces new diagnostic systems, recently installed and validated, for the detection of runaway electrons in FTU: the **Gamma camera**, for the detection of hard X-rays, that allows to obtain spatial and temporal information on the runaway electrons and their energy, and the cameras in visible and infrared spectrum (**REIS system: Runaway Electron Imaging and Spectrometry System**) that make possible to acquire images of the runaway beam in flight as well as information about their energy. Both systems are of great importance for an adequate description of the runaway electron dynamics in the experiment (as in Chapters 4 and 5). In this chapter the main characteristics of both systems are described, together with examples of their application in the FTU tokamak.

The Chapter 4 is dedicated to the experiments performed in the FTU tokamak on one of the basic parameters of the runaway physics: the **critical (threshold) electric field for runaway electron generation**. This critical field is the minimum electric field necessary to generate runaway electrons and is of great practical importance because it determines the minimum amount of impurities required to inject into the plasma to suppress and control the runaway electrons. The experiments carried out for the determination of the value of the critical electric field are described in this chapter and the measured values are compared with the theory. The results indicate that the measured values are always substantially larger than the predicted by the classical theory, which assumes that the runaway energy looses are dominated by the collisions, and that the increase in the observed value of the critical electric field is consistent with the losses of energy associated with

electron synchrotron radiation. This would mean that the amount of impurities that would be necessary to inject into the plasma in order to suppress the runaway electrons could be significantly lower than initially predicted based on the classical collisional theory.

Finally, the Chapter 5 presents a summary of the experiments performed in the FTU tokamak, in which we have collaborated, on the **active control of the runaway beam currents** formed during disruptions. The control of the runaway beam position, in order to avoid the interaction of runaway electrons with the tokamak structures, together with the current dissipation through a slow current ramp-down, currently represents one of the main schemes proposed for the control of the runaway current, alternative to the plasma impurity injection.

All the experimental work described in these three chapters has been done in collaboration with the staff of the FTU tokamak and included in all the cases: my participation in the design and planning of the experiments, set-up and validation of the diagnostic systems and data acquisition, the analyis and interpretation of the measurements, as well as the elaboration of databases.

Lastly, in the third part of the manuscript (Chapter 6), the conclusions and future lines of work are presented.

Resumen

Las disrupciones constituyen un serio peligro para la operación de dispositivos de fusión por confinamiento magnético tipo tokamak como el proyecto internacional ITER (International Thermonuclear Experimental Reactor) actualmente en construcción en Cadarache (Francia). Durante una disrupción se produce una violenta inestabilidad que da lugar a la pérdida súbita (en tiempos característicos de milisegundos) de la energía y la corriente del plasma. Como consecuencia, se crean grandes cargas de calor y fuerzas electromecánicas sobre las componentes de la primera pared y las estructuras del dispositivo que pueden limitar seriamente la integridad del mismo. Además, durante disrupciones, se producen grandes campos eléctricos que pueden dar lugar a la generación y aceleración a muy altas energías (hasta decenas o cientos de MeV) de una fracción de los electrones del plasma: los **electrones runaway**. La interacción de estos electrones energéticos con los elementos de la primera pared puede dañarlos severamente e incluso obligar a parar temporalmente la operación del tokamak. De este modo, controlar y mitigar los efectos asociados a las disrupciones y, en particular, a los electrones runaway constituyen en la actualidad una las áreas críticas de la investigación en fusión por confinamiento magnético con vistas al futuro proyecto ITER.

Esta tesis doctoral incluye un conjunto de estudios sobre electrones runaway realizados en el tokamak FTU (Frascati Tokamak Upgrade) en Frascati (Roma), una máquina de tamaño medio cuyo alto campo magnético y alta densidad la hacen especialmente adecuada para realizar extrapolaciones a ITER. El trabajo es el resultado de colaboraciones realizadas con el equipo del tokamak FTU dentro del marco de los proyectos europeos de EUROFUSION WP14-MST2-9, WP15-MST2-15 ("Runaway Electron Studies in FTU"; 2014 - 2016), WP18-MST2-15 ("REIS activities"; 2018), MST1-2017 y MST1-2018 ("Medium Sized Tokamaks"; 2017 y 2018), así como de los proyectos nacionales ENE2012-31753 ("Estudios sobre electrones runaway

y disrupciones relevantes para ITER"; 2013 - 2016) y ENE2015-66444-R ("Generación, control y disipación de electrones runaway durante disrupciones: implicaciones para ITER"; 2016 - 2019), todos ellos orientados a ITER.

La tesis se ha dividido en tres partes. La primera parte consta de dos capítulos de introducción a los conceptos básicos: la fusión termonuclear controlada, el esquema tokamak, el proyecto ITER, y el tokamak FTU sobre el que se desarrolla este trabajo (Capítulo 1), y el Capítulo 2 que introduce ideas básicas relativas a los electrones runaway en tokamaks, incluyendo elementos básicos de la física runaway, en particular el campo eléctrico crítico para la generación de electrones runaway, al que se dedicará posteriormente un capítulo de resultados en el tokamak FTU, la generación y dinámica en energía de los electrones runaway, así como los electrones runaway durante disrupciones.

La segunda parte de la memoria consta de tres capítulos en los que se presentan los resultados relativos a los electrones runaway en el tokamak FTU. El Capítulo 3 introduce nuevos sistemas de diagnóstico, recientemente instalados y validados, para la detección de electrones runaway en FTU: la Cámara gamma, para la detección de rayos X duros, que permite obtener información espacial y temporal sobre los electrones runaway y su energía, y las cámaras en la región del espectro visible e infrarrojo (sistema REIS: Runaway Electron Imaging and Spectrometry System) que hacen posible obtener imágenes del haz runaway así como información sobre su energía. Ambos sistemas son de gran importancia para una descripción adecuada de la dinámica de los electrones runaway en el experimento (como en los Capítulos 4 y 5). En este capítulo se describen las características principales de ambos sistemas así como ejemplos de aplicación en el tokamak FTU.

El Capítulo 4 está dedicado a los experimentos realizados en el tokamak FTU sobre uno de los parámetros básicos de la física runaway: el campo eléctrico crítico para la generación de electrones runaway. Dicho campo crítico es el campo eléctrico mínimo necesario para que se puedan generar electrones runaway y es de gran importancia práctica porque determina la cantidad mínima de impurezas que es necesario inyectar en el plasma para poder suprimir y controlar los electrones runaway. En este capítulo se describen los experimentos realizados para determinar el valor del campo eléctrico crítico y se comparan los valores medidos con la teoría. Los resul-

tados indican que los valores medidos son siempre sustancialmente mayores que los predichos por la teoría clásica, que supone que las pérdidas de energía de los electrones runaway están dominadas por las colisiones, y que dicho aumento en el valor del campo crítico es consistente con las pérdidas de energía de los electrones runaway asociadas a la radiación sincrotrón del electrón. Esto significaría que la cantidad de impurezas que sería necesario inyectar en el plasma para suprimir los electrones runaway podría ser significativamente menor que la predicha inicialmente sobre la base de la teoría clásica colisional.

Finalmente, el Capítulo 5 presenta un resumen de los experimentos realizados en el tokamak FTU, en los que hemos colaborado, sobre el **control activo de haces de corriente runaway** formados durante disrupciones. El control de la posición del haz runaway, para evitar la interacción de los electrones runaway con las estructuras, junto con una "suave caída" de la corriente para disiparla, constituye en la actualidad uno de los principales esquemas propuestos para el control de la corriente runaway alternativos a la inyección de impurezas en el plasma.

Todo el trabajo experimental descrito en estos tres capítulos ha sido realizado en colaboración con personal del tokamak FTU y ha incluido en todos los casos: mi participación en el diseño y planificación de los experimentos, la puesta a punto y validación de los sistemas de medida y adquisición de datos, el tratamiento e interpretación de las medidas realizadas, así como la elaboración de bases de datos.

Por último, en la tercera parte de la memoria (Capítulo 6) se presentan las conclusiones y líneas futuras de trabajo.

Contents

List of Figures

LIST OF FIGURES

Part I

Basic concepts

Chapter 1

Nuclear fusion. The FTU tokamak

"It is a profound and necessary truth that the deep things in science are not found because they are useful; they were found because it was possible to find them."

Julius Robert Oppenheimer

1.1 Nuclear fusion

The great human accomplishments over the past two centuries have created conditions for the average life expectancy to double and continue increasing, giving rise to the current world population of about 7.6 billion, projected to reach 9.8 billion by 2050 [1]. As a side effect, the energy demands of the growing population and rapidly developing societies are depleting traditional energy reserves and harming the environment. In search of alternatives to fossil fuels and nuclear fission as dominant sources of energy, the greatest potential for a long-term solution is in one of the most ordinary processes in the visible universe: the **thermonuclear fusion**.

Nuclear fusion is the process where two light nuclei combine to form a heavier one, the total mass of the final products slightly smaller than the total initial mass. The mass difference (Δm) is released as kinetic energy of the reaction products (E), transformed according to Einstein's law $E = (\Delta m) \cdot c^2$, where c denotes the speed of light in vacuum. In order for fusion to happen,

the two nuclei have to gain high enough kinetic energies to overcome the mutual coulomb repulsion. This is naturally taking place in stars, including our Sun, where the enormous gravitational pressure and extreme temperatures provide the conditions for fusion to occur. On Earth however, the pressures are significantly lower and to attain the necessary kinetic energies, the temperatures have to be ten times greater than in the centre of the sun, reaching $\sim$ 100 - 200 million degrees. At such high temperatures, matter is found in the state of **plasma**. Plasmas can be generally described as macroscopically neutral gases consisting of many interacting free electrons and ionised atoms or molecules, which exhibit collective behaviour due to long-range coulomb forces.

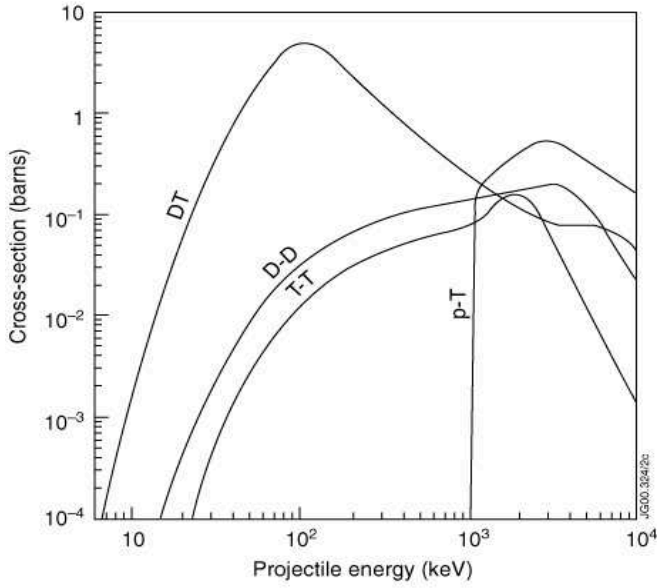

Figure 1.1: *Fusion reaction cross sections, in barns* ($1\,\text{barn} = 10^{-28}\,\text{m}^2$), *as a function of initial particle energy, in keV* ($1\,\text{keV} = 1.6021773 \times 10^{-16}\,\text{J}$). *Image from [2].*

In achieving controlled thermonuclear fusion, the basic problem is the generation and confinement of high temperature plasmas at large enough densities and for a long enough time to result in a substantial number of fusion reactions and energy. The main reaction that powers the sun is the fusion of hydrogen. As the lightest element with the lowest nuclear electric

charge, hydrogen requires the least energy to overcome the coulomb repulsion. Fig. 1.1 shows the cross-sections for several nuclear fusion reactions of the isotopes of hydrogen, as a function of the incident particle energy. The most favourable fusion reaction is that between deuterium (D) and tritium (T), yielding an alpha particle (^4_2He) and a high-energy neutron (n) according to:

$$D\ +\ T\ \longrightarrow\ {}^4_2H_e\,(3.5\,\mathrm{MeV})\ +\ n\,(14.1\,\mathrm{MeV}). \tag{1.1}$$

Controlled thermonuclear fusion of deuterium and tritium constitutes one of the most important application of man-made plasmas, due to its potential for the generation of energy. The energy released in $D-T$ fusion reactions is immense, about four million times greater than the energy released in chemical reactions such as the burning of coal, oil or gas. On the other hand, the fusion fuel is readily available: there is an abundance of renewable deuterium in sea water and the tritium required for the fusion reactions can be obtained from the earth's crust (Li) through the breeding reactions

$$\begin{aligned} {}^6Li + n\ &\longrightarrow\ \ T + {}^4_2H_e \\ {}^7Li + n\ &\longrightarrow\ \ T + {}^4_2H_e + n \end{aligned}$$

Together with the lack of long-lived radioactive residues or emission of greenhouse gasses into the atmosphere, this makes fusion an ideal long-term energy source for humanity.

1.2 The tokamak concept. The ITER project

The main criteria for the design of a fusion reactor are based upon reaching the requirements imposed on plasma density (n), temperature (T) and confinement time (τ_E), so that the burning process becomes self-sustaining (**ignition**). In order to keep the fusion reactor in such a state of ignition, it is necessary to generate more energy by fusion than is required to heat and confine the plasma, and to supply the energy lost by radiation and thermal conduction. To achieve this condition, the minimum value of the fusion triple product, $n\,\tau_E\,T$, should satisfy the Lawson criterion:

$$n\,\tau_E\,T \;>\; 5\times 10^{21}\,\mathrm{m}^{-3}\cdot\mathrm{s}\cdot\mathrm{keV}. \tag{1.2}$$

with $T\sim(10-20)\,\mathrm{keV}$ $(100-200$ million $^{\circ}\mathrm{C})$.

One of the most promising schemes to confine a thermonuclear fusion plasma consists of using magnetic fields (**magnetic confinement fusion**). The charged particles follow helical trajectories along the magnetic field lines, thus confining the plasma in the direction perpendicular to the field. The optimum magnetic configuration is the **toroidal configuration** in which the plasma is confined in a doughnut-shaped vacuum chamber by a toroidal magnetic field created by coils surrounding the vessel. Among the toroidal systems, the two leading types of devices in fusion research are the **tokamaks** and the **stellarators**. They differ in the approach taken to twist the magnetic field lines in a helical shape around the torus, which is required for a stable plasma equilibrium. In the stellarators, introduced in the 1950's by L. Spitzer, the twisting is produced by external helical conductors. Tokamaks were invented by I. Tamm and A. Sakharov in the 1950's and re-designed in the 1970's to meet the fusion conditions. They rely on internally produced confinement by transient, transformer currents, operating in a pulsed regime and constitute actually the magnetic confinement fusion device in which better results have been obtained to date.

The central phenomenon of interest for this thesis, the **electron runaway**, occurs mainly in tokamaks. Fig. 1.2 shows a schematic representation of a tokamak. The toroidal component of the magnetic field is produced by external coils around the vessel, while a toroidal current in the plasma, created by the transformer effect, yields a poloidal component of the magnetic field, resulting altogether in a helical magnetic field twisted along the

toroidal direction. Additional poloidal field coils that carry toroidal currents are used for plasma shaping, control of the plasma position, etc.

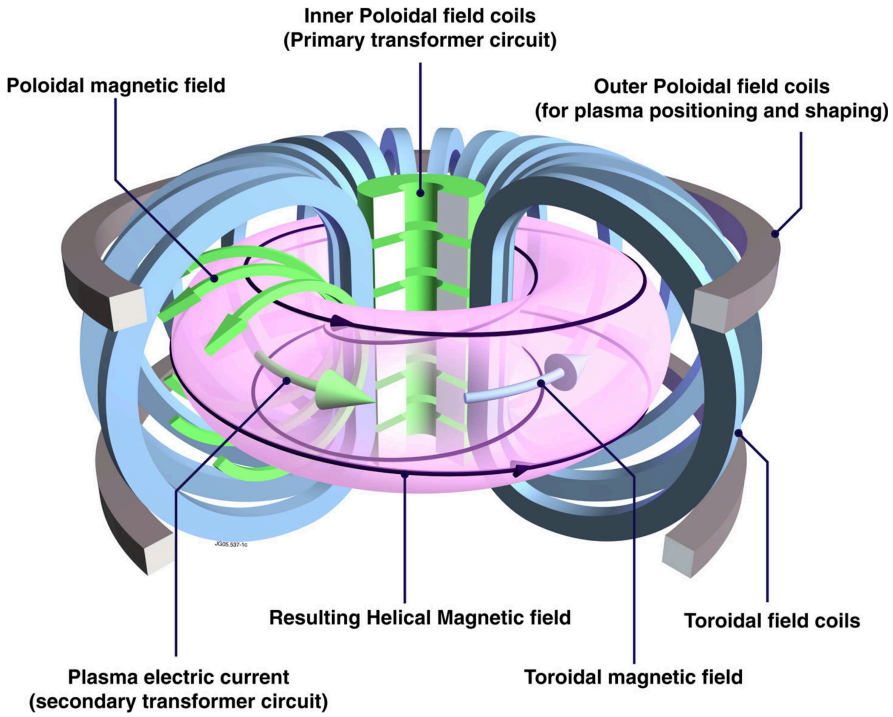

Figure 1.2: *Schematic representation of a tokamak. Figure taken from [2].*

Due to the pulsed, or transient nature of tokamak experiments, they are called **discharges**, **shots** or **pulses**. The evolution of a tokamak discharge consists of several stages, illustrated in Fig. 1.3: the **plasma current ramp-up** phase, when the plasma current increases due to the large initial voltage (electric field) associated with the transformer effect, the **current flat-top** phase, when the plasma reaches a steady state and the main energy production is taking place, and the **current ramp-down** phase, when no more flux change can be provided by the transformer and the current goes to zero.

Nowadays, based on the tokamak concept, the most ambitious fusion energy project is the ITER (*International Thermonuclear Experimental Reactor*) device (Fig. 1.4), a major international collaboration in fusion energy research involving the European Union (plus Switzerland), China, India, Japan, the Russian Federation, South Korea and the United States. It is

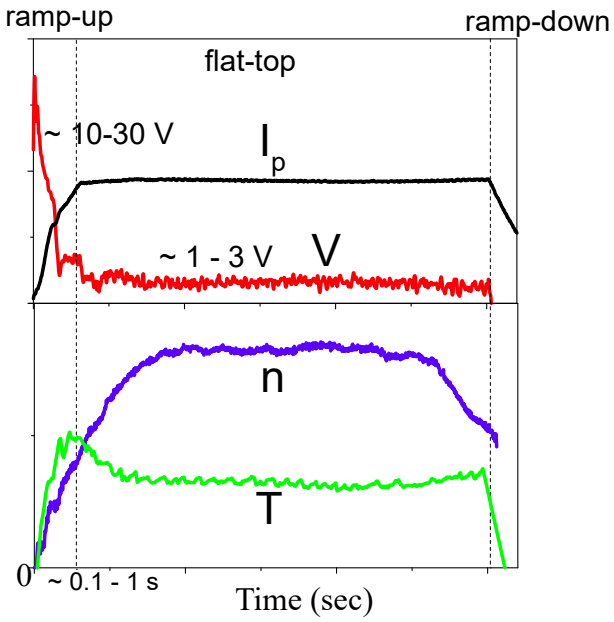

Figure 1.3: *Schematic of a tokamak discharge: Top: Time evolution of the plasma current and loop voltage; Bottom: Evolution of the central plasma density and temperature.*

currently under construction (Cadarache, France) and its overall programmatic objective is to demonstrate the scientific and technological feasibility of fusion energy for peaceful purposes. The principal goal is to design, construct and operate a tokamak experiment at a scale which satisfies this objective. ITER is designed to confine a DT plasma in which α-particle heating dominates all other forms of plasma heating. It is foreseen to obtain inductive plasmas with a power gain $Q > 10$ and operate in steady state with $Q = 5$. ITER is also aimed to demonstrate the integrated operation of the technologies for a fusion power plant, test the components required as well as the concepts for a tritium breeding module.

The main ITER design parameters are:

- Major radius: $R_0 = 6.2\,\mathrm{m}$;
- Minor radius: $a = 2.0\,\mathrm{m}$;

- Plasma current: $I_p = 15\,\mathrm{MA}$;
- Toroidal magnetic field: $B_t = 5.3\,\mathrm{T}$;
- Elongation/triangularity: $\kappa/\delta = 1.85/0.49$;
- Fusion power gain: $Q \geq 10$;
- Fusion power $\sim$ 400 MW;
- Plasma burn duration $\sim$ 400 s.

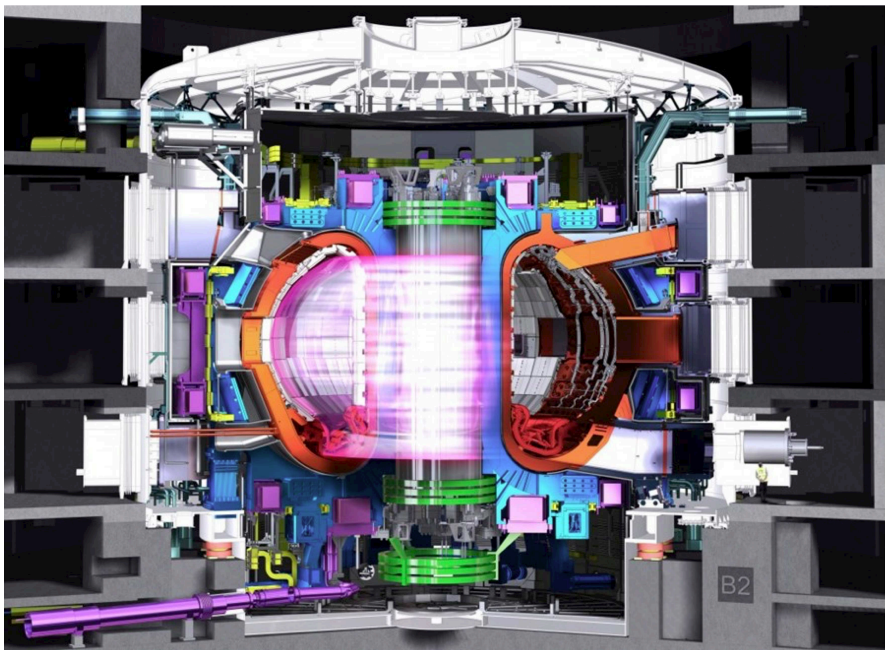

Figure 1.4: *ITER tokamak. First plasma expected by the year 2025. Image from [2].*

1.3 The FTU tokamak

The Frascati Tokamak Upgrade (FTU) is a medium-sized tokamak (MST) operating in Frascati, Italy. It is a compact tokamak (major radius $R_0 = 0.935\,\mathrm{m}$, minor radius $a = 0.30\,\mathrm{m}$) characterised by a high toroidal magnetic field (B_t up to 8 T) and high plasma density (central line averaged density up to $\sim 3 \times 10^{20}\,\mathrm{m}^{-3}$ in ohmic discharges) which began its operation in 1990.

FTU has a circular poloidal cross-section and operates in limiter configuration. All the FTU coils are made of copper and, in order to decrease the ohmic dissipation due to the Joule effect and, hence, avoid their damage, their resistivity is lowered by keeping them at the operating temperature of liquid nitrogen ($\sim 196°\mathrm{C}$).

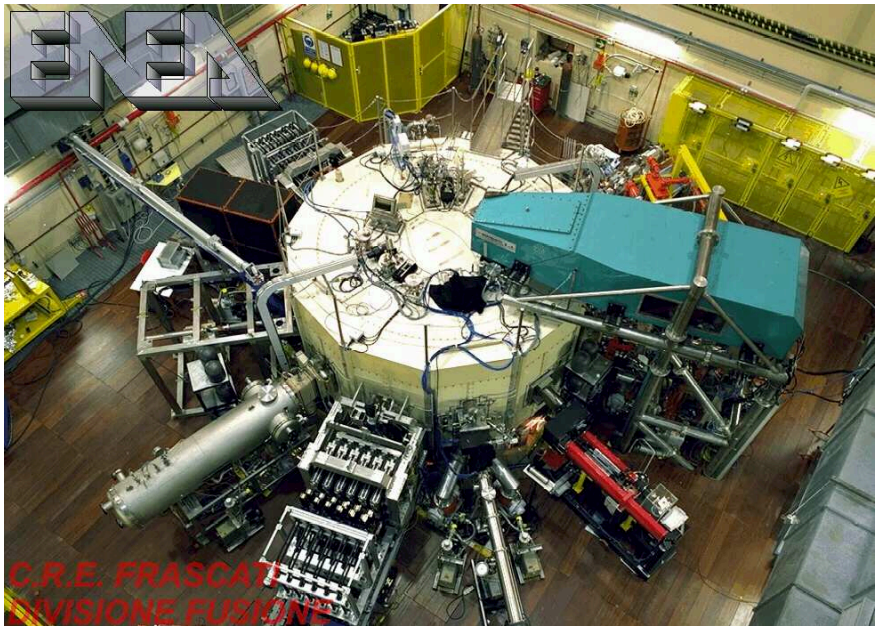

Figure 1.5: *Top view of the FTU vacuum chamber and diagnostic systems. Image from [3].*

The main FTU parameters are:

- Major radius: $R_0 = 0.935\,\mathrm{m}$;
- Minor radius: $a = 0.30\,\mathrm{m}$;

- Plasma current: $I_p < 1.6\,\mathrm{MA}$;
- Toroidal magnetic field: $B_t < 8\,\mathrm{T}$;
- Ohmic discharge duration ~ 1.7 s.

FTU has a long experience on runaway electron studies (the subject of this thesis), where the analysis of the runaway behaviour can be carried in conditions (plasma density and magnetic field) close to those expected in future reactor-relevant fusion experiments like ITER. The runaway electrons can be produced during the current ramp-up of the discharge, or be generated during disruptions. As a medium sized tokamak, the potential danger associated with the runaway electrons is smaller than in large devices, which makes FTU suitable for this kind of studies. Furthermore, FTU is equipped with a wide set of specific diagnostics for runaway electron measurements and several experimental campaigns have been devoted to runaway electron studies during the last years, addressing important ITER physics issues concerning the control and mitigation of runaway electrons [4].

CHAPTER 1. NUCLEAR FUSION. THE FTU TOKAMAK

Chapter 2

Runaway electrons in tokamak plasmas

"Our feeblest contemplations of the Cosmos stir us - there is a tingling in the spine, a catch in the voice, a faint sensation, as if a distant memory, of falling from a height."

Carl Sagan

2.1 The runaway phenomenon

The helical toroidal magnetic field configuration is essential for plasma confinement in tokamaks. As introduced in the previous chapter, it is the result of the magnetic fields created by the external toroidal field coils and the poloidal magnetic field due to the plasma current induced by the transformer effect in the device.

The presence of the toroidal electric field in the plasma creates the conditions for the phenomenon of **runaway electron** to occur. Because the electron Coulomb collision frequency decreases with increasing particle energy, electrons with energies greater than some critical value overcome the collisional drag force and are continuously accelerated by the electric field; namely, they "run away". This means that the runaway electrons gain more energy between each collision with the plasma particles than they lose in the

collision, thus speeding up to high energies, reaching energies of the order of tens or hundreds of MeV [5].

Electrons with such high energies might lose confinement and interact with the in-vessel elements, potentially yielding severe damage. This can be especially dangerous during tokamak disruptions, fast, dramatic events in which the plasma loses its stability. A disruption is characterised by a sudden loss of the plasma energy to the vacuum vessel wall, followed by a quick drop of the plasma temperature (it happens in less than 1 ms), leading to an increase in the plasma resistivity. As a consequence, at that instant, strong electric fields are induced inside the torus and the toroidal plasma current begins to fall rapidly. Whenever the electric field is sufficiently high, relativistic runaway electrons can be produced, occasionally carrying a significant kinetic energy. If they leave the plasma, they deposit the energy on the confining structures. The energy deposition by the runaways can be so large that it causes melting of the plasma facing components (PFC), or they can reach deep into the first wall materials of the vacuum vessel, damage the divertor and even cooling systems.

Historically, the runaway effect was first documented by Wilson (the inventor of the cloud chamber) in 1925 [6]. The phenomenon naturally occurs in atmospheric discharges (such as lightnings during a thunderstorms) and it is also observed and studied in astrophysical plasmas (for instance, solar flares) and solid state physics. In toroidal plasma devices, runaway electrons were originally detected in the 50's in plasma betatron experiments, where the strong applied electric fields promptly accelerated a high fraction of the plasma electrons to relativistic speeds. In tokamaks, they have been studied since the beginning of the research in this field [7].

The runaway phenomenon is particularly interesting and important in present-day tokamak fusion experiments, taking into account that the completion of a large tokamak such as ITER is in the foreseeable future. For a safe operation and control of the runaway population in next step devices like ITER, where the risk of massive runaway generation during disruptions is high, questions regarding the conditions that determine the formation of runaway beams during disruptions and their dynamics are of vital concern.

2.2 Runaway electron physics

2.2.1 Collisional friction. Critical velocity for runaway

For an initial consideration of the conditions for runaway, it can be said that the motion of an electron in a tokamak plasma is governed by two forces (Fig. 2.1). The electron is subject to the accelerating electric force due to the presence of the toroidal electric field ($E_{||}$), $F_e = eE_{||}$, and the friction force F_{coll}, due to the cumulative effect of the Coulomb collisions with the plasma ions and electrons.

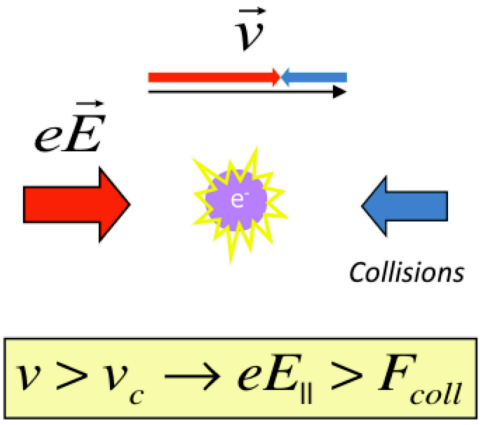

Figure 2.1: *Forces experienced by a runaway electron: accelerating force due to the electric field, and collisional friction force due to the Coulomb collisions with the plasma particles. For an electron to become runaway, the electric field acceleration must overcome the friction force.*

It can be shown that, in a non-relativistic case, for fast enough electrons, the friction force decreases with the particle energy and becomes inversely proportional to the square of its velocity ($\sim 1/v^2$) (Fig. 2.2). For the calculation of the collisional friction force, Coulomb collisions with the background thermal electrons and ions have to be considered. The force on an electron of velocity v and mass m_e, colliding with the background particles plasma j

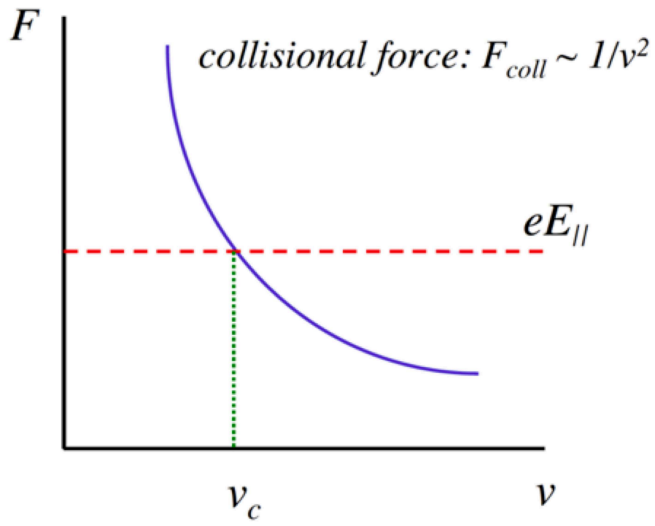

Figure 2.2: *Coulomb collisional drag force (or dynamical friction force) on a fast electron versus electron velocity. The critical velocity, v_c, is the minimum velocity at which the collisional friction force (full line) is balanced by the acceleration force due to the electric field (dashed line).*

(electrons and ions) is [8]:

$$\vec{F}_{ej}^{coll} = m_e \left\langle \frac{\Delta \vec{v}}{\Delta t} \right\rangle_{ej} = -A_{Dej}\, m_e \left(1 + \frac{m_e}{m_j}\right) \frac{\Psi(v/\sqrt{2}v_{Tj})}{2\, v_{Tj}^2} \frac{\vec{v}}{v}, \tag{2.1}$$

where the parameters, the thermal velocity of given species, v_{Tj}, and the error function, $\Phi(x)$, are defined by

$$\begin{aligned} A_{Dej} &\equiv \frac{n_j\, e^2\, q_j^2 \ln\Lambda_{ej}}{2\pi\, \varepsilon_0^2\, m_e^2}, & v_{Tj} &\equiv \left(\frac{T_j}{m_j}\right)^{1/2}, \\ \Psi(x) &\equiv \frac{\Phi(x) - x\Phi'(x)}{2x^2}, & \Phi(x) &\equiv \frac{2}{\sqrt{\pi}} \int_0^x e^{-x^2} dx. \end{aligned} \tag{2.2}$$

(n_j is the density of the species j, and q_j, T_j its charge and temperature, respectively; $\ln\Lambda_{ej}$ is the Coulomb logarithm for the collision of the electron with the species j, all of them of similar magnitude and that will assumed to be equal, $\ln\Lambda_{ej} = \ln\Lambda$).

For the purpose of this estimate, the collisions among runaways themselves can be neglected (as they are usually not too numerous), so that the expression for the friction force on the electron becomes:

$$\begin{aligned} F_e^{coll} &= F_{ee} + \sum_{ions} F_{ej} \\ &= \frac{n_e\, e^4 \ln\Lambda}{4\pi\, \varepsilon_0^2\, m_e} \left(\frac{2m_e}{T_e} \Psi(v/\sqrt{2}v_{Te}) + \sum_{ions} \frac{n_j Z_j^2}{n_e} \frac{m_j}{T_j} \Psi(v/\sqrt{2}v_{Tj}) \right). \end{aligned} \tag{2.3}$$

In the equation above, n_e is the electron density, e the electron charge, n_j the density of the ion species j, Z_j is the ion charge, m_j and T_j are the ion mass and temperature of that ion species, respectively, and ε_0 is the vacuum permittivity.

Now, considering velocities much greater than the thermal velocity, $v >> v_T$, the argument of the error function will be $x >> 1$, leading to $\Psi(x) \approx 1/2x^2$, which reduces the collisional force to

$$F_{coll} \approx \frac{n_e\, e^4 \ln\Lambda}{4\pi\varepsilon_0^2\, m_e} \frac{2 + Z_{eff}}{v^2} \propto \frac{1}{v^2}. \tag{2.4}$$

Here, $Zeff$ is the effective ion charge, defined as $Z_{eff} \equiv \sum_{ions} n_j Z_j^2 / n_e$.

Therefore, for a non-relativistic electron moving much faster than the thermal electrons, the collisional drag force is inversely proportional to the square of the electron velocity. An electron with a velocity larger than the critical velocity, v_c, at which the electric field force balances the collisional force ($F_e = F_{coll}$),

$$v_c = \sqrt{\frac{n_e\, e^3 \ln\Lambda\, (2 + Z_{eff})}{4\pi\varepsilon_0^2\, m_e\, E_{||}}}, \tag{2.5}$$

will be continuously accelerated and become a **runaway electron**.

Another parameter of interest in order to characterise the runaway phenomenon is the Dreicer field,

$$E_D = \frac{n_e\, e^3 \ln\Lambda}{4\pi\varepsilon_0^2\, T_e}, \tag{2.6}$$

which constitutes an estimate of the electric field required for thermal electrons to become runaways (note that if $E_{||} = E_D$ in Eq. (2.5), $v_c = (2 + Z_{eff})^{1/2}\, v_{Te} \sim v_{Te}$).

The Dreicer field is usually quite large, much larger, even during disruptions, than the plasma toroidal electric field.

2.2.2 Threshold electric field for runaway generation

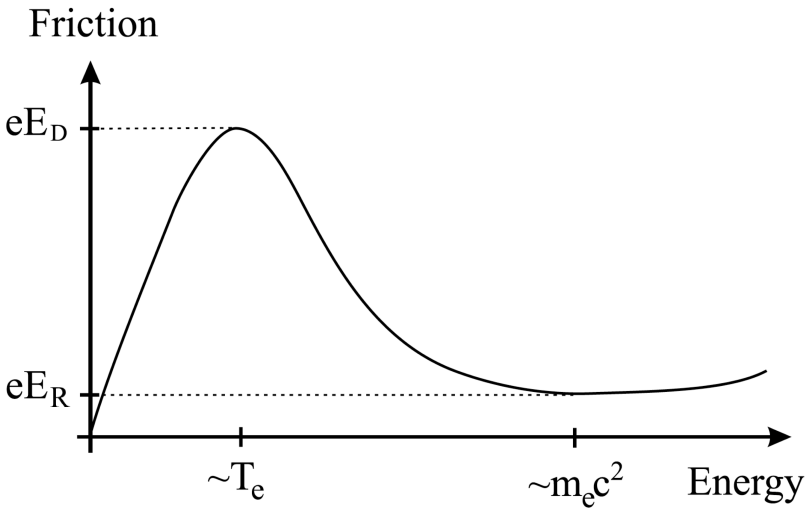

Figure 2.3: *Qualitative picture of the collisional friction force as a function of electron energy, including relativistic effects. Picture credit [9].*

For large enough electron energies, the calculation of the friction force must take into account relativistic effects [10]. As illustrated in Fig. 2.3, for energies of the order of the electron rest energy, $m_e c^2$, the collisional friction force does not decrease any further. It follows that the local minimum determines the minimum electric field required to generate runaway electrons, the so-called *critical or threshold electric field*, E_R. The value of the critical field is found when the critical velocity equals the speed of light, $v_c = c$ (as relativistically $v < c$), leading to [10]:

$$E_R = \frac{n_e\, e^3 \ln\Lambda}{4\pi\varepsilon_0^2\, m_e\, c^2}. \tag{2.7}$$

Below such a threshold field, absolutely no runaways can be found (if $E_{||} < E_R$, $v > c$ would be needed for electron acceleration). As the only experimentally controlled variable in Eq. (2.7) is the electron density n_e, sometimes the requirements for runaway generation are specified, for a given electric field, in terms of the critical electron density, above which runaway electrons cannot be found.

The critical field, E_R, can also be written in terms of the Dreicer field, E_D:

$$\frac{E_R}{E_D} = \frac{T_e}{m_e\, c^2}, \tag{2.8}$$

which shows that the Dreicer field is significantly larger than the critical field. Whereas the magnitude of the Dreicer field is never found in realistic tokamaks, during disruptions the induced parallel electric field is typically much larger than E_R, leading to a noticeable production of runaway electrons. In contrast, during the stationary phase of tokamak discharges, the toroidal electric field is much lower and, with the right selection of the plasma density, is rarely over the critical field so that few or no runaway electrons are generated.

2.3 Runaway generation mechanisms

The damage that the runaway electrons can cause depends to a great extent on their number. There are two basic mechanisms by which runaways can be generated:

- Primary or Dreicer generation [5]
- Secondary generation or avalanche mechanism [11]

When talking about the primary mechanism, it is usually referred to the Dreicer mechanism. Nevertheless, there are a few more that can also form a so-called *primary seed* in a runaway-free plasma, which will be mentioned later in this section. The total runaway growth rate (not taking into account the runaway losses) can be described by

$$\frac{\mathrm{d}n_r}{\mathrm{d}t} = \left(\frac{\mathrm{d}n_r}{\mathrm{d}t}\right)_{primary} + \left(\frac{\mathrm{d}n_r}{\mathrm{d}t}\right)_{avalanche}. \tag{2.9}$$

The plasma conditions will determine which mechanisms will be more likely to start and/or dominate the runaway production.

2.3.1 Dreicer mechanism

The Dreicer mechanism is based on the generation of runaway electrons by velocity space diffusion of electrons through the critical velocity (v_c) into the runaway domain, schematically represented in Fig. 2.4. The number of runaway electrons produced by this mechanism can be obtained by solving the Fokker-Planck kinetic equation, which gives the Dreicer runaway production rate:

$$\left(\frac{\mathrm{d}n_r}{\mathrm{d}t}\right)_{Dreicer} = n_e\,\nu_e\,\lambda, \tag{2.10}$$

where n_r is the runaway electron density, n_e is the plasma electron density, ν_e is the collision frequency for relativistic electrons

$$\nu_e = \frac{n_e\,e^4\ln\Lambda}{4\pi\varepsilon_0^2\,m_e^2\,c^3}, \tag{2.11}$$

and λ is the (relativistic) Dreicer birth rate factor [10] that can be expressed as:

$$\lambda = \left(\frac{m_e c^2}{2T_e}\right)^{3/2} \left(\frac{E_D}{E_{||}}\right)^{\frac{3(1+Z_{eff})}{16}} \exp\left(-\frac{E_D}{4E_{||}} - \sqrt{\frac{(1+Z_{eff})E_D}{E_{||}}}\right), \quad (2.12)$$

with Z_{eff} and E_D being the previously defined effective ion charge and the Dreicer field, respectively.

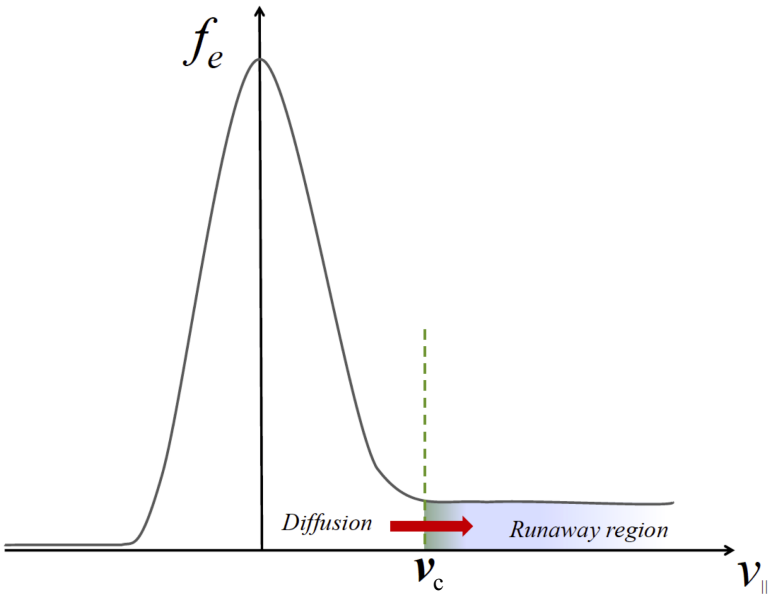

Figure 2.4: *Electron diffusion through the critical velocity (v_c) into the runaway region in velocity space. Figure reference [12].*

The Dreicer production increases exponentially with $\varepsilon \equiv E_{||}/E_D$ [13, 14]. As $E_D \equiv n_e\, e^3 \ln\Lambda/(4\pi\varepsilon_0^2 T_e)$ and $E_{||} = \eta\, j^2 \propto T_e^{-3/2} j^2$ (where η and j are the plasma resistivity and current density, respectively), it can be shown that $\varepsilon \propto 1/(n_e T_e^{1/2})$, which means that low density and cold plasma conditions promote runaway production by the Dreicer mechanism.

2.3.2 Secondary (avalanche) mechanism

Secondary runaway generation or avalanche mechanism is associated with large angle electron-electron scattering, where the existing runaway electrons transfer enough kinetic energy by close Coulomb collisions to the thermal plasma electrons which become runaways as well (Fig. 2.5) [11, 15].

The avalanche mechanism yields an exponential growth of the runaway population that can be estimated by

$$\left(\frac{\mathrm{d}n_r}{\mathrm{d}t}\right)_{avalanche} = \frac{n_r}{\tau_s}, \tag{2.13}$$

where τ_s is the characteristic avalanching time, which can be approximated as [15]:

$$\tau_s \approx \frac{4\pi\varepsilon_0^2\, m_e^2\, c^3}{e^4\, n_e}\sqrt{\frac{3(5+Z_{eff})}{\pi}}\left(\frac{E_{||}}{E_R}-1\right)^{-1}, \tag{2.14}$$

E_R being the critical electric field for runaway electron generation (Eq. (2.7)).

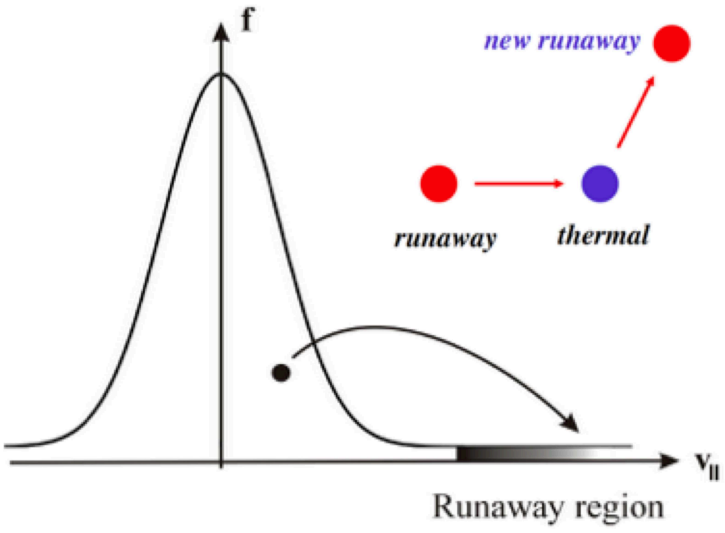

Figure 2.5: *The avalanche generation mechanism by "knock-on" collisions of runaway electrons with thermal plasma electrons. Figure reference [12].*

During disruptions, the importance of the avalanche mechanism increases with the plasma current since, in that case, the value of the electric field during the disruption is larger, which reduces the avalanching time, τ_s (Eq. (2.14)). It is expected that the secondary generation will play a fundamental role during disruptions in future fusion reactors [16].

2.3.3 Other runaway generation mechanisms

Hot-tail mechanism

Runaway generation by the hot-tail mechanism occurs during rapid plasma cooling [17] as during the thermal quench phase of a disruption (2.5). The thermalisation of the electron population during the rapid plasma drop depends on the electron energy, as the electron collision frequency decreases when the particle energy increases. This causes the high energy part of the electron distribution, with greater velocities, to remain at high energy for a longer time, creating a "hot tail" in the initial Maxwellian distribution. As the plasma keeps cooling down, the electric field increases and the critical velocity for runaway generation (v_c) decreases, enabling the hot-tail part of the electron population above the critical value to be accelerated by the rising electric field and run away. It is believed that the hot-tail generation mechanism might play an important role during fast thermal quenches during disruptions, when the plasma confinement is lost and the electron temperature can quickly (less than 1 ms) drop to very low values, $\sim$ eVs.

Tritium decay

During the DT phase of next step devices like ITER, tritium decay can provide a source of seed runaway electrons. The beta decay process, by which tritium decays into helium-3 with a half-life $\tau_T = (4500 \pm 8)$ days:

$$T \longrightarrow {}^{3}_{2}H_e + e^- + \overline{\nu}_e \tag{2.15}$$

produces along an electron (referred to as beta-electron) and an electron

antineutrino $\overline{\nu}_e$. The beta-electron breeding rate can be estimated as [18]

$$\left(\frac{\mathrm{d}n_\beta}{\mathrm{d}t}\right)_T = \lambda_T\, n_T = \ln 2\, \frac{n_T}{\tau_T}, \tag{2.16}$$

where n_T is the tritium density and $\lambda_T = \ln 2/\tau_T$ is the tritium disintegration rate constant. The primary runaway seed will only stem from the beta-electrons created with an energy greater than the critical runaway energy, E_c. Therefore, the tritium decay runaway production rate can be approximated by:

$$\left(\frac{\mathrm{d}n_r}{\mathrm{d}t}\right)_T \approx n_T\, \nu_T(E_c) = \ln 2\, \frac{n_T}{\tau_T}\, F_\beta(E_c), \tag{2.17}$$

where $\nu_T(E_c) = \ln 2\, F_\beta(E_c)/\tau_T$ and $F_\beta(E_c)$ is the fraction of the beta-electron energy spectrum ($f_\beta(E)$, normalised to one) that would become runaway

$$F_\beta(E_c) = \int_{E_c}^{E_{max}} f_\beta(E)\, \mathrm{d}E.$$

(E_{max} is the maximum of the beta-energy spectrum, $E_{max} = 18.6\,\mathrm{keV}$).

For ITER, when $E_c < E_{max}$, tritium decay could provide during disruptions a sufficiently strong seed leading, due to the avalanche amplification, to a substantial relativistic-electron current [18].

Compton scattering

In ITER, due to the high neutron production in the DT reactions, the wall activation can cause the emission of γ-rays with energies up to several MeVs. Compton scattering of the emitted γ-rays can lead to the formation of a runaway seed. The number of Compton scattered electrons by the γ-rays that become runaway can be predicted from [18]:

$$\left(\frac{\mathrm{d}n_r}{\mathrm{d}t}\right)_{Compton} = n_e \int \Gamma_\gamma(E_\gamma)\, \sigma(E_\gamma)\, \mathrm{d}E_\gamma. \tag{2.18}$$

In the equation above, E_γ is the emitted photon energy, $\Gamma_\gamma(E_\gamma)$ is the gamma energy flux spectrum (the shape of the spectra will depend on the configuration of the first wall and blanket), and $\sigma(E_\gamma)$ is the Compton scattering

cross-section for photons of energy E_γ (calculated for deflection angles over the critical angle for electron scattering with energy above the critical energy for runaway generation).

The gamma flux scales with the fusion power, and the Compton scattered electrons can take up to a few tens of milliseconds to lose their energy through collisions. During a disruption, if high gamma fluxes are present before the thermal quench, the initial runaway seed after the thermal quench can be dominated by the Compton scattered electrons, and so feed the avalanche mechanism [18].

2.4 Runaway energy dynamics

The detrimental effect of the runaway electrons when they interact with the wall structures depends on both their number and energy. In this section, we will focus on the runaway energy dynamics. The runaway electrons, accelerated by the toroidal electric field, speed up to high energies until the energy gain is balanced by the electron synchrotron radiation due to its curved path in the tokamak. The theoretical model given below describes the energy behaviour of a runaway electron in a tokamak determined by the balance of the electric field acceleration, the collisional friction and the synchrotron radiation losses [19]. The model allows to get simple estimates for the conditions for runaway including the effect of the radiation losses as well as the energy that the runaway electrons can reach, that will be applied in the following chapters to the analysis of the runaway electron dynamics in the FTU tokamak.

2.4.1 Test particle model

The dynamics of a relativistic electron in a tokamak plasma is often described by the kinetic Fokker-Planck equation [13, 20]. Its solution can be numerically heavy and for a simpler estimate of the runaway electron energy, the test particle analysis in phase-space [19, 21, 22] can be more suitable.

In this thesis, a test particle approach, introduced in Ref. [19], which characterises the dynamics of relativistic electrons in momentum space, including the acceleration in the toroidal electric field, collisions with the plasma particles, and the deceleration due to synchrotron radiation losses, will be used. In this section, several important conclusions from this model will be presented.

In the model, the evolution of a relativistic electron (absolute charge e and mass m_e) inside a tokamak plasma of electron density n_e, is described using the single particle relaxation equations [19]:

$$\frac{\mathrm{d}p_{||}}{\mathrm{d}t} = eE_{||} - \frac{n_e\, e^4 \ln\Lambda\, m_e}{4\pi\, \varepsilon_0^2}\, \gamma\, (Z_{eff} + 1 + \gamma)\, \frac{p_{||}}{p^3} - F_S\, \frac{p_{||}}{p}, \tag{2.19}$$

$$\frac{\mathrm{d}p}{\mathrm{d}t} = eE_{||}\, \frac{p_{||}}{p} - \frac{n_e\, e^4 \ln\Lambda\, m_e}{4\pi\, \varepsilon_0^2}\, \frac{\gamma^2}{p^2} - F_S, \tag{2.20}$$

where $p_{||}$ is the electron momentum component parallel to the magnetic field,

p is the total electron momentum, $E_{||}$ is the toroidal electric field, $\ln\Lambda$ is the Coulomb logarithm, γ is the relativistic gamma factor, $\gamma^2 = 1 + p^2/(m_e c)^2$ [electron kinetic energy, $E = (\gamma - 1)\, m_e c^2$], and Z_{eff} is the effective ion charge.

On the right hand side of the Eqs. (2.19) and (2.20), the first term is the acceleration due to the toroidal electric field, the second term includes the effects of collisions with the plasma ions and electrons [23], and the last term in both equations represents the losses associated to the synchrotron radiation emission by the electron moving around the tokamak. The synchrotron radiation is one of the most important mechanisms that limit the energy of the runaway electrons. In the equations above, it is characterised by the radiation reaction force [24], F_S, which is assumed to be parallel to the electron velocity vector and is approximated by

$$F_S \simeq \frac{2}{3}\, r_e\, m_e\, c^2 \left(\frac{v}{c}\right)^3 \gamma^4 \left\langle \frac{1}{R^2} \right\rangle, \tag{2.21}$$

where $r_e = e^2/(4\pi\varepsilon_0 m_e c^2)$ is the classical electron radius, v the electron velocity, $v/c = (\gamma^2 - 1)^{1/2}/\gamma$, with the radius of curvature averaged over one gyrorotation approximated by [25, 19]

$$\left\langle \frac{1}{R^2} \right\rangle \simeq \frac{1}{R_0^2} + \frac{\sin^4\theta}{r_g^2}. \tag{2.22}$$

Here, R_0 is the plasma major radius, θ the pitch angle, and r_g is the electron gyroradius (Larmor radius), $r_g \equiv p_\perp/eB_0$, where $p_\perp$ is the electron momentum perpendicular to the toroidal magnetic field B_0.

The first term in the Eq. (2.22) is primarily determined by the guiding centre motion and the second term by the electron gyromotion. Considering that $r_g \ll R_0$, the last term dominates when the pitch angles are finite, and thus the radius of curvature is determined by the electron gyration. The contribution from the guiding centre motion is significant only when θ is close to zero. Thus, the decelerating radiation force finally comes to

$$F_S \simeq \frac{2}{3}\, r_e\, m_e\, c^2 \left(\frac{v}{c}\right)^3 \gamma^4 \left(\frac{1}{R_0^2} + \frac{\sin^4\theta}{r_g^2}\right). \tag{2.23}$$

Even though better approximations for the decelerating radiation force ex-

ist [26], without assuming $\vec{F_S} \parallel \vec{v}$, it has been shown in Ref. [27] that the estimate (2.23) proves to be a sufficiently good approximation for the analysis of the generation conditions and the limiting energy of runaway electrons.

It is useful to rewrite Eqs. (2.19) and (2.20) in normalised form using the normalised electron momentum $q = p/m_e c$, defining a normalised time $\tau \equiv \nu_r\, t$, with $\nu_r = n_e e^4 \ln\Lambda/(4\pi\varepsilon_0^2 m_e^2 c^3)$, a normalised electric field $D = E_{||}/E_R$, where E_R is the critical field for runaway generation defined in Sec. 2.2.2 (Eq. 2.7), and the parameters $\alpha = 1 + Z_{eff}$, $F_{gc} = F_{gy}(m_e c/eB_0R_0)^2$, and $F_{gy} = 2\varepsilon_0 B_0^2/3n_e \ln\Lambda m_e$, where F_{gc} and F_{gy} describe the two contributions to the radiation losses coming from the guiding centre motion and the electron gyromotion, respectively. The resulting normalised test particle equations are:

$$\frac{\mathrm{d}q_{||}}{\mathrm{d}\tau} = D - \gamma\,(\alpha+\gamma)\,\frac{q_{||}}{q^3} - \left(F_{gc} + F_{gy}\,\frac{q_\perp^2}{q^4}\right)\gamma^4\left(\frac{v}{c}\right)^3\frac{q_{||}}{q} \qquad (2.24)$$

$$\frac{\mathrm{d}q}{\mathrm{d}\tau} = D\frac{q_{||}}{q} - \frac{\gamma^2}{q^2} - \left(F_{gc} + F_{gy}\frac{q_\perp^2}{q^4}\right)\gamma^4\left(\frac{v}{c}\right)^3 q_\perp^2, \qquad (2.25)$$

where $q_{||}$, $q_\perp$ and q are the normalised parallel, perpendicular and total electron momenta, respectively.

Combining Eqs. (2.24) and (2.25), the equation for the perpendicular momentum is recovered:

$$q_\perp\frac{\mathrm{d}q_\perp}{\mathrm{d}\tau} = \frac{1}{q}\left[\gamma\,(\alpha+\gamma)\,\frac{q_{||}^2}{q^2} - \gamma^2 - \left(F_{gc} + F_{gy}\frac{q_\perp^2}{q^4}\right)\gamma^4\left(\frac{v}{c}\right)^3 q_\perp^2\right]. \qquad (2.26)$$

The system of Eqs. (2.24) and (2.26) describes the test electron trajectories in momentum space $(\,q_{||},\, q_\perp^2)$, which is characterised by two singular points: a saddle point, P_1, and a stable focus, P_2 (see Fig. 2.6). Considering that P_1 and P_2 lie at the intersection of the contours $\dot{q_{||}} = 0$ and $\dot{q_\perp} = 0$ (or $\dot{q} = 0$), an analytic relation between the normalised electric field, D, and the singular points can be found. Hence, setting $\dot{q} = 0$, an implicit equation for the relativistic gamma factor at the singular points, γ_s, can be obtained from Eq. (2.25),

$$D = \frac{\gamma_s^2}{\cos\theta_s(\gamma_s^2-1)} \times \left(1 + F_{gy}\frac{(\gamma_s^2-1)^{3/2}}{\gamma_s}\sin^2\theta_s + F_{gc}\frac{(\gamma_s^2-1)^{5/2}}{\gamma_s}\right), \qquad (2.27)$$

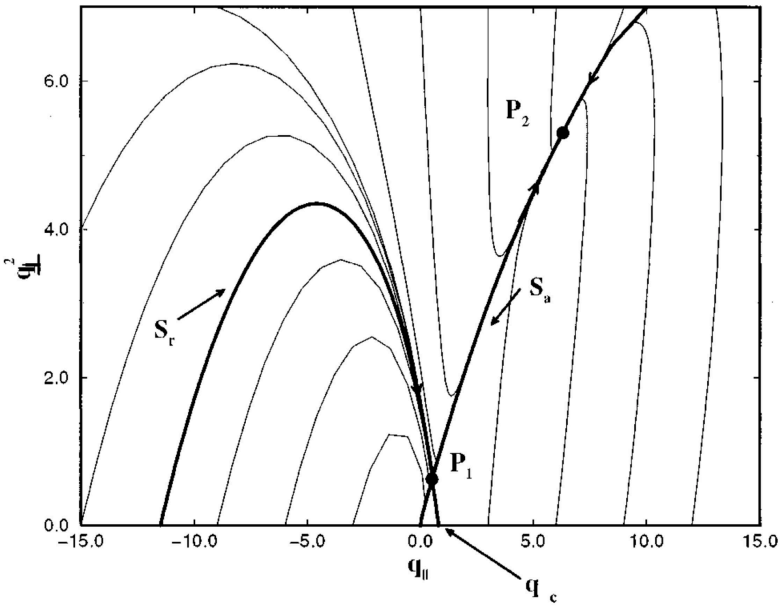

Figure 2.6: *Test electron trajectories (Eqs. (2.24) and (2.26) in* $(q_{||}, q_{\perp}^2)$ *space, for* $D = 4.4$, $\alpha = 4, F_{gy} = 0.65,$ *and* $F_{gc} = 2.3\times10^{-8}$. *The saddle point is* P_1, *and the stable focus* P_2, S_r *and* S_a *are the separatrices, and* q_c *is the normalised critical momentum for runaway electron generation (reproduced from Ref. [19]).*

with the pitch angle at the singular points, θ_s, found from Eq. (2.26) setting $\dot{q_{\perp}} = 0$,

$$\begin{aligned}\cos^2\theta_s \;=& 1 + \frac{F_{gc}(\gamma_s^2-1)}{2F_{gy}} + \frac{\alpha+\gamma_s}{2F_{gy}(\gamma_s^2-1)^{3/2}} \\ &\times\left\{1 - \left[\frac{4\alpha F_{gy}(\gamma_s^2-1)^{3/2}}{(\alpha+\gamma_s)^2} + \left(1+\frac{F_{gc}(\gamma_s^2-1)^{5/2}}{\alpha+\gamma_s}\right)^2\right]^{1/2}\right\}.\end{aligned} \tag{2.28}$$

As a result of the direct relation between γ and the electron energy, $E = (\gamma-1)m_e c^2$, the relativistic gamma factor is sometimes referred to as the electron energy. The plot in Fig. 2.7 shows the dependence of D on γ_s, calculated for a specific set of parameters ($\alpha = 4$, $F_{gy} = 0.65$) using Eqs. (2.27) and (2.28). For a given value of the normalised electric field,

there are two solutions for γ_s, that correspond to the singular points P_1 and P_2: γ_s at the saddle point P_1 corresponds the branch I in the figure, while the branch II gives γ_s at the stable focus P_2. The two branches join at the minimum of D over γ_s (defined by $\mathrm{d}D/\mathrm{d}\gamma_s = 0$). The physical meaning of the two singular points is well known: the saddle point provides the critical energy for runaway generation, and the stable focus the energy limit for the generated runaway electrons [19].

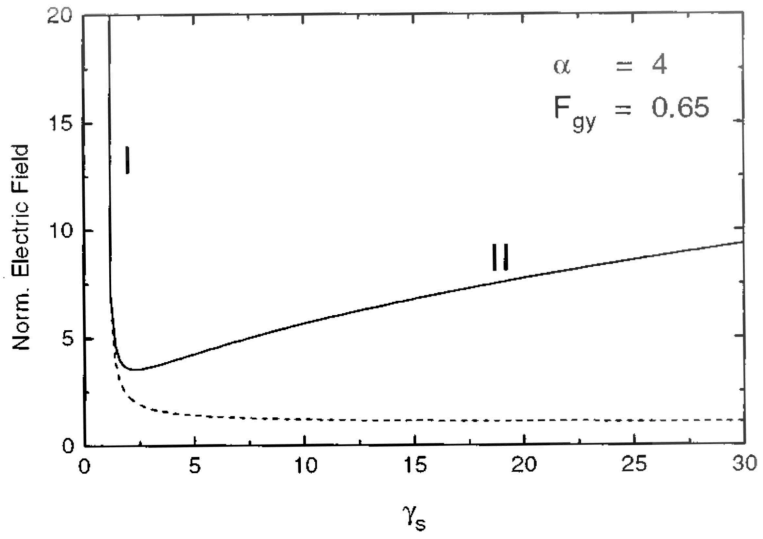

Figure 2.7: *Dependence of the normalised electric field D on the electron energy γ_s, including the energy losses due to the electron synchrotron radiation (full line), and omitting the power radiated by the electron (dashed line). Source [19].*

Outlined in Fig. 2.6 are the limiting particle trajectories, the separatrices S_r and S_a passing through P_1 and P_2. The separatrix S_r divides the phase space $(q_{||}, q_{\perp}^2)$ in runaway and non-runaway regions. Outside S_r is the runaway region, meaning that all the electrons found inside eventually move along the separatrix S_a towards the stable focus P_2, while electrons initially inside S_r will finally collapse into the origin, becoming thermal electrons.

It should be remarked that the stable point P_2 is the result of including the radiation in the test particle model. The runaway electrons, outside S_r,

are not perpetually accelerated but will finally reach a maximum energy at P_2 when the electric field acceleration is balanced by the electron synchrotron radiation losses. In the absence of radiative losses, the test equations would show only one singular point in momentum space, the saddle point P_1. Its location can be obtained by setting $F_S = 0$ and $\dot{q_{||}} = 0$, $\dot{q_{\perp}} = 0$ (dashed line in Fig. 2.7),

$$D = \frac{\gamma_s^{3/2}(\alpha + \gamma_s)^{1/2}}{\gamma_s^2 - 1}. \tag{2.29}$$

In such a case, there would be only one branch (dashed line Fig. 2.7) that corresponds to the saddle point, extending to infinity in γ_s when $D \Longrightarrow 1$ ($E_{||} = E_R$).

2.4.2 Critical electric field and synchrotron radiation losses

Connor and Hastie [10] introduced relativistic effects in a kinetic description of the runaway dynamics including the effect of the electric field and the collisions, and revealed the existence of a critical electric field, $E_R = n_e\, e^3 \ln\Lambda/(4\pi\varepsilon_0^2\, m_e\, c^2)$ (or $D_R = 1$), below which runaway generation ceases. The same result was obtained by Fussmann [22] by a test particle approach in the absence of the radiative energy losses (Sec. 2.2.2).

If the synchrotron radiation losses are included, along with the influence of the electric field and collisions with the plasma particles considered in Ref. [10], the value of the critical electric field increases. This change can be quantified using the test particle approach [19] presented above. As illustrated in Fig. 2.7, a local minimum separates the branch I with saddle points from the branch II with stable focus points. When D is decreasing in the vicinity of the local minimum, the value of γ_s at the saddle point increases, meanwhile its value at the stable focus decreases, right until they coalesce at the minimum of D over γ_s. Beneath this minimum, there are not singular points in momentum space, i.e., there are no runaway electrons.

It follows that the normalised threshold electric field for runaway electron generation, D_R, can be found as the minimum of D versus γ_s, that is, from the condition $\mathrm{d}D/\mathrm{d}\gamma_s = 0$. The resulting normalised critical electric field, D_R, as a function of the electron radiation parameter, F_{gy}, is shown in Fig. 2.8.

Its value is greater than one ($D_R > 1$) due to the synchrotron radiation, and increases with the radiation parameter F_{gy}. The classical result $D_R = 1$ (critical electric field equal to E_R), from Refs. [22, 10], is recovered when the radiation losses are neglected (by setting $F_{gy} = 0$). When $F_{gy} > 0$, the momentum and energy losses intensify due to the radiated power, leading to more restrictive conditions for runaway, and hence, to the increase in the value of the threshold electric field for runaway generation in comparison to the estimate excluding radiation ($D_R > 1$, i.e., critical electric field larger than E_R) [19].

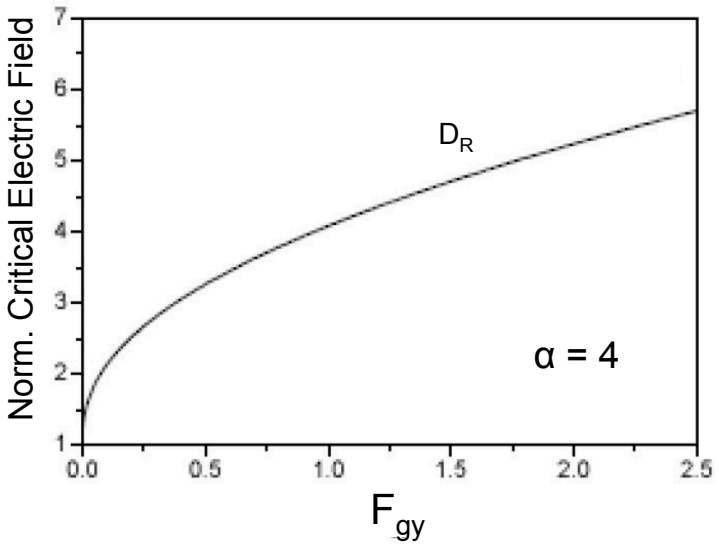

Figure 2.8: *Normalised critical electric field for runaway generation, D_R, as a function of the radiation parameter, F_{gy} (from [19]).*

The increase in the value of the critical electric field associated to the effect of the synchrotron radiation losses has been verified experimentally in the FTU tokamak [28]. During the experiments, runaway suppression during ECRH (*Electron Cyclotron Resonance Heating*) was found to occur at electric fields substantially larger than E_R, and consistent with an increase of the threshold electric field due to electron synchrotron radiation.

In Ref. [28], an empirical fitting to the calculated critical electric field including synchrotron radiation effects, E_R^{rad}, using the test particle model, suitable for the comparison with the experiment, was obtained,

$$\frac{E_R^{rad}}{E_R} \cong 1 + C(Z_{eff})\, F_{gy}^{\alpha}, \tag{2.30}$$

where $C(Z_{eff}) \cong 1.64 + 0.53\, Z_{eff} - 0.015\, Z_{eff}^2$, and $\alpha = 0.45 \pm 0.03$. This scaling law for E_R^{rad} is compared in Fig. 2.9 with results in FTU corresponding to runaway suppression experiments during ECRH and LHCD *Lower Hybrid Current Drive*), and to the observation of runaway electrons during FTU ohmic (OH) discharges. In particular, it is observed that runaway electron suppression during ECRH (open circles in the figure) can be found for values of the electric field substantially larger than the Connor collisional threshold (horizontal line), E_R, and close to the radiation threshold line corresponding to E_R^{rad}. Furthermore, no runaway electrons are observed below E_R^{rad}, indicating that the critical field including the effect of the electron synchrotron radiation, E_R^{rad}, constitutes an effective threshold electric field value for runaway electrons in FTU.

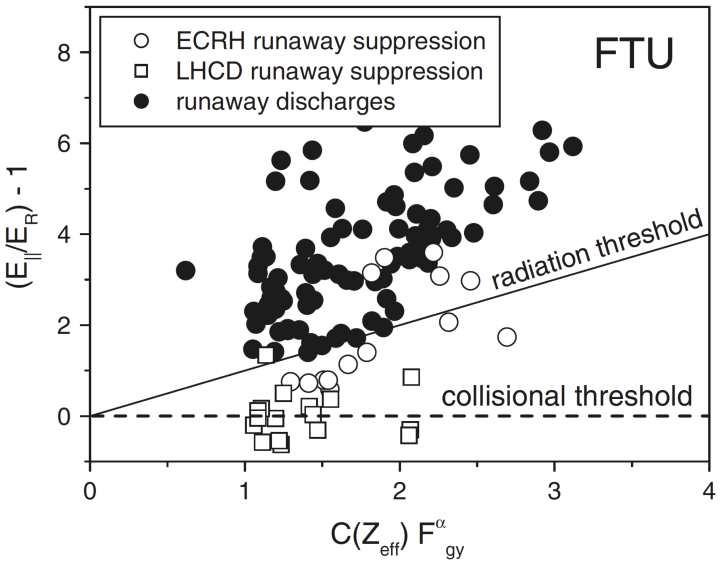

Figure 2.9: *$E_{||}/E_R^{rad} - 1$ versus $C(Z_{eff})\, F_{gy}^{\alpha}$ for FTU runaway suppression experiments during ECRH (open circles) and LHCD (open squares), and corresponding to the observation of runaway electrons during FTU OH discharges (full circles). The predicted radiation and collision threshold electric fields, E_R^{rad} and E_R, are indicated by the full and dashed lines, respectively.*

2.4.3 Critical momentum

The separatrix S_r, highlighted in Fig. 2.6 (Sec. 2.4.1), separates the region in momentum space where runaway generation is taking place. Nevertheless, a simpler criterion (as pointed out by Fuchs et al. [21]) for runaway generation can be obtained by realising that nearly all the electrons must be oriented in the direction of the electric field force. Consequently, the condition for runaway can be reduced to $q_{||} > q_c$, where q_c is the intersection of the separatrix with the positive $q_{||}$ axis and can then be referred to as the critical (normalised) momentum for runaway generation. The value of q_c can be derived as in the non-radiative approach from Ref. [21]: the critical runaway energy and momentum, γ_c and q_c, can be fairly approximated by those at the saddle point P_1. Thus, γ_c will be given by branch I in Fig. 2.7 (Eqs. (2.27) and (2.28)), while $q_c = (\gamma_c^2 - 1)^{1/2}$, which results in a slight but acceptable overestimate of q_c in comparison to the numerically calculated critical momentum [19]. The consideration of the synchrotron radiation losses lead to higher values of q_c, particularly when D is close to the threshold electric field [19].

2.4.4 Limiting energy

The test particle model provides a simple framework which allows not only an easy estimate of the critical quantities that determine the conditions for runaway electron generation, but also estimates of the final energies that the runaways can reach.

One of the main features of the single particle equations (Sec. 2.4.1, Eqs. (2.24), (2.25)) is the appearance of a stable focus P_2 in momentum space toward which all the electron trajectories outside S_r tend. The electron energy, γ_l, corresponding to the singular point P_2 determines the energy limit for the generated runaway electrons. When the energy gain in the toroidal electric field is balanced by the collisional and radiation losses, the escaping electrons will reach the maximum energy at P_2. The relation between the energy limit γ_l at P_2 and the normalised electric field D is given by the branch II of Eqs. (2.27) and (2.28) (Fig. 2.7) and is shown in Fig. 2.10.

Fig. 2.10 also shows are the limiting energies obtained from Eq. (2.27) and (2.28) assuming in the radiation term: (a) only electron gyromotion

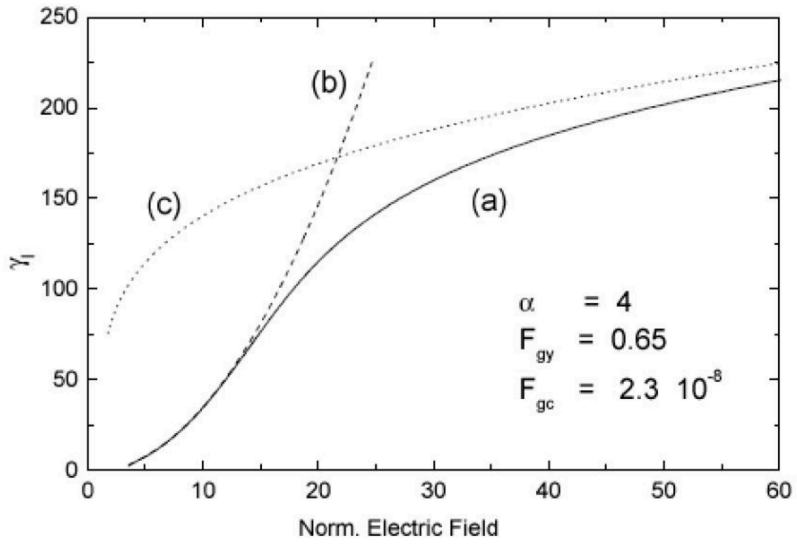

Figure 2.10: *(a) Runaway energy limit, γ_l versus normalised electric field D. The energy limits estimated assuming the synchrotron radiation ruled mainly by (b) the electron gyromotion (dashed line) and (c) the guiding centre motion (dotted line) are also included. Plot reference [19].*

around the toroidal magnetic field, and (b) guiding centre motion along the toroidal path alone. It is apparent from the figure that for low values of the electric field, γ_l is dominated by the radiation due to the electron gyromotion, as when the field is weak, the collisions of the runaways with the plasma species are significant enough to increase the pitch angle, and in that way the radiation losses associated to the gyromotion. For high electric fields, the collisions with the plasma particles are negligible and the pitch angle tends to zero, which means that the radius of curvature is approximately equal to the major radius of the device and γ_l is dominated by the radiation associated with the electron motion along its toroidal path (i.e. the guiding centre motion). An explicit expression for γ_l as a function of D can be derived under the assumptions $\gamma_l^2 \gg 1$ and $\gamma_l \gg \alpha/2D$, yielding [19]):

$$\gamma_l = \frac{1}{2}\left[- B^{1/2} + \left(-B + \frac{2a}{B^{1/2}} \right)^{1/2} \right], \tag{2.31}$$

where

$$A = \left[27\,a^2 + \left(729\,a^4 + 6912\,b^3\right)^{1/2} \right]^{1/3},$$
$$B = -\frac{4 \cdot 2^{1/3} b}{A} + \frac{A}{3 \cdot 2^{1/3}}, \tag{2.32}$$

and $a \equiv \alpha F_{gy}/DF_{gc}$ and $b \equiv (D-1)/F_{gc}$.

As discussed in Ref. [19], simpler expressions for γ_l for the cases of the electron synchrotron radiation dominated by the gyromotion and the guiding center motion can be produced yielding, respectively

$$\gamma_l \simeq \frac{D(D-1)}{\alpha\, F_{gy}}. \tag{2.33}$$

and

$$\gamma_l \simeq \left(\frac{D-1}{F_{gc}} \right)^{1/4}. \tag{2.34}$$

2.4.5 Additional energy loss mechanisms

The runaway energy limit can be modified by any mechanism that causes an increase in the electron pitch angle, since it causes an increase of the radiative power associated with the electron gyromotion, and thus the final runaway energy is reduced. These processes might further help to limit the runaway energy in tokamak discharges.

One of these mechanisms is the *ripple resonance*. It occurs when the electron gyromotion becomes resonant with the harmonics of the toroidal magnetic field ripple. The strong pitch angle scattering due to the interaction with the ripple resonances causes momentum transfer to perpendicular direction, which in turn enhances the power radiated by the electron [29]. The greater the synchrotron losses lower the value of the runaway energy limit. A resonance between the electron gyrofrequency and the fundamental ripple frequency was predicted to be sufficient to pose an upper limit on the runaway electron energy during plasma disruptions in large tokamaks (such as JET and ITER) [30].

Another mechanism that affects the runaway energy are the *radial diffu-*

sive losses, which can have an effect on both the runaway generation process and the runaway energy. If the electron loss rate is strong enough, electrons can diffuse out before they run away, therefore reducing the runaway production. There is experimental evidence [31] of successful runaway suppression during disruptions due to anomalous radial losses associated with the magnetic fluctuations. On the other hand, for the existing runaways, the runaway lifetime in the tokamak can be determined by the radial losses, and so changing their distribution function and reducing the maximum attainable energy. As derived in Ref. [32], the effect of the radial diffusion losses can be analysed using the test particle model, by simply including the friction force $\vec{F}_d = -\vec{q}/\tau_{dr}$ in the test relaxation equations. In the force term, $\tau_{dr} = \nu_r \tau_d$ is the normalised diffusion time and $\tau_d = a^2/j_0^2 D_r$ is the characteristic diffusion time for the runaway losses, where D_r is the runaway radial diffusion coefficient, a is the plasma minor radius and j_0 the first zero of the Bessel function J_0. In the case of fully stochastic magnetic fields, the diffusion coefficient can be approximated by $D_r = D_m v_{||}$ [33], where $v_{||}$ is the parallel (to the magnetic field) electron velocity and $D_m = L_{||}\tilde{b}^2$ ($\tilde{b}$ is the amplitude of the normalised radial magnetic fluctuation, $\tilde{b} \equiv \tilde{B}_r/B_0$, and Ł$_{||} \approx \pi q_0 R_0$ is the parallel correlation length of the fluctuations, with the safety factor q_0).

The inclusion of the friction force keeps the main features of the test relaxation equations and the singular points in phase space, but they change due to the diffusive process. The radial losses increase the value the threshold electric field for runaway generation and reduce the runaway energy limit [32].

2.5 Runaway electrons and disruptions

2.5.1 Disruptions and runaway mitigation

A disruption is a violent unstable event which leads to a sudden loss of plasma confinement. The plasma is rapidly extinguished and the thermal and magnetic energy stored in the plasma are transferred by large power loads and electromechanical forces to the structures surrounding the plasma. In future reactors, energy loads and forces of such magnitude over short times can cause catastrophic damage. Therefore, it is essential that disruptions are well understood and to develop methods to avoid and/or mitigate them.

An example of a disruption is given in Fig. 2.11. Many different precursor scenarios can lead to a disruption, although one of the main causes is the growth of large amplitude unstable magnetohydrodynamic (MHD) modes, usually tearing modes, which induces a rapid loss of plasma confinement and so a fast cooling of the plasma ($\sim 0.1 - 1$ ms). This is the thermal quench (TQ) phase of the disruption (centre plot in Fig. 2.11), in which the plasma temperature drops abruptly down to a few eV while the plasma thermal energy is deposited onto PFCs. Meanwhile, a redistribution of the plasma current occurs flattening the profile and resulting in a small increase of the current (a little peak seen in the top plot, typically $\sim 15\%$ of the total current), and a small negative drop in the plasma loop voltage, V_l. As a consequence of the temperature decrease, plasma resistivity ($\eta \propto T_e^{-3/2}$) and electric field ($E_{||} = \eta\, j$) increase quickly (bottom plot, Fig. 2.11, where $E_{||} \sim V_l/(2\pi R_0)$, R_0 being the plasma major radius). In continuation, the current quench (CQ) phase begins (usually lasting over a few tens of ms, top plot) when the plasma current starts to fall resistively and the strong electric field induced by plasma cooling results in the generation of a high number of runaway electrons, that can reach tens or hundreds of MeV. During the CQ phase, the plasma magnetic energy is transferred by radiation on PFCs as well as to the runaway electrons leading to avalanche multiplication of the initial runaway seed. At the final stage of the CQ, all the current is carried by REs and, as they are essentially collisionless due to their high energy, the current does not decay resistively anymore and establishes a so-called runaway current plateau (~ 1 MA in bottom plot of Fig. 2.11).

In large tokamaks as JET and JT-60U [34, 35], RE plateau currents of

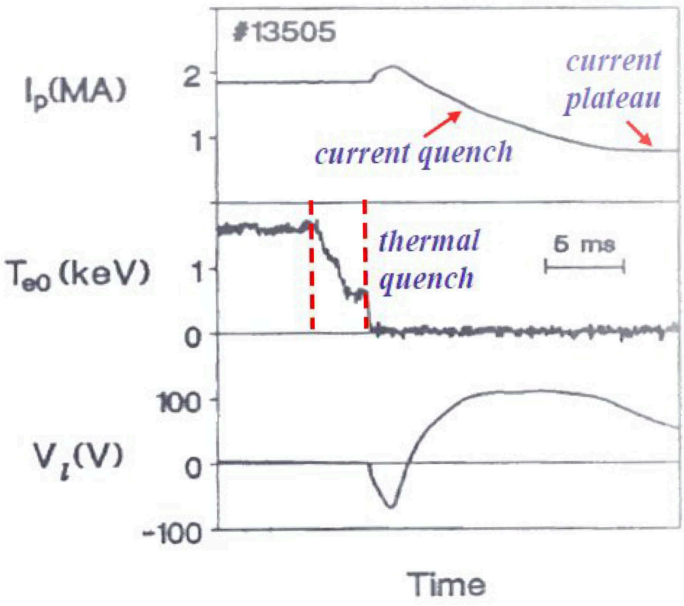

Figure 2.11: *Evolution of plasma current, central temperature and loop voltage during thermal and current quench stages of a disruption in the JET tokamak. Image from [12].*

several mega-amps have been recorded. It is foreseen that, during disruptions in ITER, large runaway currents can be generated (up to $\sim 10\,\mathrm{MAs}$ [18]), mainly due to the secondary generation of runaway electrons, which increases with the plasma current. Hence, it is urgent to develop strategies for mitigating the damage associated with the disruption generated electrons in case they can interact with the wall structures.

One of the most promising candidates consist of injecting large amounts of high Z impurities by Massive Gas Injection (MGI) or, most probably due its better efficiency, by Shattered Pellet Injection (SPI) [36, 37]. The injection of the impurities increases the plasma density and the collisionality of the runaway electrons (free and bound electrons should be included) and, therefore, the critical electric field, E_R, for runaway generation and, if

$$E_{||} < E_R \equiv \frac{n_e\, e^3 \ln\Lambda}{4\pi\varepsilon_0^2\, m_e\, c^2} \approx 0.1 \times n_e[10^{20}\mathrm{m}^{-3}],$$

the runaway electrons will be suppressed. Moreover, the injection of impurities increases substantially the runaway energy dissipation due to the strong synchrotron radiation associated with the electron pitch angle increase when the runaways collide with the impurities, as well as due to the large electron bremsstrahlung radiation in a plasma with a high impurity content [38].

Other runaway mitigation schemes are based on the fact that the runaway electrons are essentially collisionless, so that they closely follow the magnetic field lines. Thus, if the magnetic field is perturbed, the runaway electrons could get de-confined and escape following the radial magnetic field perturbations. In this way fast losses of runaways can be prompted, for instance, via external MHD perturbations by external coils, suppressing the runaway population.

2.5.2 Runaway control

Methods of post-disruption runaway electron beam control aim to give solutions for large experiments as ITER, in situations when complete mitigation of the runaway population would not be feasible. One of the most promising approaches is the development of beam control algorithms for stabilisation of the RE beam, minimising the interaction of the runaway electrons with the wall structures, and subsequent current dissipation, frequently done in combination with MGI and SPI as auxiliary means [4].

Recent simulations have shown that for ITER disruptions, if $I_{p0} - I_{RE,max}$ is less than $\approx 5\,\mathrm{MA}$ (I_{p0}: pre-disruption plasma current; $I_{RE,max}$: maximum runaway current) and $dI_p/dt < 0.5\,\mathrm{MA/s}$, RE beam control could prove to be effective [39]. The RE beam control strategies are based on controller systems which manage RE beam confinement and current dissipation. The controllers ramp-down the current if a trigger is set off by the RE diagnostics available for the device, which monitor and compare several plasma parameters with their reference values. If the RE plateau is detected, the system initiates the current ramp-down, with pre-selected ramp-down rate, in order to avoid premature runaway beam loss [40], and inducing beam displacement towards the low field side. The controller stabilisation secures the beam position and accounts for the outward shift of the beam using external coils for plasma position. The RE beam control system developed in FTU will be discussed, together with the experiments carried out, in Chapter 5.

Part II

Runaway electrons in the FTU tokamak

Chapter 3

Runaway electron diagnostics in FTU

"There are two possible outcomes: if the result confirms the hypothesis, then you've made a measurement. If the result is contrary to the hypothesis, then you've made a discovery."

Enrico Fermi

3.1 Introduction

The important ITER physics questions concerning runaway electrons addressed in this thesis are the critical electric field for RE generation, RE dynamics and control of disruption-generated REs. In the FTU tokamak, the experiments dedicated to runaway electron studies have been supported by the installation of an extensive set of RE diagnostic systems. They consist of diagnostic, hardware and software tools integrated in the real-time (RT) plasma control system [4]. A complete overview of the FTU diagnostics (not only RE diagnostics) can be found in Ref. [41].

A substantial amount of work carried out in this thesis has been devoted to the setting-up and validation of new RE diagnostics in FTU, mainly the Gamma Camera and the Runaway Electron Imaging and Spectrometry (REIS) system [4]. This activity has been performed in collaboration with the FTU tokamak within the framework of the EUROfusion Projects WP14-MST2-9, WP15-MST2-15 ("Runaway Electron Studies in FTU"; 2014-2016),

WP18-MST2-15 ("REIS activities"; 2018), MST-1 2017 and MST-1 2018 ("Medium Sized Tokamaks"; 2017 and 2018). Part of the content in this chapter has been published in articles listed in the Published and Submitted Content: B. Esposito, L. Boncagni, P. Buratti, D. Carnevale, F. Causa, M. Gospodarczyk, J.R. Martin-Solis, Z. Popovic et al., "Runaway electron generation and control", *Plasma Phys. Controll. Fusion* **59** *(2017) 014044*, D. Carnevale et al. (EUROfusion MST1 Team, includes Z. Popovic as a collaborator), "Runaway electron beam control", *Plasma Phys. Controll. Fusion* **61** *(2019) 014036*, and F. Causa et al. (includes Z. Popovic as a collaborator), "Runaway Electron Imaging Spectrometry (REIS) system", *submitted to Rev. Sci. Instrum. (2019).*

The presence of runaway electrons in FTU is indicated by: (i) the synchrotron radiation emitted by runaway electrons, (ii) the appearance of signature hard-X ray (HXR) and gamma radiation, as well as (iii) neutron emission, where the latter two originate from runaway induced reactions. These include interactions of REs with different targets: plasma and limiter bremsstrahlung, which may cause photo-nuclear processes and ensuing radioactive decay, electro-disintegration, and electron-positron pair production [42]. However, detection of neutrons, HXR and gamma radiation in FTU is not associated only with REs. Other sources include the neutrons produced in fusion reactions and the gamma rays from inelastic neutron scattering reactions, i.e. neutron capture, which are differentiated using customised diagnostic systems.

The runaway electron measurements pertinent for the present work are performed using the following RE specific diagnostic systems installed in the FTU: (a) BF_3 chambers, (b) NE213 organic liquid scintillator, (c) Gamma camera and (d) Runaway Electron Imaging and Spectrometry (REIS) system.

(a) BF_3 chambers

A collection of six absolutely calibrated BF_3 proportional counters (5 ms integration time), which are only sensitive to neutrons and placed in pairs 120° apart on top of the cryostat [43], is set-up to monitor the neutron yield (neutron rate, Y_n, in the range $10^9 < Y_n < 10^{12}$ n/s). The BF_3 signal is used to indicate the presence of runaways through comparison with the signal from the NE213 scintillator, an example of which is shown in Fig. 3.1, while

a further signal treatment for the study of the conditions for RE generation is described in Sec. 4.2.

(b) NE213 liquid scintillator

The NE213 liquid organic scintillator is a cylindrical (5" diameter × 5" thickness) detector, sensitive both to neutrons (n) and hard X- and gamma-rays (γ). It is situated on the equatorial plane outside the cryostat, coupled to a photomultiplier tube (PMT), and operated in current mode at 20 kHz sampling rate. The NE213 detector is cross-calibrated with the set of BF_3 neutron detectors in discharges with negligible runaway production [44], when a perfect overlap of the two signals is achieved. However, in runaway discharges, an excess of gamma-rays increases the NE213 signal and the two traces diverge. NE213 is henceforth used to monitor the HXR emission due to runaway electrons, as illustrated in Fig. 3.1, comparing the traces of the two detectors during discharges with and without runaways.

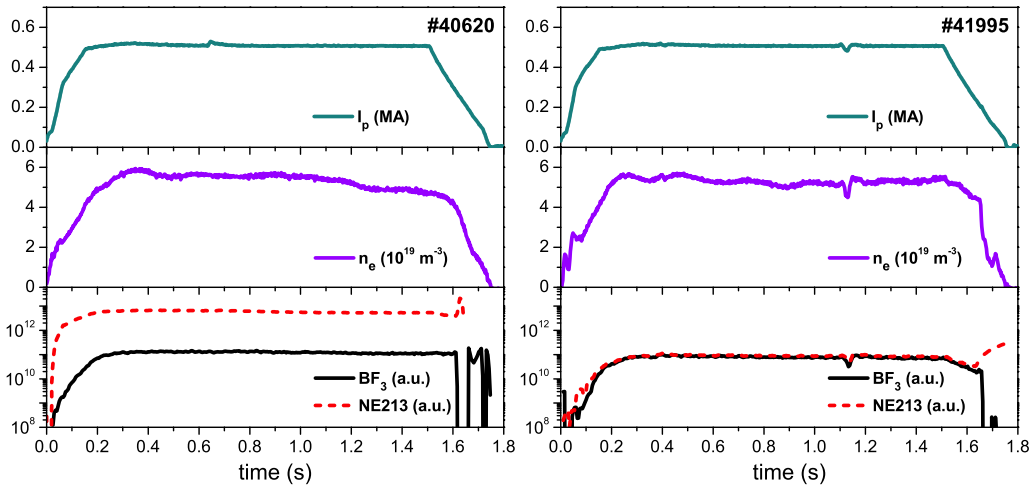

Figure 3.1: *Comparison of two current flat-top pulses at B_t = 4 T, # 40620 with REs (left) and # 41995 without REs (rigth); top to bottom panels: plasma current I_p, line-averaged density n_e, and BF_3 and NE213 detector signals.*

(c) Gamma Camera

A gamma/neutron detector system [45], referred to as the "gamma camera" (GC), provides radially resolved measurements of HXR emitted perpendicularly to the magnetic field and produced by the runaway electrons through bremsstrahlung in the plasma. The system is built with NE213 detectors (2" diameter × 2" thickness) capable of n/γ discrimination, operated in count mode with a digital acquisition system (14-bit, 400 MSamples/s) [46]. The camera is sensitive to HXR with energy $> 100\,\mathrm{keV}$ and its time resolution, depending on the count rate, goes down to $\sim 1\,\mathrm{ms}$. A more elaborated description of the GC is given in the next section, followed by measurements obtained in several types of FTU discharges, important for this thesis.

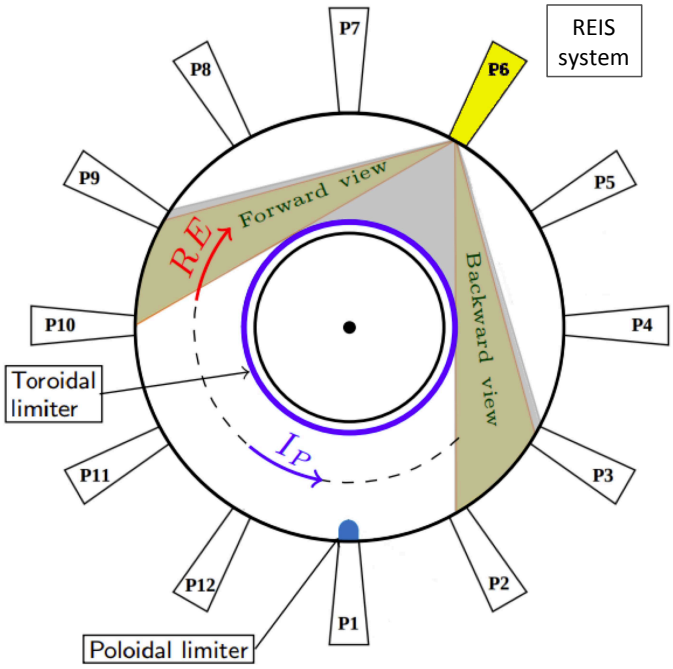

Figure 3.2: *A simplified schematic representation of the FTU tokamak top view, depicting the field of view of the REIS system installed at port 6 (P6). Figure from [47].*

(d) Runaway Electron Imaging and Spectrometry (REIS) system

The runaway electron imaging and spectrometry (REIS) system [48] is a

wide-angle optical diagnostic that collects the runaway electron synchrotron radiation from two plasma cross sections corresponding to the RE backward and forward views (Fig. 3.2), and transmits it to visible/infrared spectrometers through an incoherent bundle of fibres. Its spectral range spans from 370 to 2100 nm and the sampling time is configurable down to 10 ms. The REIS system also features a CCD camera for visible image acquisition of the vessel, closely aligned to the view seen by the fibre bundle. The complete system description and its use in the present work is given in Sec. 3.3.

3.2 Gamma camera

3.2.1 Description of the gamma camera (GC) diagnostic system

The FTU gamma camera system [45] is a collection of liquid organic scintillators (2" diameter and 2" thick NE213 detectors) distributed along six radial lines of sight (LOS) looking at the plasma from a vertical port below the equatorial plane of the tokamak (Fig. 3.3, Table 3.1). Each detector is coupled to a photomultiplier and an embedded ^{22}Na source for energy calibration purposes. The gamma camera digital acquisition system is optimised for high count-rate operation (MHz range), reprocessing of data and Pulse Height Spectra (PHS) analysis. As mentioned, the scintillators are capable of spectrometric and neutron/gamma (n/γ) discrimination and radially arranged; thus, the GC system is able to provide radial profiles of HXR emission perpendicular to the plasma current, which originates from RE bremsstrahlung in the plasma.

Table 3.1: *Gamma camera LOS characteristics: radial position, collimator diameter and collimator length*

LOS #	r (cm)	Coll. diameter (cm)	Coll. length (m)
1	-18	1	1.2
2	-4	1	1.2
3	1	1.2	1.2
4	6	1.4	1.2
5	13	1.7	1.2
6	21	1.7	1.2

Within the liquid scintillators, the incident photons with energies greater than $\sim 100\,\mathrm{keV}$ generate Compton scattered electrons, while incident neutrons create recoil protons through (n, p) elastic scattering. The emerging charged particles then excite the organic molecules inside the scintillators and produce fluorescence, measured by photo-multipliers coupled to each scintillator. The discrimination between the incident particles is done by the recorded pulse shape analysis where the pulse energy is determined by pulse

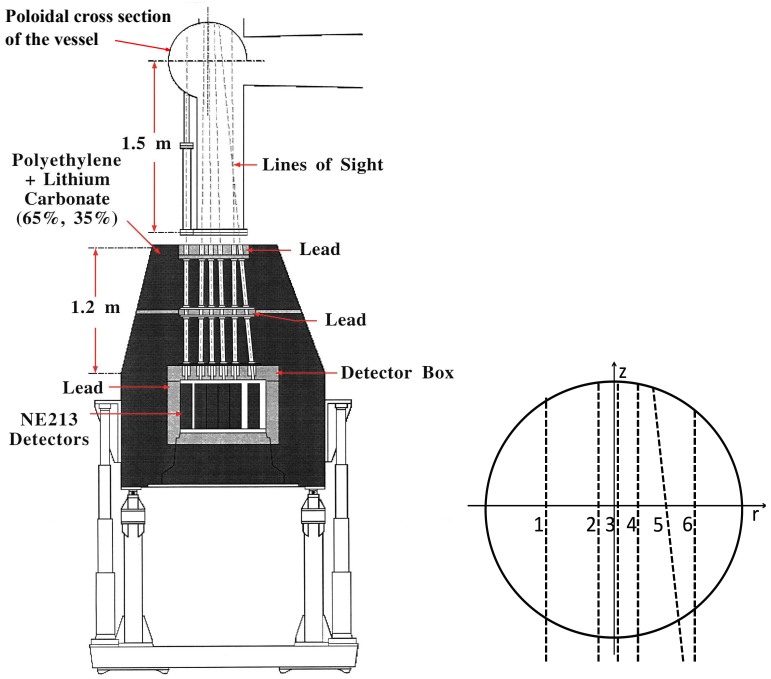

Figure 3.3: *Schematic of the FTU radial hard X-ray profile monitor (the gamma camera) with the layout of the six lines of sight along the poloidal cross section of the tokamak vessel. Image credit [45].*

integration, and the neutron/gamma separation by integration of each pulse in two different time intervals [49]. For an NE213 signal above $\sim 10^{12}\,\mathrm{s}^{-1}$, a time resolution of ~ 10 ms can be achieved.

The GC measurements are corrected for the following three background components of the signal: (a) neutron-induced background, that is, photons emitted during the radiative capture of neutrons interacting with the inner wall, other vessel elements and the GC shielding layer (a small correction, proportional to the total neutron yield, which is usually low in FTU deuterium discharges, $\sim 10^{11}\,\mathrm{s}^{-1}$), (b) reflectivity of the vessel, i.e. photons reaching the detectors through the collimators after scattering from the vessel (a component significant only for the FTU LOS #1 which intercepts the vessel and probes the plasma edge, and for peaked HXR profiles), and (c) RE-generated background, specifically photons created in RE bremsstrahlung when hitting thick-target plasma facing components (PFCs) and GC struc-

tures, that pass through the detector shielding (a few percent contribution during current flat-top phase on the inner three LOS, and even less on the outer three LOS; however, a significant signal contamination is observed in RE plateau phase: the inner LOS #1, #2 and #3 should be excluded from the radial profile analysis).

3.2.2 Measurements performed with the GC diagnostics

There are four types of runaway discharges performed during FTU experiments which are significant for our investigation.

First is a typical FTU flat-top pulse in which runaway electrons are generated during the I_p ramp-up and remain until the end of the discharge. An example in Fig. 3.4 gives time traces of the plasma current (I_p), the loop voltage (V_{loop}), the line-averaged electron density (n_e), the neutron and neutron/gamma rate monitors (BF_3 chamber and NE213 scintillator, respectively), and the gamma camera signals. A steep increase in NE213 scintillator signal in the first few ms, departing from the one of BF_3, indicates the presence of runaway electrons, and can be observed in the signals from the GC channels too.

The bottom right plot of the same figure includes a set of GC profiles for several time slices during the current flat-top. The HXR emission starts in the centre and then partly moves to the outer part of the plasma, flattening out the profiles. As described in Ref. [45], the contamination of LOS #1-3 due to the vessel reflectivity and RE-generated background can be significant. Hence, the first two LOS have been excluded and still an increase in signal from LOS # 3 is visible in all of the profiles.

The remaining plot in Fig. 3.4 (right, top) shows the gamma PHS for each GC LOS, registering photons of energies up to ~ 5 MeV. A more elaborated signal treatment of the energy spectra (as done in [50], [51]) requires PHS unfolding using the NE213 response functions and is a part of ongoing studies.

Another type of RE discharge we consider is when the conditions for RE onset are met during the plasma current flat-top. Fig. 3.5 on the left shows the plasma current (I_p), loop voltage (V_{loop}), central line-averaged density (n_{e0}), and the HXR from the outer four channels of the gamma camera overlaid on

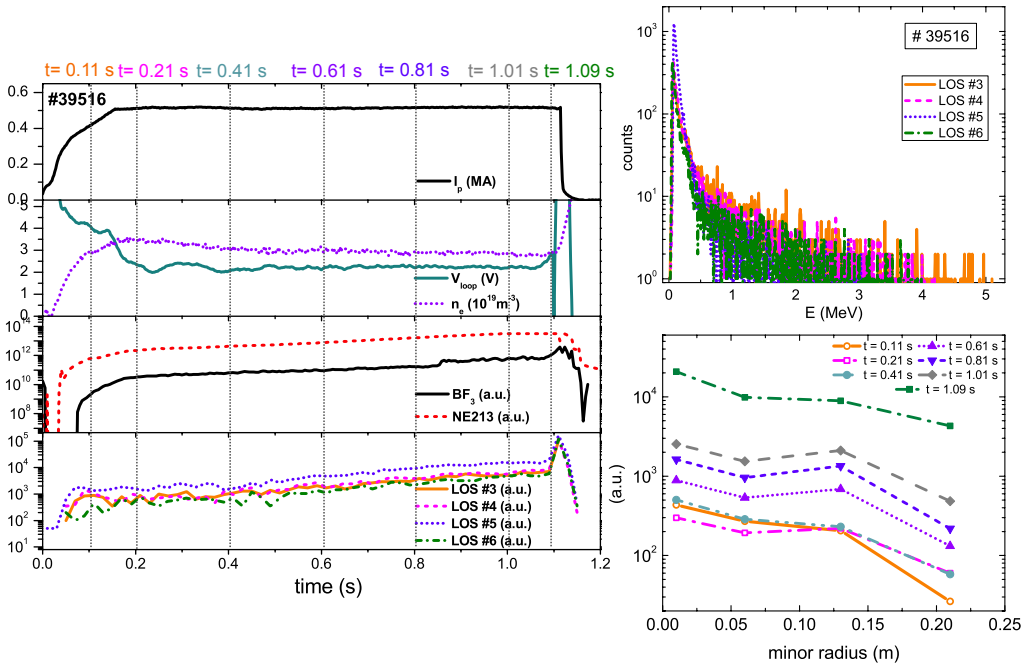

Figure 3.4: *FTU flat-top discharge (B_t = 4.1 T). Left (top to bottom panel): Time traces of plasma current (I_p), loop voltage (V_{loop}) and line-averaged electron density (n_e), HXR from NE213 scintillator and neutrons from BF_3, and line-integrated HXR from gamma camera (LOS #3-6). Right: Energy calibrated PHS (top) and radial profiles of line-integrated HXR emission from REs at indicted times (bottom).*

top of the neutron detector (n) and scintillator signals ($\gamma + n$) for reference. From the radial profiles at selected times (bottom plot on the right) after the runaway onset (indicated by the separation between the NE213 and BF_3 signals), we see that the early HXR peak is closer to the centre and moving out to the LOS #5, which could indicate runaway production in the plasma centre. The maximum RE energy can be approximated by the ends of the pulse height spectra (PHS) shown in Fig. 3.5 on the top right; in this case up to $\sim$ 3 MeV.

In contrast, when runaway electrons are generated in the beginning of the discharge and the runaway production stops later on during the I_p flat-top

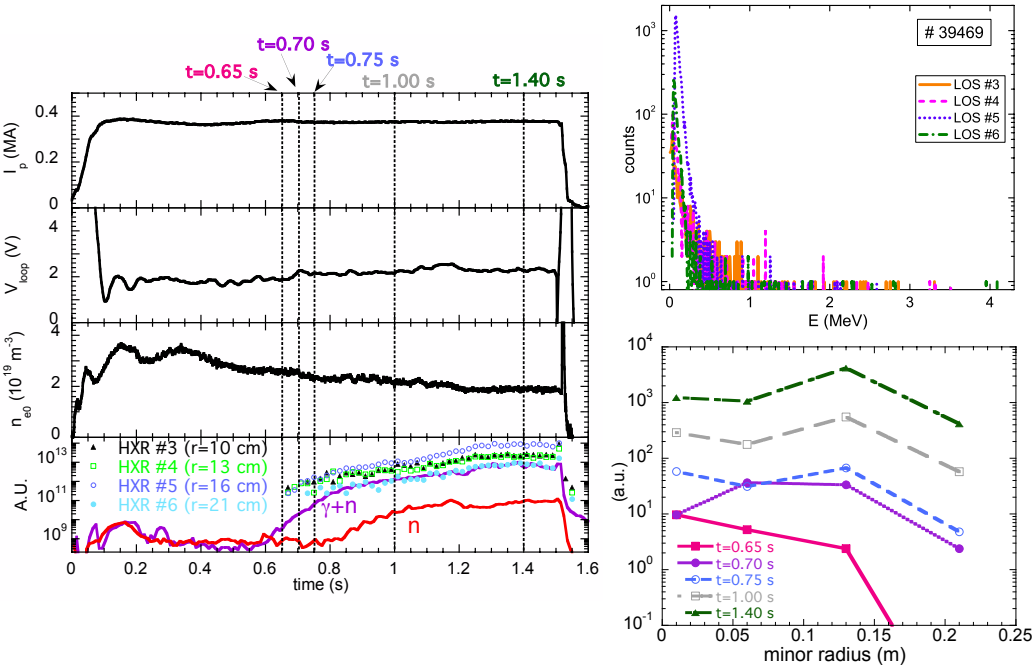

Figure 3.5: *FTU discharge # 39469 (B_t = 4.1 T). Left (top to bottom panel): Time traces of plasma current (I_p), loop voltage (V_{loop}), central line-averaged electron density (n_{e0}), line-integrated HXR from gamma camera (LOS #3-6), HXR from NE213 scintillator ($\gamma + n$) and neutrons (n) from BF_3. Right: (top) Energy calibrated PHS; (bottom) Radial profiles of line-integrated HXR emission from REs at different times after RE onset. Figure adapted from [4].*

phase, typically due to an increase of the density, a case of runaway electron suppression occurs. Such an example is presented in Fig. 3.6: the gamma camera PHS show lower energies (right, top) than in discharges where REs persist until the end (compare to flat-top RE case). Moreover, it is clear (right, bottom) that the gamma emission is consistently reduced already at t = 0.41 s.

Finally, a representative case of a RE active control experiment is illustrated in Fig. 3.7, a discharge in which runaway electrons are created initially in the plasma current ramp-up, and a disruption is induced at $t \sim 0.8$ s by

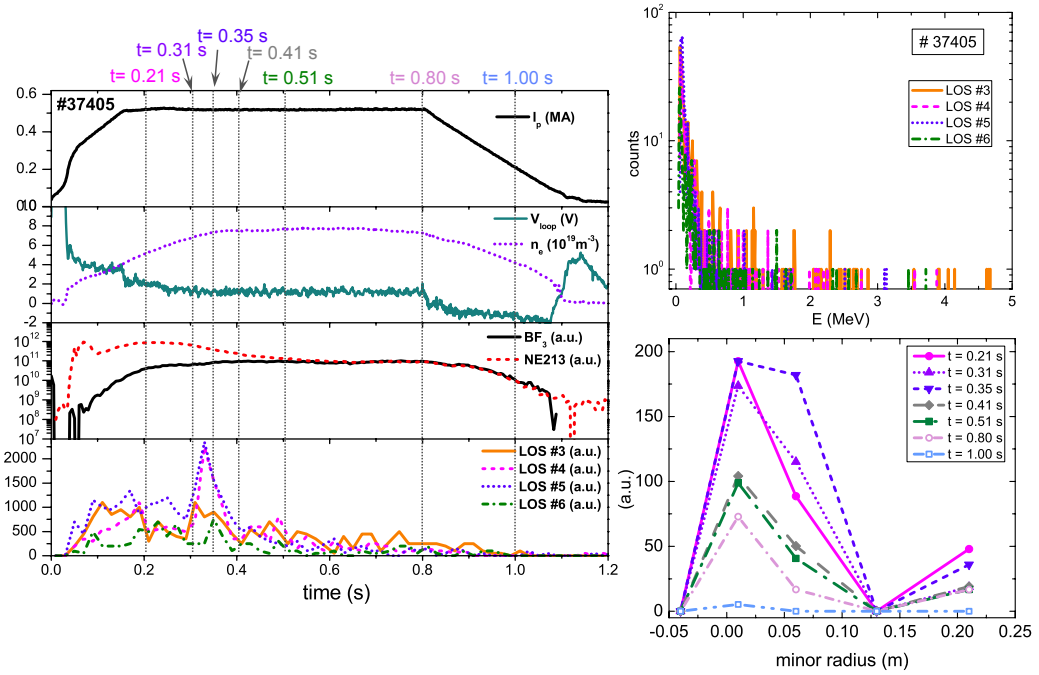

Figure 3.6: *FTU suppression discharge # 37405 (B_t = 6 T). Left (top to bottom panel): Time traces of plasma current (I_p), loop voltage (V_{loop}), line-averaged electron density (n_e), HXR from NE213 scintillator and neutrons from BF_3, and line-integrated HXR from gamma camera (LOS #3-5). Right: Energy calibrated PHS (top) and radial profiles of line-integrated HXR emission from REs at indicated times (bottom).*

argon injection, which is followed by a RE current plateau formation. The pre-disruption energy of REs, assessed by the ends of PHS given in top right plot of the figure, reaches $\sim$ 5 MeV in this case. Throughout the RE plateau phase (just after 0.8 s) the BF_3 and NE213 detectors often operate at the limit of saturation, due to a higher HXR and photoneutron emission than in the pre-disruption phase, caused by in-plasma and thick-target bremsstrahlung of circulating and lost REs onto the PFCs. However, a spike in the electron density is observed right after the disruption, and a considerable drop in GC signals, indicating that a significant decrease in lost REs might have occurred. The HXR radial profiles during the I_p flat-top and just before the disruption are given in the right plot of the figure.

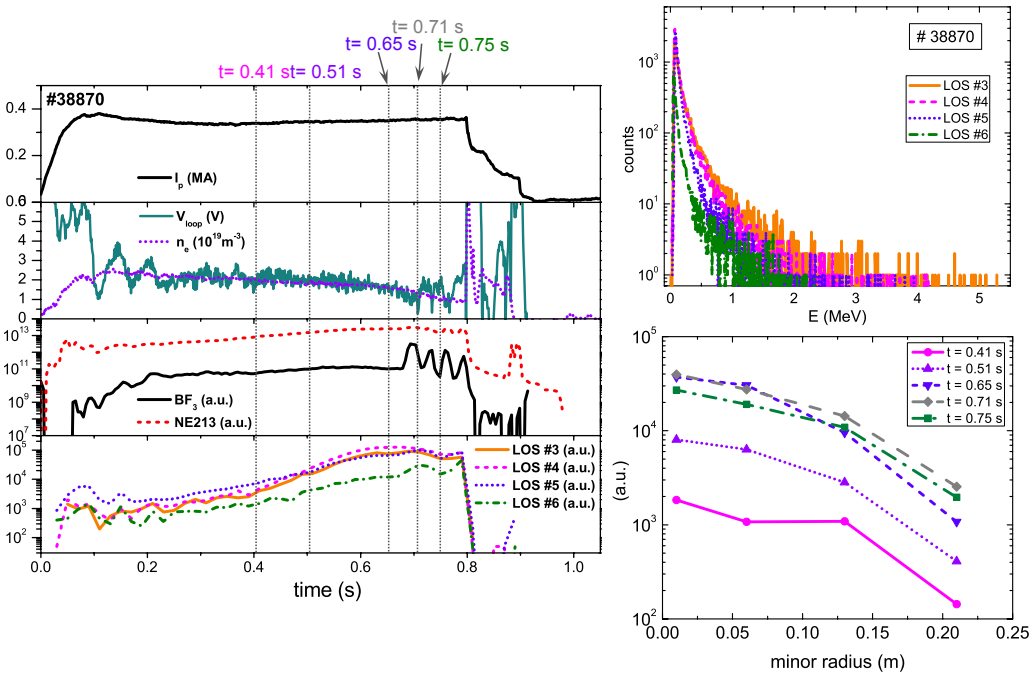

Figure 3.7: *FTU disruption discharge # 38870 (B_t = 4 T). Left (top to bottom panel): Time traces of plasma current (I_p), loop voltage (V_{loop}), line-averaged electron density (n_e), HXR from NE213 scintillator and neutrons from BF_3, and line-integrated HXR from gamma camera (LOS #3-5). Right: Energy calibrated PHS (top) and radial profiles of line-integrated HXR emission from REs for several times before disruption (bottom).*

3.3 Runaway electron imaging and spectrometry system

The synchrotron radiation emitted by runaways provides information about the energy and pitch angle of in-flight (confined) REs in different stages of the discharge. The Runaway Electron Imaging and Spectrometry (REIS) system [4] was designed for detection of runaway electron synchrotron spectra during plasma discharges in MST (Medium Size Tokamak) devices and has been tested in the FTU tokamak. In this section, the REIS diagnostic system is presented and examples of FTU measurements with the subsequent data analysis are shown.

3.3.1 Introduction. REIS system description

Charged particles accelerated in a magnetic field will radiate. For non-relativistic particle velocities we talk about cyclotron radiation, and the frequency of emission is simply the frequency of the particle gyration in the magnetic field. However, for emission by extreme relativistic particles, such as runaway electrons, the frequency spectrum is more complex; it can extend to many times the gyration frequency and is known as synchrotron radiation. In the highly relativistic case the emission is predominantly directed along the electron velocity vector in a narrow cone of half-angle $\alpha = \cos^{-1}\beta$ (where $\beta^2 = (v_{||}/c)^2 + (v_{\perp}/c)^2$) [52] and the polar plot of the instantaneous radiation intensity is similar to a cross section of a searchlight beam, as seen in Fig. 3.8 (a). The same figure (b), shows the radiation cone relative to the magnetic field direction, i.e. the pitch angle θ and, on the right (c), the solid angle to which the emitted radiation is confined over one revolution.

The power emitted at wavelength λ by a relativistic electron following a straight magnetic field line is given by [54]:

$$P_{cyl}(\lambda) = \frac{1}{\sqrt{3}} \frac{c\, e^2}{\varepsilon_0\, \lambda^3\, \gamma^2} \int_{\lambda_c/\lambda}^{\infty} K_{5/3}(l) dl, \tag{3.1}$$

where e is the electron charge, c is the speed of light, ε_0 is the vacuum permittivity, $\lambda_c = (4\pi c\, m_e \gamma_{||})/(3eB\gamma^2)$, $\gamma_{||} = \sqrt{1 - v_{||}^2/c^2}$, m_e is the electron mass, B is the magnetic field strength, and $K_\nu(x)$ is the modified Bessel function of the second kind. It should be noted that the effects of magnetic field line curvature and the curvature drift should be taken into account in the calculation of power radiated by an electron in a tokamak, as it has been done in Ref. [55]. However, considering that the integrands in that formula can have excessive computational requirements, as a first approximation for diagnostic development and validation, the use of Eq. (3.1) can be justified.

Figure 3.9, on the left, shows the spectra for synchrotron emission from a single relativistic electron for a range of energies. The spectra peak in the infrared (IR) region and shift down in wavelength toward the visible (VIS) for higher electron energies. On the right of the same figure, the synchrotron spectra for a relativistic electron moving in FTU have been calculated, clearly peaking in the IR part of the spectrum. The strong dependence of P_{cyl} on runaway electron energy is what the diagnostics detecting RE synchrotron

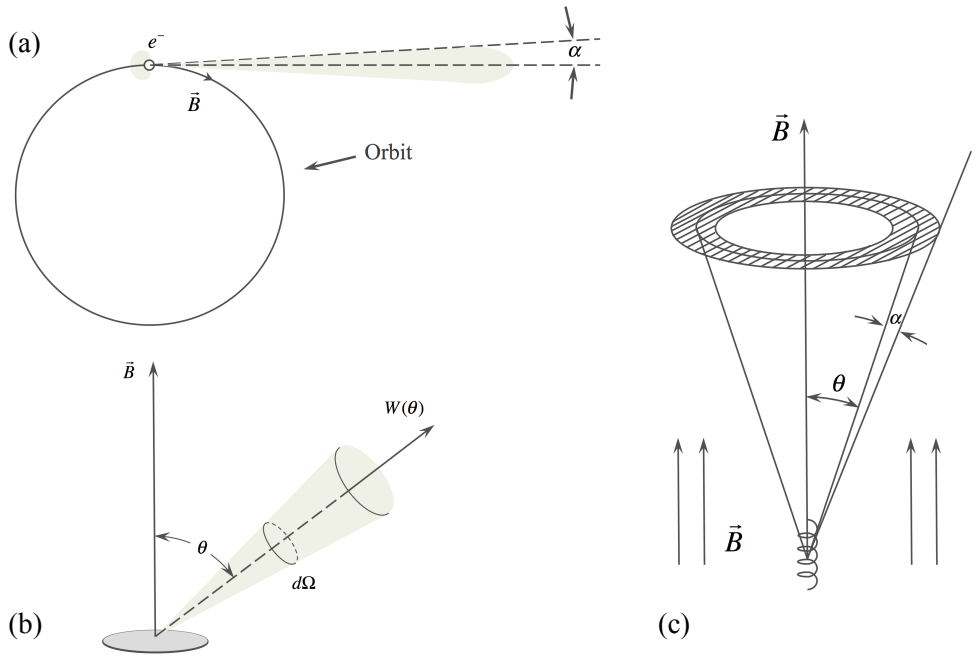

Figure 3.8: *Sketches of synchrotron radiation geometry for a highly relativistic electron: (a) polar plot of the emission showing it is predominantly directed along the instantaneous velocity vector of the electron, (b) synchrotron radiation cone from a particle with pitch angle θ, and (c) the solid angle (shaded area) to which the radiation is almost entirely confined over one revolution. Image after [52], [53].*

radiation rely on. However, the portion of electrons with higher γ (we can speak in terms of γ since $E = (\gamma - 1)m_e c^2$) contribute more to the radiation in the visible region, which means that only the tail of the distribution is indirectly observed in this range.

For synchrotron radiation imaging purposes, based on geometrical optics approach, it is important to accentuate that just a fraction of the photons in the emission beam from the source can be effectively measured. The photon flux density focused on the detector, i.e. the spectral brightness of the measured RE synchrotron emission in tokamaks is correlated with the number of observed REs, the electron pitch angle θ and the RE energy γ, and can be estimated by [57]:

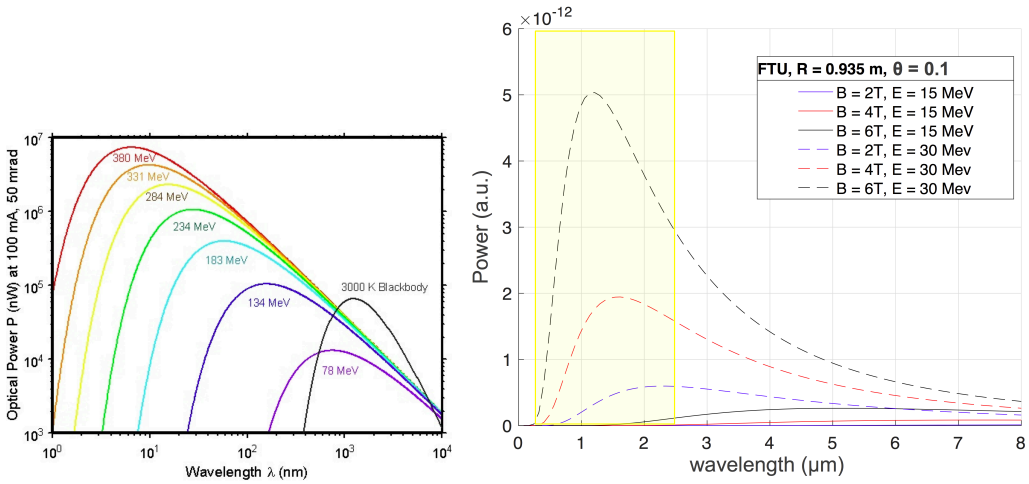

Figure 3.9: *Synchrotron radiation spectra for a single electron emission: (left) spectra peaking dependence on the electron energy with reference to blackbody radiation, and (right) power spectra calculated with FTU parameters for a range of energies and magnetic fields. Area shaded in yellow represents the wavelength region studied with the FTU REIS system. Image credit [56].*

$$B(\lambda, \theta, \gamma) = P(\lambda, \theta, \gamma)\, \frac{2R_0}{\pi\theta}\, n_r, \tag{3.2}$$

where n_r is the density of observed REs and R_0 is the major radius of the tokamak. The above estimate is valid for highly relativistic electrons and includes corrections: (i) for the limited solid angle in the view of the detector collection area, meaning that only the radiation of a toroidal fraction $\sim 2\theta/(2\pi)$ of REs is measured, and (ii) for the restricted number of photons collected by the detector optics. In our case, in Eq. (3.2) $P(\lambda, \theta, \gamma)$ is substituted by $P_{cyl}(\lambda)$, for the reasons mentioned earlier, thus predicting the brightness in a tokamak with reference to the single runaway electron emission, and which could later be compared with the measured brightness.

A prototype of a portable diagnostic for acquisition of synchrotron spectra from runaway electrons in MST devices, the Runaway Electron Imaging and Spectrometry (REIS) system, has recently been developed in FTU. The REIS system includes three visible/infrared spectrometers, coupled via a bundle of

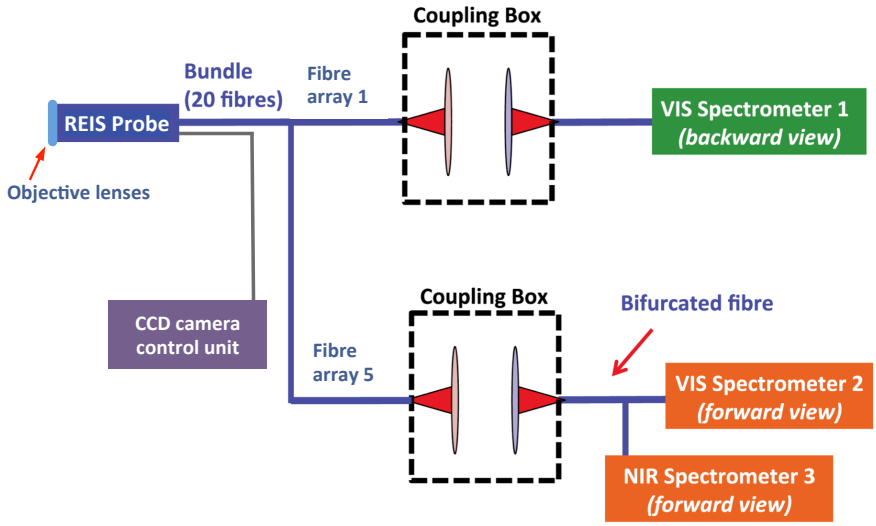

Figure 3.10: *REIS diagnostic schematic representation: the probe head with two wide-angle lenses, one coupled via optical fibres through a set of lenses to optical spectrometers for RE synchrotron spectra acquisition and another to a CCD camera for visible imaging of the poloidal cross section of the tokamak vessel. Figure adapted from [4].*

20 incoherent optical fibres to a diagnostic probe with a wide-angle objective lens collecting the RE synchrotron radiation from two plasma cross sections, in forward and backward view of the RE beam. A schematic of the configuration is given in Fig. 3.10. The coupling boxes outlined in the diagram contain sets of aligned lenses which serve to combine the bare fibre outputs and transmit them to the spectrometers. The probe is also equipped with a digital CCD camera, for visible imaging of the plasma inside the vessel close to the line of sight to which the fibre bundle is exposed. Fig. 3.11 shows the probe head, an image of the vessel taken by the CCD camera during a discharge in FTU, and an approximate outline of the fibre bundle view, indicating that only the first and last vertical arrays of fibres are viewing the plasma in directions nearly tangential to the orbit of runaway electrons, the RE backward (BW) and forward (FW) directions, respectively.

The outputs from the relevant fibre arrays are connected to the spectrometers to measure the spectra of the collected radiation. The signal from the incoming REs is sent via a bifurcated fibre simultaneously to spectrometers

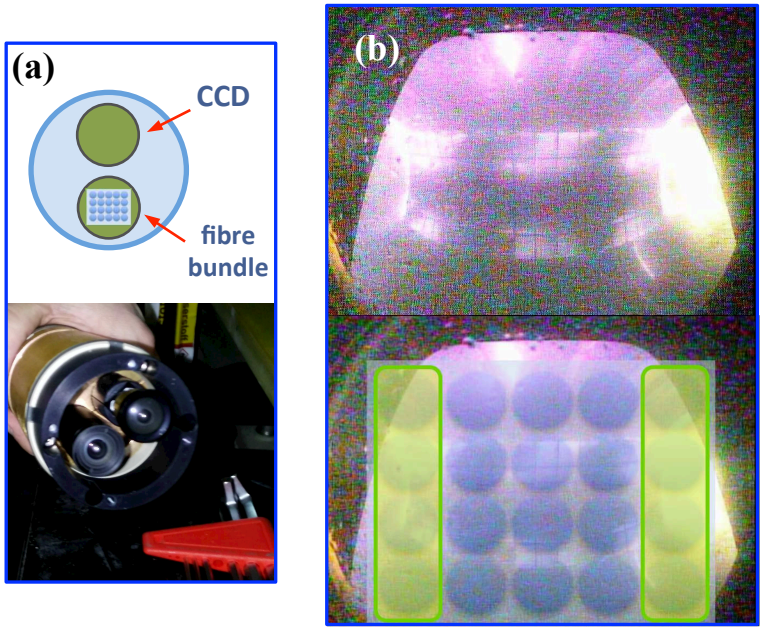

Figure 3.11: (a) *The REIS probe head layout and picture showing the two lenses below which are the CCD camera and the fibre bundle consisting of five vertical arrays of four low-OH optical fibres.* **(b)** *An image taken with the REIS camera during an FTU pulse (above) and a notional view of the fibres (below), designating that the leftmost vertical array (fibre array 1 in the system schematics in Fig. 3.10) measures the signal along the backward RE direction, while the last fibre array on the right (fibre array 5 in Fig. 3.10) collects the signal in the forward RE direction.*

covering visible (VIS) range from 300 - 860 nm and near-infrared (NIR) from 900 - 2500 nm. Meanwhile, the backward signal is transferred to another spectrometer operating in the identical interval (300 - 860 nm) of the visible range. The region of wavelengths considered by the REIS system with reference to the FTU single electron emission spectra is shown in light yellow in Fig. 3.9.

The data acquisition is synchronised with the main common gate of the tokamak for initialisation and directed by a customised LabView program. Data is gathered every 20 ms (configurable down to 10 ms) simultaneously from the three spectrometers, and images from the CCD camera every 40 ms.

The REIS system calibration was done using a tungsten halogen lamp and a lambertian diffuser [47], both of which are calibrated. The absolute calibration in the visible range was obtained with the lamp-diffuser system, by taking the ratio of the diffuser radiance to the measured data. For the infrared range, however, the output power of the calibrated source was insufficient, and a relative calibration was done instead, by pointing the tungsten lamp directly to the collection optics of the REIS system without the diffuser. A blackbody radiation curve for $T = 1750°C$ (corresponding to the tungsten lamp) was extrapolated to the infrared part of the spectrum, the ratio of which to the measured data was then taken as the relative calibration of the system. The calibration curves obtained for the forward and backward REIS detectors are shown in Fig. 3.12. When applying the calibration to experimental data, the relative curve in the infrared range is multiplied by an arbitrary constant to maintain the presumed continuity of the spectrum.

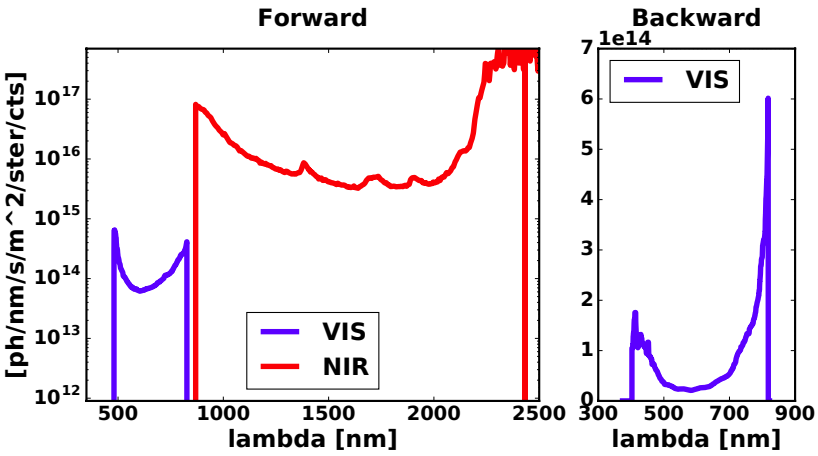

Figure 3.12: *Calibration curves for forward (left) and backward (right) lines of sight (LOS) of the REIS system. Figure from [47].*

The REIS data analysis has a goal of recovering energy and distribution of runaway electrons emitting the radiation from the measured spectra. Ideally, such analysis would be done in real time and serve as part of a congregate RE diagnostic-control system. With the present prototype of the REIS system, such complete use is not established, and so an enhancement of the diagnostic is under development. Specifically, the upgrade will include an extension of the wavelength range to 5000 nm (to cover the peaks of synchrotron spectra

across different MST devices), with the corresponding calibration, and more elaborated data processing and interpretation tools. In addition, application of synthetic synchrotron diagnostic frameworks such as SOFT [58], which takes into account the geometric effects in computation of synchrotron images and spectra, would provide a more complete and accurate evaluation of the REIS data. In the following section, a standard runaway discharge with REIS measurements and the analysis we performed is described.

3.3.2 REIS spectra analysis

To illustrate the REIS data interpretation, we can look at the synchrotron radiation spectra for an FTU discharge with runaway electrons during current flat-top. The example is discharge #40677, shown in Fig. 3.13, a 0.5 MA ohmic (OH) discharge for which runaway electrons can be detected since the current ramp-up, as evidenced by the difference between the BF_3 neutron detector and the NE213 neutron/gamma scintillator signals [44] (left plot). The synchrotron emission spectra measured by the REIS system at several time slices are shown in the right plot of the figure.

The measured synchrotron emission spectra are compared with spectra calculated in two ways: a) using the runaway distribution functions estimated for this pulse, and b) assuming a monoenergetic RE beam with energy equal to the maximum electron energy. It should to be noted that the monoenergetic fit of the synchrotron spectra can be misleading for estimation of the runaway electron energy. There are multiple sets of (p, θ) pairs for a given magnetic field that lie on the curve which is a solution to the Eq. (3.1) in (p, θ) space, warranting the same shape of the spectrum. This means that a restriction must be imposed on energy or pitch angle in order to retrieve the correct value of the other quantity.

For our example discharge, the simulated runaway electron dynamics is given in Fig. 3.14. On the left plot of the figure, panel (b), is the runaway electron production rate, calculated assuming to be dominated by the Dreicer mechanism, Eqs. (2.10) and (2.12), as typically observed in FTU OH discharges [44]. The REs are generated at the beginning of the discharge, due to large electric field and low density, and the runaway production stops soon at ~ 0.15 s. The simulated dynamics is confirmed by the comparison of the n/γ signals from neutron detectors and the scintillator, shown in panel (a).

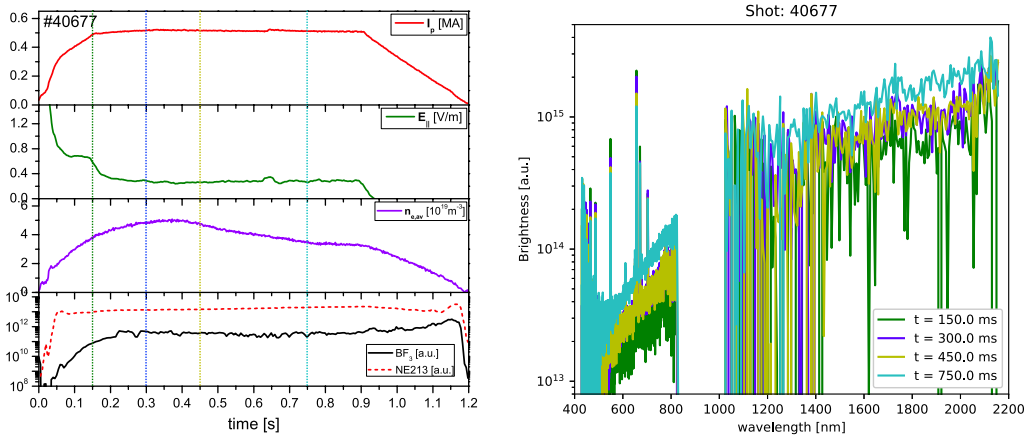

Figure 3.13: *FTU discharge #40677: (left) Time traces of the plasma current (I_p), electric field ($E_{||} \cong V_{loop}/(2\pi R_0)$; V_{loop} is the loop voltage), line-averaged central density (n_{e0}) and NE213 (γ+n) and BF_3 (n) signals; (right) Measured synchrotron radiation spectra at several time slices indicated in the left figure.*

To estimate the runaway energy distribution function, $f_r(E)$, we refer to the test particle model for the runaway dynamics introduced in Sec. 2.4.1, that considers the electron acceleration by the electric field, Coulomb collisions with the plasma particles and electron deceleration due to synchrotron radiation losses. $f_r(E)$ is obtained by calculating the energy evolution of the generated runaway electrons from:

$$f_r(E,t) = \int_0^t \frac{\mathrm{d}n_r}{\mathrm{d}t'}(E_0,t')\,\mathrm{d}t', \tag{3.3}$$

where $t = 0$ denotes the initial time of runaway generation and the integration is carried out over times t' for which an electron generated with energy E_0 would have gained, according to the test particle equations, an energy E at time t. The resulting distribution function at different times during the discharge is given in Fig. 3.14 on the right. The shape of the distribution function is initially broad, extending up to the maximum runaway energy at each time step, and afterwards narrowing along the discharge with a trend to accumulate close to a steady state energy ~ 19 MeV up to ~ 0.9 s. The time evolution of the calculated maximum electron energy, E_{max}, [E_{max} =

$(\gamma_{max} - 1)\, m_e c^2]$ and average electron energy, E_{av}, found as

$$E_{av} = \frac{\int_{E_0}^{E_{max}} E\, f(E)\, \mathrm{d}E}{\int_{E_0}^{E_{max}} f(E)\, \mathrm{d}E}, \tag{3.4}$$

is presented in panel (c), left plot of Fig. 3.14.

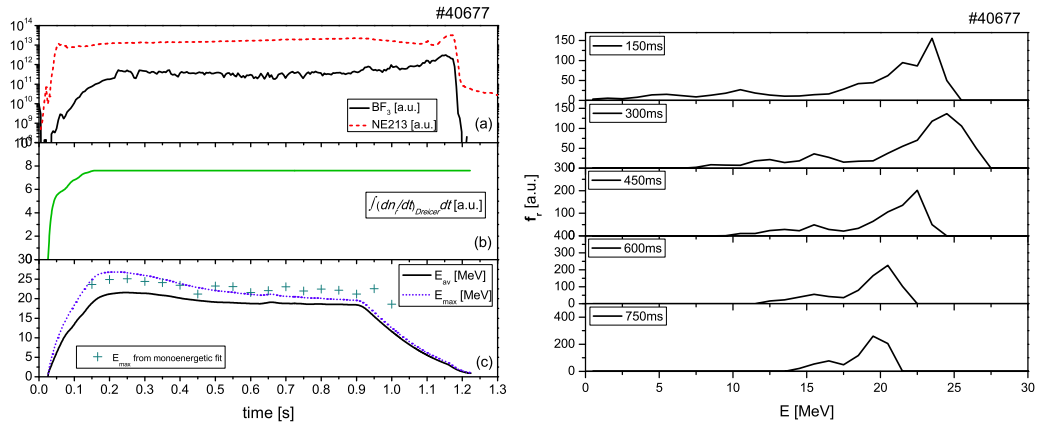

Figure 3.14: *For discharge # 40677: Left: (a) Time evolution of BF_3 and NE213 scintillator signals, (b) estimated runaway production, (c) maximum and average runaway energies. The green crosses correspond to estimates of the maximum electron energy using a monoenergetic fitting to the measured spectra; Right: Calculated runaway distribution function at different times.*

At the next step, the numerical tool PySYRUP (Python translation of SYRUP [54], [59]) has been employed for calculation of the synchrotron emission spectra using the simulated runaway distribution functions. This tool is equipped with various formulas for calculation of the synchrotron emission spectrum, both in a single particle picture and from a full RE distribution function, and in our case the approximations given by Eqs. (3.1) and (3.2) for the electron emitted power and brightness were chosen. The comparison of calculated spectra with the measurements at four different times during the discharge is shown in Fig. 3.15. Each time slice also includes the calculated spectra for the case of a monoenergetic beam with an energy and pitch angle

best fitting the measurements.

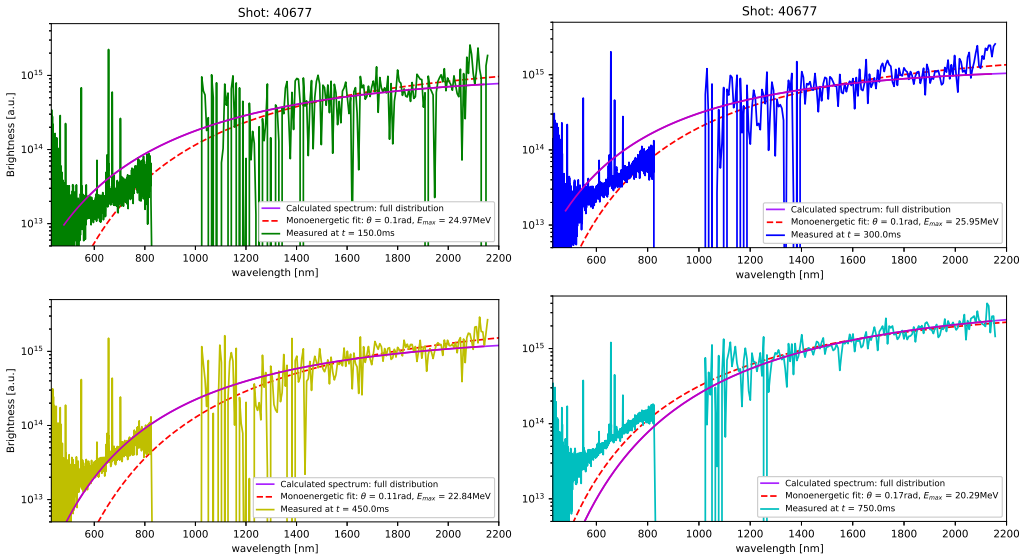

Figure 3.15: *Comparison between the measured and the calculated, using the full distribution function, synchrotron emission spectra for discharge # 40677 at four different times. The calculated spectra for a monoenergetic beam with an energy equal to the predicted maximum electron energy are also shown for comparison.*

The figure illustrates the difference between the calculations of the spectra using the full electron distribution and the monoenergetic case when the distribution function is broad. Only when the electron distribution becomes approximately monoenergetic (at 750 ms in the figure) the two calculations are closer. This suggests the need, for a correct interpretation of the synchrotron emission measurements, of taking into account the full electron distribution function [54]. Nevertheless, the monoenergetic case still yields sensible estimates of the maximum electron energy (green crosses in panel (c), Fig. 3.14). Fig. 3.15 also indicates a reasonable agreement between the calculations using the full electron distribution and the measurements until $\sim 500\,\text{ms}$. The discrepancy between the calculated and measured spectra at later times, mainly in the visible region of the spectra, is still unclear and is the subject of ongoing investigations. For example, underestimates in the calculated pitch angle could partially explain such a difference. Apart from the pitch angle estimate, several questions have to be addressed for the full

treatment of the REIS spectra, such as the field of view of the optical elements of the detectors, shape of the RE distribution function (the contribution of electrons with the highest energy is the most prominent), etc.

Chapter 4

Measurement of the critical electric field for runaway electron generation

"A scientist in his laboratory is not a mere technician: he is also a child confronting natural phenomena that impress him as though they were fairy tales."

Marie Curie

4.1 Introduction

Runaway electrons represent a major threat in the operation of tokamaks, especially when generated during disruptions, and the understanding of the conditions that lead to their generation is important in the design of systems capable to mitigate and suppress them.

As introduced in Sec. 2.2.2, when $E_{||}$ is below the critical electric field for runaway generation, E_R, all the existing runaway electrons are suppressed and eventually thermalised. For this reason, E_R is not only a relevant parameter describing the runaway dynamics, but it also has important practical implications. Methods for runaway electron suppression during disruptions by densification, using massive gas injection (MGI) or shattered pellet injection (SPI), aim to reach the critical electron density above which runaway electron generation is prevented ($E_{||} < E_R$) [36, 37, 60]. However, in a large

device as ITER, taking into account the present injection limits and the assimilation efficiency of the injected gas species (mainly Ar, Ne, He or D_2), it is still an open question if such a high density might actually be achieved. Moreover, for the case of argon or neon injection, because of the high cooling rate of these gases, the current quench time would be expected to fall below the eddy current limit, resulting in unacceptable forces on the ITER vessel and in-vessel components [37].

Runaway suppression experiments by means of Electron Cyclotron Resonance Heating (ECRH) in the flat-top phase of FTU discharges [28] found that the runaway electrons can be suppressed at electric fields substantially larger than those predicted by the relativistic collisional theory of runaway generation [Eq. (2.7)]. The results from an ITPA joint experiment to study the onset, growth, and decay of the runaway electrons during quiescent, flat-top conditions in several devices [61] also support evidence for a new threshold for runaway generation larger than the collisional threshold [10]. These findings suggest that, in addition to collisions, there are other runaway electron loss mechanisms that might be dominating the runaway dynamics in these experiments. On the other hand, it would imply that the required critical density for runaway mitigation might be significantly lower than expected on the basis of the relativistic collisional theory of runaway generation. Understanding the nature of such additional runaway loss mechanisms and whether this can be confirmed for disruption generated runaway electrons remain open issues.

This chapter describes experiments designed to evaluate the threshold electric field for runaway generation for a wide range of plasma parameters during the flat-top of ohmic (OH) discharges in FTU [62]. The critical conditions have been tested in two experimental scenarios: (1) runaway electron (RE) *onset* experiments, in which the density is decreased along the discharge until runaway electron generation occurs, and (2) runaway electron (RE) *suppression* of existing runaway electrons (created during a low density start-up) by gas injection. The experiments carried out and the methodology used for the estimate of the critical field are presented in Sec. 4.2 whereas the results are analysed and discussed in Sec. 4.3. In consistency with previous studies [28, 61], the measured threshold electric field is found to be substantially larger ($\sim 2-5$ times) than expected according to the purely collisional theory [Eq. (2.7)]. An investigation of the loss mechanisms which might explain these observations indicates that these results can be reason-

ably explained by an increase of the threshold electric field due to effect of the electron synchrotron radiation (Sec. 4.4), although in many cases additional energy losses still need to be invoked. The analysis carried out in Sec. 4.5 of the runaway electron dynamics in these experiments allows to get a quantitative estimate of such additional losses, found to be consistent with runaway electron losses due to radial diffusion for previously reported levels of magnetic turbulence in FTU [44]. Finally, the conclusions are summarised in Sec. 4.6.

Significant part of the content in this chapter has been published in articles listed in the Published and Submitted Content: G. Pucella et al., "Overview of the FTU results" (FTU Team and collaborators; includes Z. Popovic as a collaborator), *Nucl. Fusion* **55** *(2015) 104005*, Z. Popovic, B. Esposito, J.R. Martín-Solís et al., "On the measurement of the threshold electric field for runaway electron generation in the Frascati Tokamak Upgrade", *Phys. Plasmas* **23** *(2016) 122501*, and G. Pucella et al. (FTU Team and collaborators; includes Z. Popovic as a collaborator), "Overview of the FTU results", *Nucl. Fusion* **57** *(2017) 102004*, and B. Esposito, L. Boncagni, P. Buratti, D. Carnevale, F. Causa, M. Gospodarczyk, J.R. Martin-Solis, Z. Popovic et al., "Runaway electron generation and control", *Plasma Phys. Controll. Fusion* **59** *(2017) 014044*.

4.2 Runaway electron onset/suppression experiments

In FTU, the threshold electric field, E_{thr}, was evaluated during the plasma current flat-top phase of deuterium ohmic discharges in two types of experiments: (1) RE onset and (2) RE suppression experiments (Fig. 4.1).

In the RE *onset* discharges (Fig. 4.1, left), the electron density during the current ramp-up is set high enough to avoid runaway generation and, then, gradually decreased during the flat-top until the critical field value drops below the toroidal electric field and runaway electrons are generated. In contrast, during the RE *suppression* experiments (Fig. 4.1, right), the threshold electric field is crossed in the opposite sense: the discharge starts at very low density, allowing runaway electron generation, and is followed by an increase of the density to a high enough value for runaway electron

suppression, when the threshold field overcomes the accelerating electric field.

The critical time, t_c, for RE onset/suppression is determined by comparison of the BF_3 neutron detector and the NE213 neutron/gamma scintillator signals (Fig. 4.1). As it was explained in Chapter 3, during deuterium discharges with negligible runaway population, a perfect overlapping of the BF_3 and NE213 signals occurs, while in presence of runaways, the NE213 signal is contaminated by an excess of gamma-ray events and the NE213 scintillator signal no longer equals the BF_3 measurements [44]. Hence, in the RE onset discharges, the scintillator signal overlaps with the BF_3 chambers signal during the pre-RE phase and begins to diverge at the time (t_c) the runaway electrons are generated. The RE suppression experiments show a larger scintillator signal in the initial phase, indicating the presence of runaway electrons, while the two signals overlap at the time (t_c) when runaway electron suppression occurs. In order to obtain a more accurate estimate of t_c in these experiments, the difference between the logarithms of the BF_3 chambers and the NE213 scintillator signals, normalised to the logarithm of

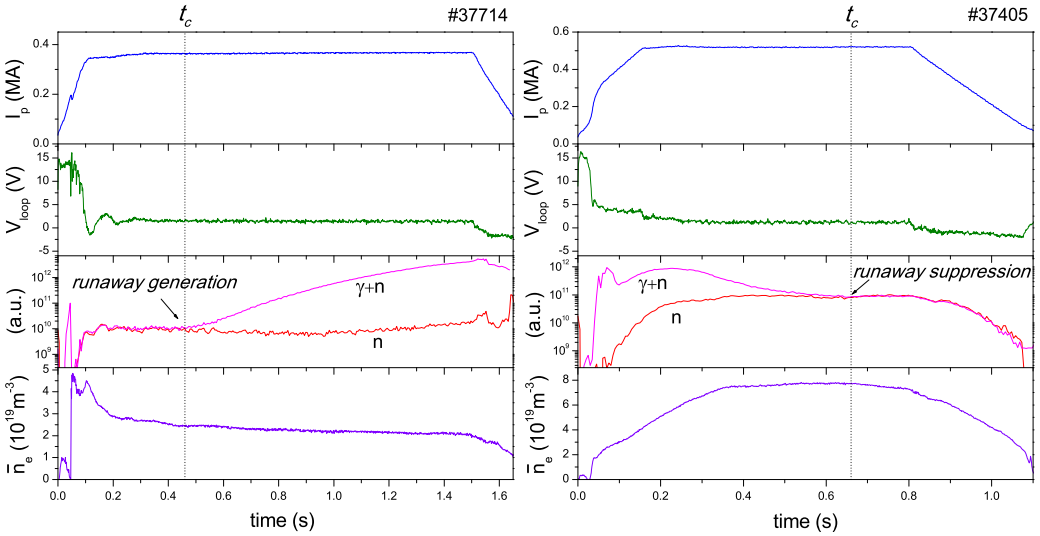

Figure 4.1: *Time traces of the plasma current (I_p), loop voltage (V_{loop}), NE213 ($\gamma + n$) and BF_3 (n) signals, and line-averaged central density for representative discharges: RE onset (left) and RE suppression (right) experiments.*

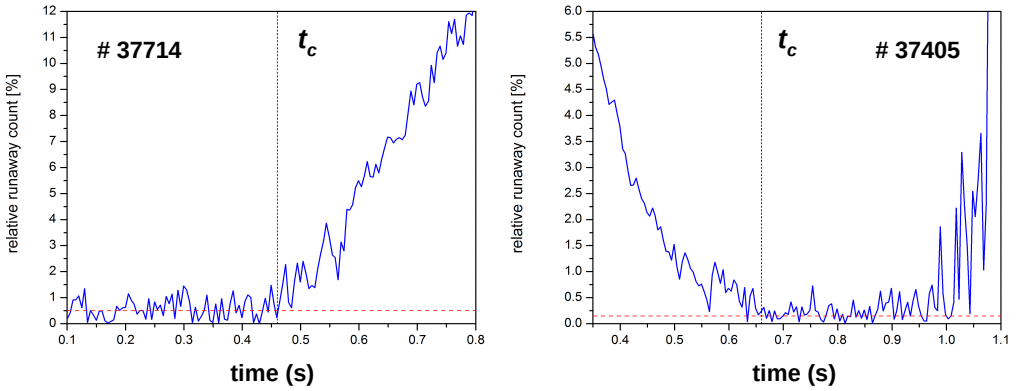

Figure 4.2: *Determination of the critical time, t_c, for RE onset (left) / suppression (right) discharges.*

the scintillator signal, is calculated and compared with the reference value before the runaway electrons are observed in the RE onset experiments, or after they disappear during the RE suppression discharges (Fig. 4.2).

Then, the threshold field is estimated as the value of the electric field at the critical time, t_c, that is, at the time when the runaway signal appears (disappears) in the onset (suppression) experiments, $E_{thr} \sim V_{loop}(t_c)/2\pi R_0$. It should be mentioned that there is an instrumental limit for the minimum amount of runaway electrons that can be detected, depending on the detector sensitivity. Thus, during the RE onset experiments, some runaway electrons might already exist in the plasma while the BF_3 and NE213 signals still coincide and, if so, the critical density (determined at t_c) would be underestimated and the measured E_{thr} (for a given density) would actually constitute an upper bound for the critical electric field. On the other hand, in the case of the RE suppression discharges, the critical electric field may be reached before the BF_3 and NE213 actually overlap as, once the critical density is reached, some time is required until the REs are slowed down and suppressed, implying that, in this case, the critical density would be overestimated and, therefore, the measured E_{thr} at a given density would constitute a lower bound for the actual threshold field. Thus, the combined use of the two separate methods, RE onset and suppression, gives the possibility to set, respectively, upper and lower limits for the critical electric field.

4.3 Data analysis and comparison with the classical collisional theory

The database includes 56 deuterium discharges covering a wide range of plasma parameters ($B_t \sim 2 - 7.2\,\mathrm{T}$, $I_p \sim 0.35 - 0.9\,\mathrm{MA}$ and $Z_{eff} \sim 1 - 13$). Fig. 4.3 shows the measured E_{thr} values as a function of the central line-averaged density, $\overline{n}_e$. Each point corresponds to a different discharge. The threshold field is in the range $\sim 0.1 - 0.4\,\mathrm{V/m}$ and the critical (line-averaged) density is typically $\sim 0.3 \times 10^{20}\,\mathrm{m}^{-3}$ for the RE onset experiments and $\sim (0.6 - 1.5) \times 10^{20}\,\mathrm{m}^{-3}$ for the suppression discharges, which is consistent with the discussion made at the end of the section above regarding the limitations of these methods for setting the threshold electric field and the critical density for runaway generation.

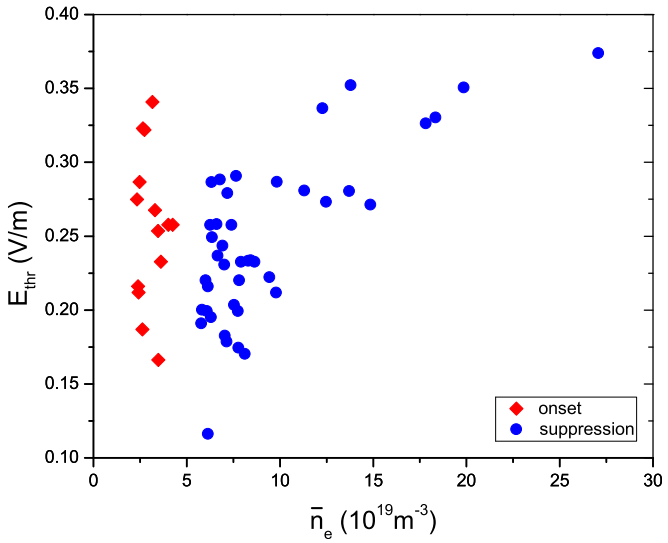

Figure 4.3: *E_{thr} versus central line-averaged density for the analysed set of discharges.*

As an initial comparison of the measured threshold electric field, E_{thr}, with the critical electric field, E_R, predicted by the relativistic collisional theory, the central line-averaged density has been used for the calculation of the threshold electric field. The results are shown in the Fig. 4.4. The measured critical electric field is found to be substantially larger ($\sim 2.5 - 9$ times) than E_R.

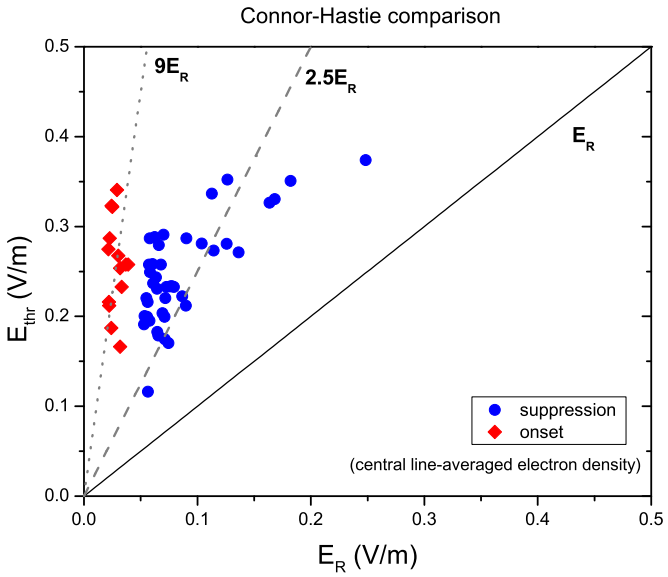

Figure 4.4: *Comparison of E_{thr} for the RE onset / suppression experiments with the relativistic theory, E_R, calculated using the central line-averaged density. Each point corresponds to a single discharge.*

However, for a more proper analysis of the parametric dependence of E_{thr} and its comparison with the theoretical predictions, it turns out to be adequate to use the local central electron density instead of the central line-averaged electron density as, typically, during ohmic discharges in FTU, runaway electrons are mainly created in the central part of the plasma column [44]. This is corroborated by measurements of hard X-ray radial profiles (using the HXR radial profile monitor described in Sec. 3.2) performed in the discharges of the present study. An example is shown in Fig. 4.5, corresponding to a RE onset experiment. The figure shows the time traces of the 6 hard X-ray line integrals (left, second panel) and the hard X-rays profiles obtained at two subsequent time slices (right) during the runaway generation phase. The observed hard X-ray emission, due to in-plasma bremsstrahlung of the runaway electrons, shows a peaking in the plasma center. Moreover, the hard X-ray line integrals from the lines of sight (LOS) traversing the plasma center (LOS #3 and #4) indicate the appearance of REs at roughly the same time ($\sim 0.5\,$s) as detected by NE213 scintillator (which provides no spatial information being located externally to the plasma vessel) indicating

the consistency between both runaway diagnostics. The scintillator signal shown in Fig. 4.5 (left, third panel) is purely due to hard X-rays, the neutron contribution (BF_3 time trace of Fig. 4.1) having been subtracted.

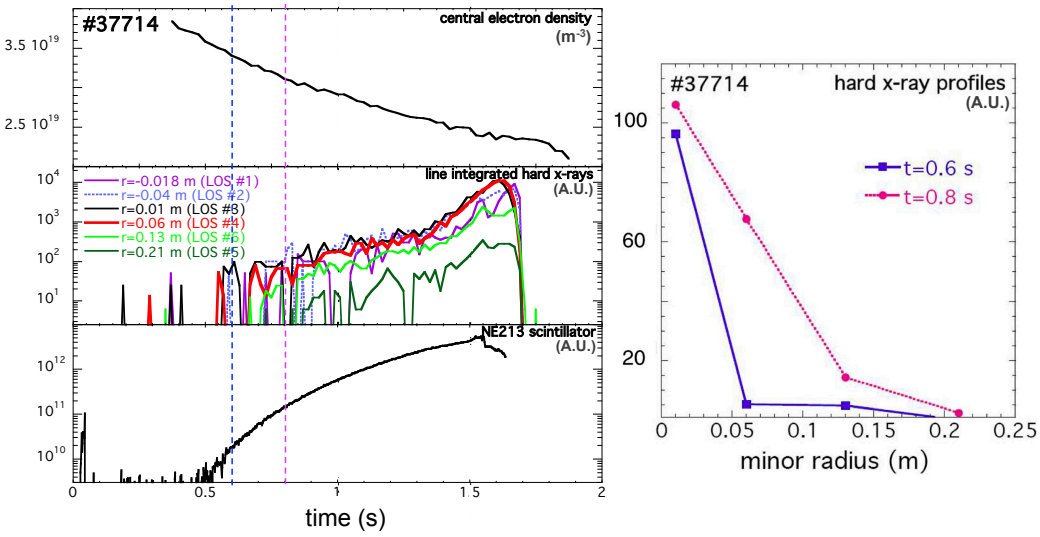

Figure 4.5: *FTU discharge #37714: Left: Time traces of central electron density, line-integrated hard X-rays (HXR radial profile monitor), and hard X-rays measured by NE213 scintillator; Right: Line-integrated hard X-ray profiles at t=0.6 s and t=0.8 s.*

Fig. 4.6 compares the measured threshold field in these experiments, E_{thr}, with the classical collisional prediction for critical electric field, E_R, using the local central electron density, n_{e0}, $E_R \propto n_{e0}$ [Eq. (2.7)]. The electron density data are produced by a CO_2 scanning interferometer, and n_{e0} is determined through a radial inversion technique [41] (left Fig. 4.5, first panel). The measured values of E_{thr} are typically in the range $E_{thr} \sim (2-5) \times E_R$, well above the values, E_R, foreseen by the relativistic collisional theory, suggesting that other runaway electron loss mechanisms, in addition to the classical collisional energy dissipation, are playing a role.

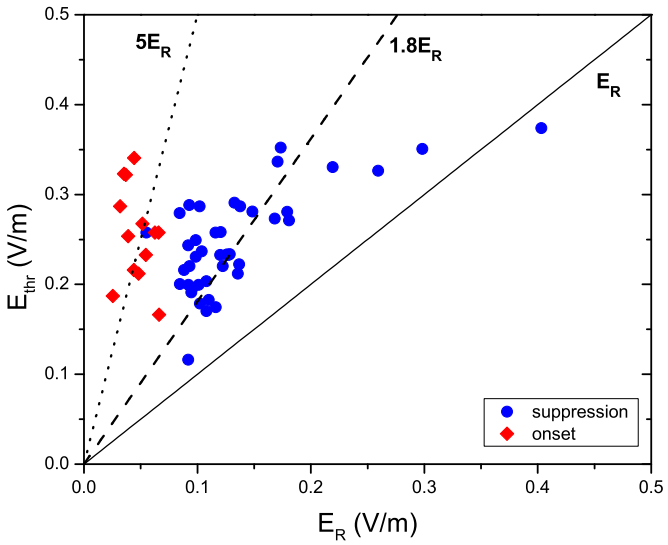

Figure 4.6: *Comparison of E_{thr} for the RE onset / suppression experiments with the relativistic collisional theory, E_R, calculated using the local central electron density. Each point corresponds to a single discharge.*

4.4 Synchrotron radiation losses

Although there are a number of loss mechanisms (electron radiation, drift orbit losses, turbulent transport, etc) that could be proposed to explain the discrepancy between the measured E_{thr} and the Connor collisional threshold, the synchrotron radiation due to the electron motion on toroidal paths and to the gyromotion of the runaways, having a finite pitch angle as a result of the collisions with the plasma particles and impurity ions, is always present and its effect on the critical field for runaway generation, as that of the collisional energy losses, therefore, must always be considered.

Thus, the classical collisional critical field, E_R, should be replaced by a new threshold, E_R^{rad}, which includes both the effect of the collisions and the electron radiation. Indeed, the increase in the threshold electric field for runaway generation including these effects has been addressed several times in the past [19, 63, 64] and has allowed to explain the observations made on runaway electron suppression during the flat-top phase of FTU ECRH heated discharges [28]. Moreover, it was experimentally found that such a

radiation threshold electric field constitutes an effective lower bound for the existence of runaway electrons in FTU [28].

This effect is illustrated in Figs. 4.7 and 4.8, which show the comparison between the measured E_{thr} and the critical field for runaway generation including the effects of radiation, E_R^{rad}, for the onset/suppression experiments here reported. The radiation threshold, E_R^{rad}, has been calculated following Eq. (2.30):

$$\frac{E_R^{rad}}{E_R} \simeq 1 + C(Z)\, F_{gy}^{\alpha},$$

an empirical fitting to the numerically calculated E_R^{rad} using the test particle approach introduced in Sec. 2.4.1, which agrees well with the estimates based on the kinetic approximation [64]. In this equation, Z is the ion charge which in plasmas with partially stripped impurity ions includes the effect of the scattering of the runaway electrons by the full nuclear and the electron-shielded ion charge of the impurity ions [65, 66]. For the analysed experiments, for which the electron temperature in the plasma center (where the runaway electrons are mostly located) is of a few keV, the impurities are highly ionised and Z can be roughly approximated by the effective ion charge Z_{eff}, deduced from visible bremsstrahlung measurements.

As described in the previous section, runaway electrons in FTU are mainly generated in the core region of the plasma and indeed the critical field values estimated using the local central electron density (Fig. 4.8) are showing a better agreement with experiment than the values calculated using the central line-averaged electron density (Fig. 4.7).

E_{thr} in Fig. 4.8 falls well within the range of critical fields predicted including the effect of the electron synchrotron radiation losses, $E_{thr} \sim (1.0 - 1.7) \times E_R^{rad}$. Furthermore, the equation above for E_R^{rad} [also Eq. (2.30)] shows a dependence on the plasma parameters (n_e, B_0 and $Z \equiv Z_{eff}$ in contrast to the dependence on n_e alone for E_R) which seems to be consistent with the measurements. This is illustrated in Fig. 4.9 in which the measured $(E_{thr}/E_R^{rad} - 1)$ is plotted as a function of $C(Z) \cdot F_{gy}^{\alpha}$ [definitions of $C(Z_{eff})$, F_{gy} and α are given in Sec. 2.4.2] for the analysed discharges. According to the equation for E_R^{rad} [Eq. (2.30)], $C(Z) \cdot F_{gy}^{\alpha}$ quantifies the deviation of E_R^{rad} from the collisional threshold and contains the dependences of E_R^{rad} on the plasma parameters [$C(Z) \cdot F_{gy}^{\alpha} \propto C(Z) \cdot B_0^{\alpha}/n_e^{\alpha}$, with $\alpha \sim 0.45$]. Fig. 4.9

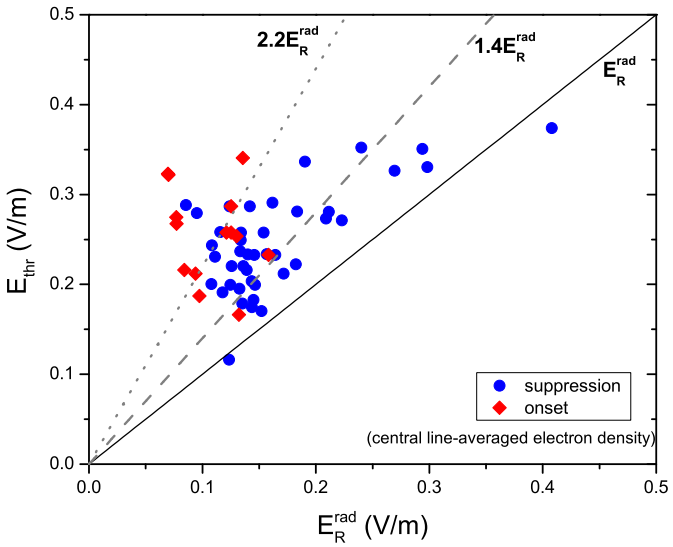

Figure 4.7: *Comparison of E_{thr} for the RE onset / suppression experiments with the relativistic theory, E_R^{rad}, calculated using the central line-averaged density. Each point corresponds to a single discharge.*

suggests that the predictions of the synchrotron radiation theory provide a good agreement with the measurements not only as far as the magnitude of the threshold electric field is concerned, but also the dependence of E_R^{rad} on the plasma parameters [Eq. (2.30)] reasonably agrees with the experiment.

The results shown in Figs. 4.8 and 4.9 also indicate that, although close, the measured E_{thr} is typically larger than E_R^{rad} [$\sim (1.0 - 1.7) \times E_R^{rad}$]. This behaviour is not unexpected, since the radiation threshold (E_R^{rad}) sets a minimum electric field below which no runaways can exist when collisions and radiation losses are considered. However, the presence of other loss mechanisms (such as radial runaway losses due to magnetic fluctuations [32], drift orbit losses, etc.) cannot be discarded, increasing even further the value of the threshold field for runaway generation, which is supported by a detailed analysis of the runaway electron dynamics in these experiments, shown in the following section.

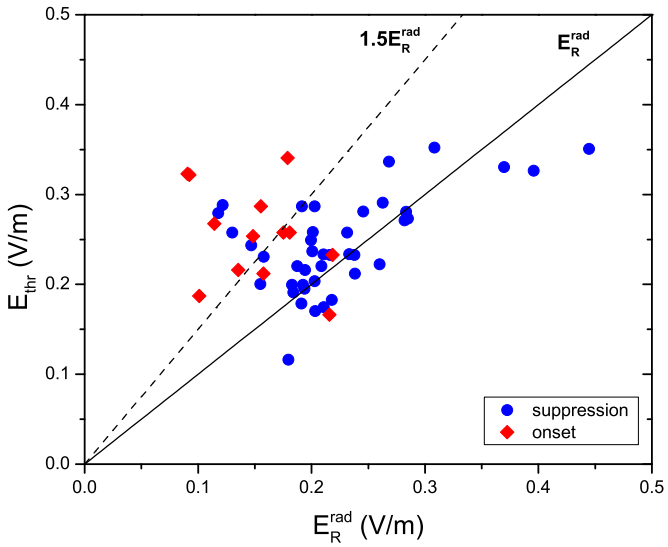

Figure 4.8: *Comparison of E_{thr} for the RE onset / suppression experiments with the radiation threshold, E_R^{rad}, calculated using the local central electron density. Each point corresponds to a single discharge.*

4.5 Runaway electron dynamics

Here, a detailed analysis of the runaway electron dynamics for the onset and suppression experiments will be carried out. The runaway electron production, energy and distribution function will be calculated. Its comparison with the existing observations will provide a useful insight on the behaviour of the runaway electrons in these discharges. In the case of the RE suppression experiments, this analysis allows the introduction of a quantitative estimate of the magnitude of the additional losses that must be invoked to explain the deviations of the measured E_{thr} from the radiation threshold field, E_R^{rad}.

Fig. 4.10 shows the results of the simulations for the RE onset discharge # 37714 (left Fig. 4.1). The runaway production [trace (b) in left figure] has been calculated according to the Dreicer mechanism (due to electron diffusion in velocity space at the critical velocity, as described in Sec. 2.3.1) by the expression [10, 14]

$$\frac{\mathrm{d}n_r}{\mathrm{d}t} = n_e \nu_0 \lambda(\varepsilon), \tag{4.1}$$

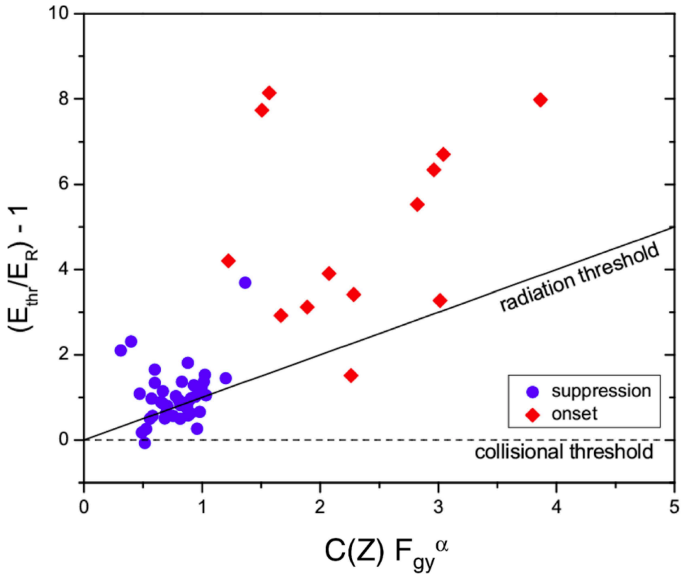

Figure 4.9: *For FTU RE onset / suppression discharges:* $\left(E_{||}/E_R^{rad}\right) - 1$ *versus* $C(Z) \cdot F_{gy}^{\alpha}$ *[$C(Z)$ and α defined in the text]. The full and dashed lines show the predicted radiation and collision threshold electric fields,* E_R^{rad} *and* E_R*, respectively.*

where n_r is the runaway density, ν_0 is the electron collision frequency, and λ is the runaway birth parameter, mainly determined by the parameter $\varepsilon \equiv E_{||}/E_D$, with $E_D = e^3 n_e \ln\Lambda/(4\pi\varepsilon_0^2 k T_e)$ [14]. Although it is not possible to make an absolute comparison between the calculated Dreicer growth rate and the runaway diagnostics signals, the runaway electron generation in FTU ohmic discharges is typically dominated by the Dreicer mechanism [44] and the resulting time evolution of $\int (\mathrm{d}n_r/\mathrm{d}t)_{Dreicer}$ [panel (b) in Fig. 4.10] for the runaway generation experiments is usually found to be consistent with the runaway measurements and estimated critical times for runaway generation [BF_3 and NE213 traces, panel (a)]. For the example shown in Fig. 4.10 ($E_{||} \sim 0.24\,\mathrm{V/m}, T_e \sim 3\,\mathrm{keV}, n_e \sim 3 \times 10^{19}\,\mathrm{m}^{-3}$), the parameter $\varepsilon \equiv E_{||}/E_D \sim 0.05$ should lead to a sizeable Dreicer runaway production [67].

Nevertheless, secondary generation cannot be discarded. As explained in Sec. 2.3.2, more runaway electrons can be produced due to Coulomb collisions between existing runaway electrons and thermal electrons which, as a result, become runaways. The characteristic avalanching time τ_s, calculated using

the approximation [68], is given by Eq. (2.14)

$$\tau_s \approx \frac{4\pi\varepsilon_0^2 m_e^2 c^3}{e^4 n_e}\sqrt{\frac{3(5+Z_{eff})}{\pi}}\left(\frac{E_{||}}{E_R}-1\right)^{-1},$$

which, in the case of the discharge in Fig. 4.10 yields $\tau_s \sim 0.7\,\mathrm{s}$, so that the secondary generation mechanism could contribute somewhat to the formation of the runaway population during the late phase of the discharge, although the runaway losses via radial diffusion, with a characteristic diffusion time for FTU ohmic discharges $\tau_d \sim 0.4\,\mathrm{s}$ [44], should prevent the exponential growth associated with the avalanche mechanism.

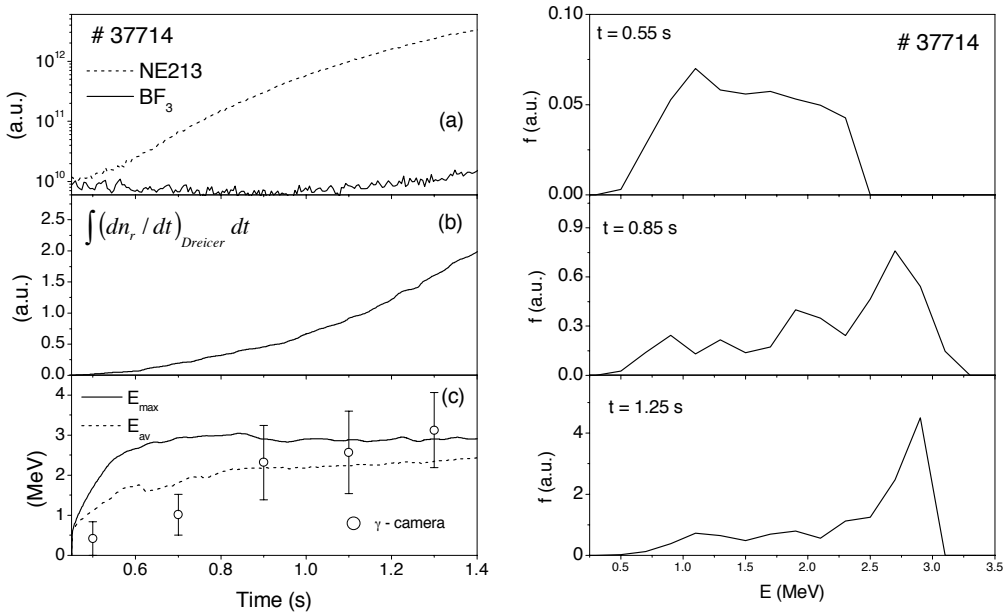

Figure 4.10: *For the RE onset discharge # 37714: Left: Time evolution of BF_3 and NE213 scintillator signals (a), estimated runaway production (b), calculated maximum and average runaway energies (c). The estimated maximum energy from the central chord of the hard X-ray profile monitor (open dots) is also shown for comparison; Right: Calculated runaway distribution function at 0.55, 0.85 and 1.25 s.*

The runaway energy distribution function, $f(E)$, has been estimated cal-

culating the energy evolution of the generated runaway electrons by means of the simple test particle description of the runaway dynamics (Sec. 2.4.1, [19]), including the electric field acceleration, collisions with the plasma particles and deceleration due to synchrotron radiation losses:

$$\frac{\mathrm{d}q_{||}}{\mathrm{d}\tau} = D - \gamma(1+Z_{eff}+\gamma)\frac{q_{||}}{q^3} - \left(F_{gc} + F_{gy}\frac{q_\perp^2}{q^4}\right)\gamma^4\left(\frac{v}{c}\right)^3\frac{q_{||}}{q} \quad (4.2)$$

$$\frac{\mathrm{d}q}{\mathrm{d}\tau} = D\frac{q_{||}}{q} - \frac{\gamma^2}{q^2} - \left(F_{gc} + F_{gy}\frac{q_\perp^2}{q^4}\right)\gamma^4\left(\frac{v}{c}\right)^3 \quad (4.3)$$

where, recalling, $q_{||}$, $q_\perp$ and q are the parallel, perpendicular and total electron momenta normalised to $m_e c$, v is the electron velocity and γ is the relativistic gamma factor [electron kinetic energy, $E = (\gamma - 1)\, m_e c^2$]; $\tau = \nu_r t$, with $\nu_r = n_e e^4 \ln\Lambda / 4\pi\varepsilon_0^2 m_e^2 c^3$; $D = E_{||}/E_R$ is the normalised electric field; F_{gc}, F_{gy} describe the two contributions to the radiation losses coming from the guiding centre motion and the electron gyromotion, respectively: $F_{gc} = F_{gy}(m_e c/eB_0R_0)^2$, $F_{gy} = 2\varepsilon_0 B_0^2/3n_e \ln\Lambda m_e$.

The first term in these equations corresponds to the acceleration due to the toroidal electric field, and the second term includes the effect of the collisions with the plasma particles [23]. The third term describes the synchrotron radiation losses [19].

At each time step, the runaway electrons are assumed to be generated at the lowest energy $\gamma_0 > \gamma_c$ (γ_c: critical energy for runaway generation) and, then, the runaway distribution function at time t is formally given by:

$$f(\gamma, t) = \int_0^t \frac{\mathrm{d}n_r}{\mathrm{d}t'}(\gamma_0, t')\,\mathrm{d}t', \quad (4.4)$$

where $t = 0$ denotes the start of the runaway generation process and the integration is carried out over the times t' for which an electron generated with energy γ_0 would have gained, according to the test particle equations, an energy γ at time t. The resulting distribution function at three different times during the discharge is plotted in right Fig. 4.10. The distribution function is broad, extending up to the maximum runaway energy at each time step, and showing a trend along the discharge to accumulate close to the limiting energy $\sim 3\,\mathrm{MeV}$.

Trace (c) in left Fig. 4.10 shows the time evolution of the calculated

maximum electron energy, E_{max}, and the average runaway energy,

$$E_{av} = \frac{\int_{\gamma_0}^{\gamma_{max}} (\gamma - 1) m_e c^2 \, f(\gamma) \, d\gamma}{\int_{\gamma_0}^{\gamma_{max}} f(\gamma) \, d\gamma}, \tag{4.5}$$

$[E_{max} = (\gamma_{max} - 1) \, m_e c^2]$.

Initially, E_{max} is noticeably larger than E_{av} and, later in the discharge, once the electrons start to accumulate close the limiting energy, E_{max} and E_{av} get closer. The maximum measured gamma energy determined from the end points of the gamma ray spectra for the central chord of the gamma camera is also shown as function of time in trace (c) in the figure and can be assumed to describe the time evolution of the maximum runaway energy. Despite of the large uncertainties, to a great extent associated to the relatively low number of gamma counts (particularly for the earlier times in the discharge) which prevent to get more accurate estimates, the measurements seem to be consistent with the calculations.

A second example of a RE onset discharge is illustrated in Fig. 4.11. In this case, the simulations suggest a large electron energy increase (up to $\sim 30 - 40\,\mathrm{MeV}$) during the RE generation phase which is supported by measurements of the REIS system. Hence, Fig. 4.12 shows the measured synchrotron radiation spectra at three different times during the discharge (1.3, 1.4 and 1.5 s). The spectra are fitted (black solid lines) using formula (1) from Ref. [54] for the power radiated by the electron. For the aim of a simple estimate of the maximum electron energy, the synchrotron emission from a single electron is used as an approximation (Chapter 3), using a specific value of the momentum and pitch-angle identified as the maximum momentum and pitch-angle of the runaway electrons. The electron pitch angle ($\theta \sim 0.1\,\mathrm{rad}$) is obtained from the test particle simulations of the runaway dynamics and the maximum electron energy is given by the values best fitting the spectra (see insert in Fig. 4.12) which are found to be consistent with the predictions of the simulations based on the test particle model (energy $\sim 30{-}40\,\mathrm{MeV}$). The large energy reached by the electrons in this discharge in comparison with # 37714 ($\sim 3\,\mathrm{MeV}$) is due to the larger accelerating electric field ($\sim 0.4\,\mathrm{V/m}$ vs. $\sim 0.25\,\mathrm{V/m}$ for # 37714) and to the lower synchrotron radiation losses as a result of the smaller magnetic field (3.7 T vs. 6 T, respectively), and a lower

(nearly half) Z which reduces the collisionality and, hence, the electron pitch angle and the synchrotron radiation associated with the electron gyromotion.

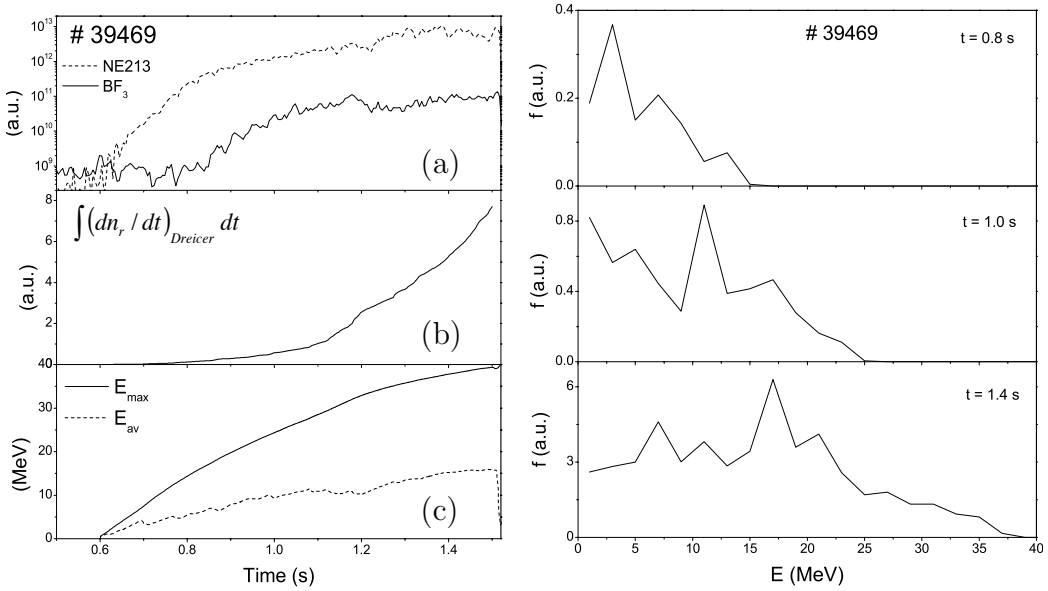

Figure 4.11: *For the RE onset discharge # 39469 ($I_p = 0.37\,\mathrm{MA}$; $B_t = 3.7\,\mathrm{T}$): Left: Time evolution of BF_3 and NE213 scintillator signals (a), estimated runaway production (b), calculated maximum and average runaway energies (c); Right: Calculated runaway distribution function at 0.8, 1.0 and 1.4 s.*

The RE suppression experiment and modelling are presented in Fig. 4.13. The runaway electrons are generated in the beginning of the discharge (due to the large electric field and low density, as shown in Fig. 4.1) and the runaway production stops soon during the current ramp-up at $\sim 0.15\,\mathrm{s}$ [panel (b) in left figure] when $E_{||}$ decreases and the density increases. Initially, the runaway energy rises up to $\sim 4\,\mathrm{MeV}$ [panel (c)] and decreases later on along the discharge, when the density increases until the runaway electrons are suppressed. As the runaway production stops early in the discharge ($\sim 0.15\,\mathrm{s}$), the distribution function rapidly evolves towards a monoenergetic beam (right pictures) with an average energy equal to the maximum runaway energy [left Fig. 4.13 (c)]. As discussed in Sec. 4.4, for a substantial number of discharges, the collisions and the electron radiation cannot account for all the runaway losses (typically $E_{thr} > E_R^{rad}$) suggesting that additional energy

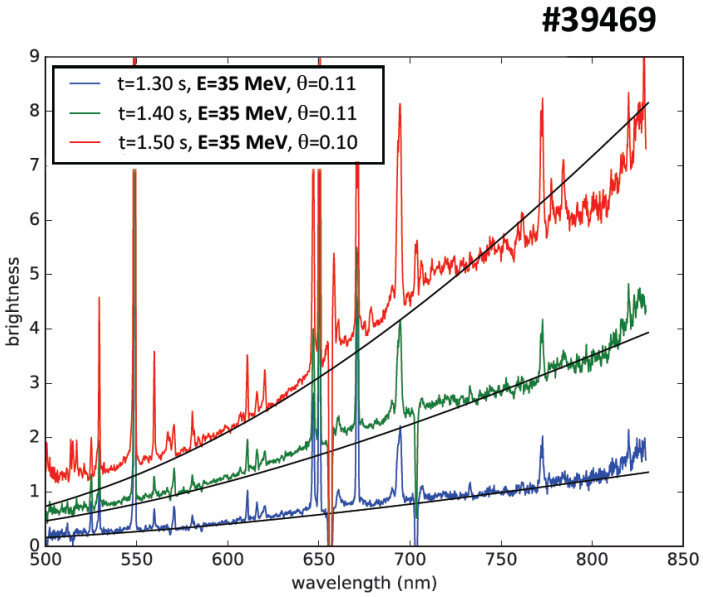

Figure 4.12: *Synchrotron radiation spectra for the RE onset discharge # 39469 at 1.3, 1.4 and 1.5 s. Best fittings to the spectra (black solid lines) and the parameters used (electron energy and pitch angle; see insert in the figure) are also shown.*

dissipation mechanisms should be playing a role. Indeed, in the simulations shown in Fig. 4.13, a loss term $-\vec{q}/\tau_d$ ($\tau_d \sim 0.14\,\mathrm{s}$ in the figure) must be included in the test particle equations in addition to the collisional and radiation losses for consistency with the inferred runaway suppression from the BF_3 / NE213 signals [panel (a) in left figure]. If no additional RE losses were considered ($\tau_d \to \infty$; red line in the figure), the runaway electrons would not be suppressed and at $\sim 0.8\,\mathrm{s}$ the runaway electron energy would still be $\sim 3\,\mathrm{MeV}$. As in Fig. 4.10, the open dots in panel (c) indicate the estimates of the maximum electron energy from the central line of sight of the hard X-ray profile monitor. The measurements agree reasonably well with the simulations up to $\sim 0.4\,\mathrm{s}$. The last experimental point (at 0.7 s) has a large error bar (the number of counts is very low), but compatible with the zero energy (i.e. runaway suppression) expected by the overlap of the BF_3 and NE213 time traces.

The empirical dissipation time, τ_d, constitutes a quantitative measure-

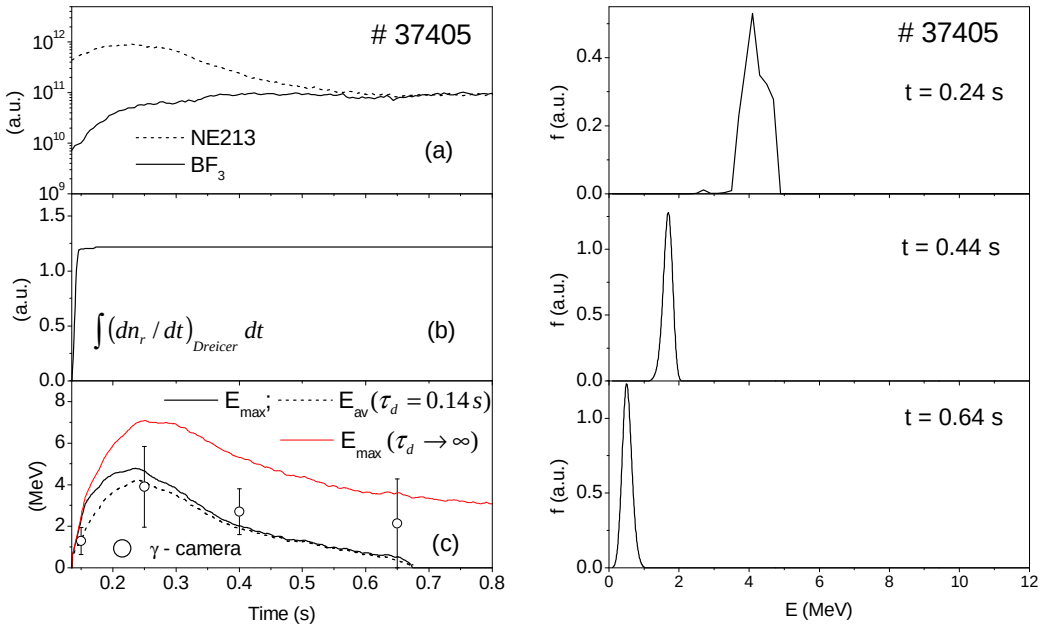

Figure 4.13: *For the RE suppression discharge # 37405 ($I_p = 0.52\,\mathrm{MA}$; $B_t = 6\,\mathrm{T}$): Left: (a) Time evolution of BF_3 and NE213 scintillator signals, (b) estimated runaway production, and (c) calculated maximum and average runaway energies including additional energy losses ($\tau_d = 0.14\,\mathrm{s}$; black lines). The red line indicates the predicted runaway energy assuming no additional loss mechanisms ($\tau_d \to \infty$) for which no runaway suppression would be predicted. The estimated maximum energy from the central chord measurements of the hard X-ray profile monitor (open dots) is also shown for comparison; Right: Calculated runaway distribution function at 0.24, 0.44 and 0.64 s.*

ment of the unknown energy loss mechanisms which should be taken into account in addition to the collisions and the electron synchrotron radiation to explain the observed runaway suppression in these experiments. The estimated values of τ_d for the set of analysed discharges typically lie in the range $\sim 0.05 - 0.3\,\mathrm{s}$.

Among the mechanisms which could be proposed to explain these additional losses, quantified by means of τ_d, the radial diffusion of the runaway electrons, mainly due to magnetic fluctuations, has been often assumed to account for the observed anomalous runaway losses in many devices [50, 69],

which indeed might increase the value of the threshold electric field for runaway generation [32, 27]. There is no direct evidence for such a magnetic turbulence in these experiments, but measurements of the radial runaway diffusion coefficient in FTU ohmic discharges have provided estimates of the level $\tilde{b} \equiv \tilde{B}_r/B_0$ of the radial magnetic turbulence $\sim 10^{-5}$ [44]. Indeed, if it is assumed that the energy dissipation time, τ_d, in these experiments is determinad by the radial loss of the runaway electrons, a runaway diffusion coefficient can be deduced, $D_r \sim a^2/5.8\tau_d$ [32], yielding $D_r \sim (0.05 - 0.3)\,\mathrm{m}^2/\mathrm{s}$, which is in consistency with previous measurements made in FTU [44] as well as in other tokamaks [50, 69]. From D_r, a simple estimate for $\tilde{b}$ can be obtained using the theoretical prediction for the diffusion coefficient $D_r \approx \pi q R_0 \tilde{b}^2 v_{||}$ [33], where q is the safety factor and $v_{||}$ is the runaway velocity parallel to the toroidal magnetic field, yielding $\tilde{b} \sim 10^{-5}$, also consistent with the values previously reported in FTU ohmic discharges [44]. The large drift displacement of the runaway electrons when their energy increases can decouple them from the field lines and so reduce their sensitivity to the magnetic turbulence [70, 71] and the resulting radial diffusion losses. The corrections to D_r due to drift orbit averaging depend on the relation between the runaway drift displacement and the radial correlation length of the turbulence. The runaway drift can be estimated by $d_r \approx m_e \gamma v_{||} q/eB_0$ which, assuming a typical runaway energy for the discharges for which τ_d was determined $\sim 3\,\mathrm{MeV}$ (Fig. 4.13), would lead to $d_r \sim 2\,\mathrm{mm}$. On the other hand, the correlation length, σ, of the turbulence can be approximated by $1/m$, where m, the poloidal number of the fluctuations, is given roughly by $m \simeq a/\rho_i$ (ρ_i is the ion Larmor radius) which, for the discharges considered ($T_i \sim T_e \sim 1-3\,\mathrm{keV}$) would yield $\sigma \sim 3 - 4\,\mathrm{mm}$. Hence, the runaway drift orbit displacement would be of the order or smaller than the radial correlation length of the turbulence, and large corrections due to drift orbit averaging effects should not be expected.

In summary, the estimated level of the magnetic fluctuations required to account for τ_d in these experiments (and so for the increase of E_{thr} over E_R^{rad}) would be consistent with the estimated values of $\tilde{b}$ inferred from the measured runaway radial diffusion coefficient in FTU ohmic discharges [44]. On the other hand, losses associated with the outward drift of the electron orbit when its energy increases do not seem to play a significant role in most cases. As discussed above, the magnitude of the runaway drift is typically only of a few mms and most of the runaway electrons are located in the

central region of the plasma in these experiments. Nevertheless, other loss mechanisms (such as, for example, kinetic instabilities) cannot be completely discarded.

4.6 Summary

Dedicated experiments on RE onset and suppression have been carried out in the FTU tokamak in order to determine the threshold electric field for runaway generation during the flat-top phase of ohmic discharges.

More precisely, taking into account the sensitivity of the runaway detectors and the limitations of the methodology employed, the use of the two separate methods allows to provide upper (RE onset) and lower (RE generation) limits for the threshold field E_{thr}. It is found that the critical field for runaway generation measured in FTU is $\sim 2-5$ times larger than expected according to the relativistic collisional theory [10]. These results are in agreement with a recent ITPA joint experiment carried out in several tokamaks [61] and suggest that other runaway electron energy loss mechanisms, in addition to collisions, should be playing a role and explain the differences with the classical theory. Indeed, the results found for E_{thr} reasonably agree with an improved estimate of the threshold electric field for runaway electron generation, E_R^{rad}, which includes the effect of the losses always present due to the collisions and electron the synchrotron radiation [19, 63, 64], $E_{thr} \sim (1.0-1.7) \times E_R^{rad}$, confirming earlier results from FTU RE suppression experiments by means of electron cyclotron resonance heating [28]. Moreover, not only the measured E_{thr} is closer to E_R^{rad} but the predicted dependence of the new threshold electric field on the plasma parameters also matches reasonably well with the experimental data.

Nevertheless, even taking into account the electron synchrotron radiation, the measured threshold field, E_{thr}, although close, is often found to be larger than E_R^{rad} and simulations of the runaway energy dynamics (runaway energy and distribution function) during the RE suppression experiments confirm that additional losses should be considered in order to reproduce the observed runaway suppression. The simulations indicate that the characteristic dissipation time, τ_d, describing the unknown additional losses is in the range $\sim 0.05-0.3\,\mathrm{s}$ and that, if these are assumed to be due to anomalous radial losses driven by the underlying magnetic turbulence, the

radial diffusion coefficient describing the radial runaway transport should be $D_r \sim (0.05 - 0.3)\,\mathrm{m}^2/\mathrm{s}$ and the corresponding radial magnetic fluctuation level $\tilde{b} \sim 10^{-5}$, consistent with values previously reported in the core region of FTU ohmic discharges [44], although it cannot be completely discarded that other loss mechanisms (such as, for example, kinetic instabilities) might be playing a role.

These experiments, together with those performed within the ITPA joint experiment on low density flat-top runaway electron discharges [61], would imply that the required critical density for runaway mitigation might be noticeably lower than expected on the basis of the relativistic collisional theory of runaway generation, but it is still an open issue if these results can be confirmed for disruption generated runaway electrons.

Chapter 5

Runaway electron control in FTU

"The scientific man does not aim at an immediate result. He does not expect that his advanced ideas will be readily taken up. His work is like that of the planter - for the future. His duty is to lay the foundation for those who are to come, and point the way. He lives and labours and hopes."

Nikola Tesla

For safe and efficient operation of large devices of ITER type the planned scenarios should be carried out so that the critical RE parameters are outside of the range for runaway generation, or that only insignificant amounts of runaway electrons arise. Nonetheless, rectifying methods and damage reduction are required during undesirable outcomes such as disruptions [37], especially in cases when RE beams carrying substantial currents are formed. In ITER, the stored energy in plasma discharges will be greater than in current tokamaks and, according to estimates, runaway electron currents over 2 MA are regarded as potentially intolerable [4].

The main strategies for disruption RE mitigation are: (i) RE mitigation by means of massive gas injection (MGI) or shattered pellet injection (SPI) of high-Z impurities [18, 72, 73], which also reduces localised heat loads before the thermal quench (TQ), (ii) resonant magnetic perturbations (RMP) to suppress REs [74, 75, 76], and (iii) RE active control aiming to dissipate the energy of the RE beam and to diminish the RE population [77, 39, 78]. Although the injection of high-Z impurities constitutes the most promising

scheme for RE mitigation and control, it has the disadvantage of needing accurate disruption predictors and reliable injection mechanisms, while it may also lead to hot tail RE generation [17]. In ITER, the disruption mitigation systems must prevent runaway electron seed formation that could possibly be amplified through avalanche by a factor orders of magnitude higher than in present tokamaks. Further, densification via MGI or SPI would require reaching critical density of $\sim 3 \times 10^{22}\,\mathrm{m}^{-3}$, which is unlikely to be achieved without adequate assimilation of the injected impurities (assimilation in existing experiments with MGI is under 20% [37]). On the other hand, magnetic perturbations imposed by special external coils have resulted in successful prevention of a RE beam formation over a specific perturbation amplitude threshold [67, 74], but the predictions of perturbations for ITER [79], introduced by the in-vessel coils designed for edge localised mode mitigation, prove to be inadequate for RE suppression.

In FTU, dedicated experiments to RE suppression by injection of high-Z impurities, by MGI (SPI systems are not available) have not been carried out, and specific active coils for RMP experiments have not been installed. In contrast, experiments dedicated to the RE active control represent one of the most important areas of investigation done in FTU [4, 80]. In this chapter, a brief overview is given of the work done in collaboration with the FTU active control team, which includes my participation as a member of the team in charge of the experimental planning and execution.

Part of the content in this chapter has been published in articles listed in the Published and Submitted Content: B. Esposito, L. Boncagni, P. Buratti, D. Carnevale, F. Causa, M. Gospodarczyk, J.R. Martin-Solis, Z. Popovic et al., "Runaway electron generation and control", *Plasma Phys. Controll. Fusion* **59** *(2017) 014044*, D. Carnevale et al. (EUROfusion MST1 Team, includes Z. Popovic as a collaborator), "Runaway electron beam control", *Plasma Phys. Controll. Fusion* **61** *(2019) 014036*.

The RE active control refers to the stabilisation of the RE beam generated during disruptions, with the aim of reducing the beam interaction with the inner components of the vessel and the RE energy dissipation on the PFCs. It is done so by controlling the position of the RE beam formed by the electrons that remain runaway after the CQ. The RE current is minimised inductively by the central solenoid (as in [77]), decreasing the energy of REs in the process. RE mitigation strategies include MGI or SPI when a stable

control of the RE beam is achieved, which would intensify the RE radiative losses and diminish the runaway population.

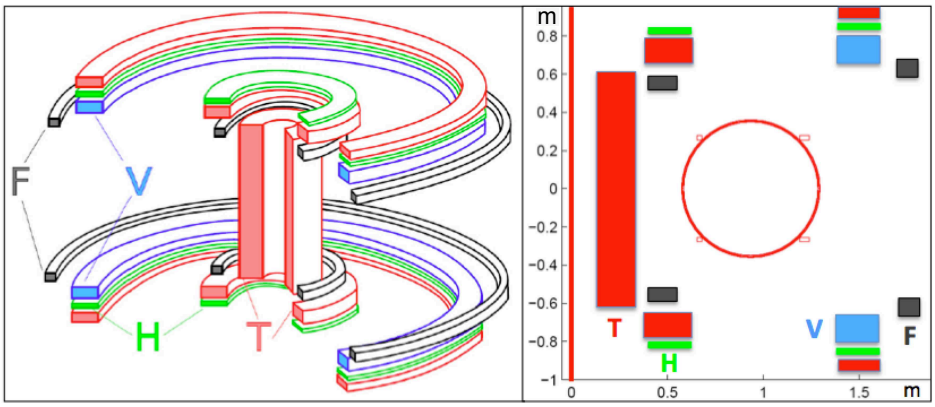

Figure 5.1: *Active FTU coils: central coil T controls the plasma current I_p, V and F coils control the radial movements and elongation of the plasma column, while H coil controls the plasma column vertical position. Image from [4].*

In FTU RE active control studies [4], the post-disruption RE beams are dissipated through inductive effects from the central coil, together with a new dedicated tool in the plasma control system (PCS) of the tokamak [81]. The PCS scheme provides the radial position control and current ramp-down of the RE beam, where the efficiency of the approach is evaluated by the reduced interaction of REs with the PFCs. In the past several years, two novel real-time (RT) algorithms for position and plasma current ramp-down control of disruption-generated REs have been developed in FTU, implemented within the FTU PCS framework, and tested in dedicated FTU plasma discharges. It has been shown that RE beam energy is suppressed and the interactions with the vessel significantly alleviated (especially on the low-field side) by means of a slow I_p ramp-down (~ 1 MA s^{-1} up to 200 ms) and a reduction of plasma external radius ($\sim 10\%$ of the flat-top value). A more detailed description of the algorithms and examples of their application in FTU experiments can be found in Ref. [4]. Fig. 5.1 shows the active coils employed for the control of the plasma current and position. The central solenoid, the T coil, imposes the I_p via inductive effects, and the PCS couples the current flowing through the coil with a feedback control scheme driven by the I_p error plus a pre-

programmed signal. The horizontal position of the plasma is regulated in combination with on-line processing of a series of pick-up coil signals that determine the plasma boundary (last closed magnetic surface) and compare it along the equatorial plane to the reference plasma internal and external radii [82, 83, 84, 85]. Due to geometrical arrangement, the F and V coils in Fig. 5.1 create vertical fields, allowing to vary the plasma elongation and, through current redistribution between the two coils, maintain the vertical and radial position of the plasma at run-time [4]. Safety limits based on the HXR detector signal are imposed by the PCS in case that a certain safety threshold value is exceeded for over 10 ms, which would indicate that harmful REs are present. In such cases, the discharge is shut-down by a standard shut-down control algorithm, that decreases the I_p reference exponentially down to zero, while keeping the reference inner and outer plasma radii at the equatorial plane unchanged.

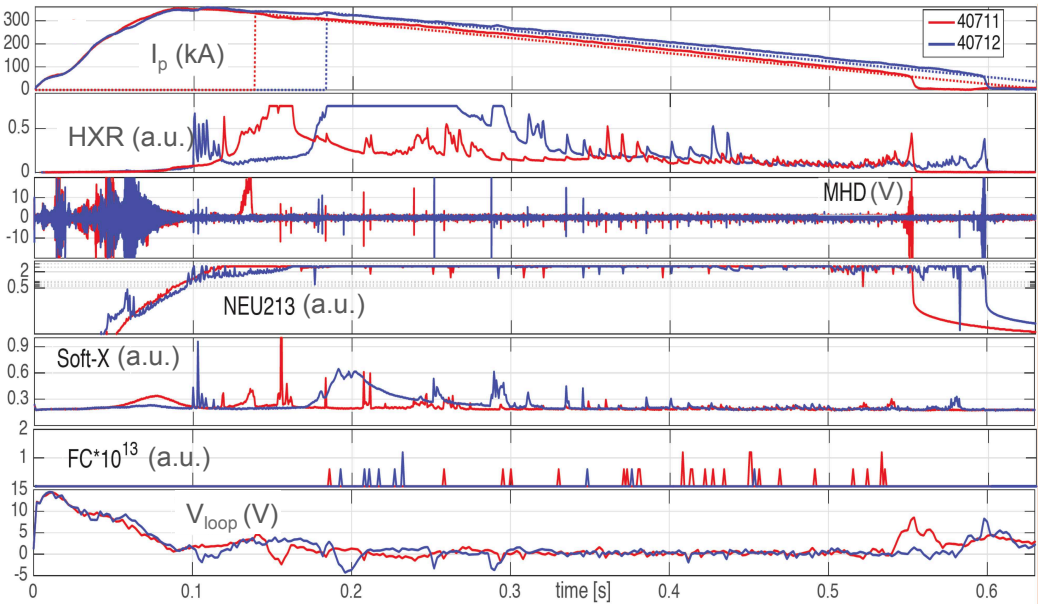

Figure 5.2: *FTU examples of soft-stop for plasmas with high level of REs. Figure Ref. [86].*

Fig. 5.2 illustrates two soft-stop experiments in FTU. "Soft-stop" refers to the control and current ramp-down of the plasma when a substantial amount of runaway electrons is indicated by a high level of HXRs. In RE control

experiments, additional diagnostics are used, such as: ^{235}U fission chambers (FC), indicating the presence of gamma rays with energies over 6 MeV, soft X-ray (SXR) acquired by a multichannel bolometer detecting X-rays in the range 5 eV to 10 keV, an additional HXR scintillator, for monitoring X-rays with energy higher than 200 keV, and a Mirnov coil [87], in which the amplitude of the signal is directly related to helical deformations of the plasma resulting from MHD instabilities. The HXR signal in the second panel of Fig. 5.2 saturates as a result of RE interactions with the vessel and high-Z ions of the plasma when the trigger occurs. The scintillator (NE213) signal increases up to the saturation level suggesting a substantial number of runaway electrons after 0.1 s (fourth panel). A decrease in the RE population and energy as a result of the control of the RE beam is indicated by the lower HXR signal level (second panel) after $\sim$ 0.2 s and $\sim$ 0.3 s for the discharges # 40711 and # 40712, respectively, and which continues along the I_p ramp-down, while MHD induced RE losses are correlated with SXR spikes, as seen by the corresponding traces in the third and fifth panels of Fig. 5.2. The RE energy decrease along the ramp-down is confirmed by fitting of the spectra acquired with the REIS system, presented in Fig. 5.3, keeping the assumption of a monoenergetic distribution.

Post-disruption RE beam control and suppression performed in selected FTU experiments [86] is shown in Fig. 5.4. In the first panel, the I_p is depicted in solid lines, while the dotted lines represent the new current references (instead of a previous constant upper reference value of 360 kA) when the CQ is detected, clearly showing an improved tracking performance during the current ramp-down. The time traces of the HXR and FC detectors, given in the second and third panels of Fig. 5.4, indicate that a large and energetic RE population is present during the CQ, a part of which is lost in the initial part of the RE plateau phase, causing saturation of HXR and high levels of FC signals. As the remaining RE beam current decreases, the FC signal does not feature the termination peak (except in the discharge # 39903), which is usually observed in discharges without the RE controller and corresponds to the final RE loss to the PFCs, even in the discharges # 38513 and # 38519 with larger current drops. The lack of the FC peak during the current termination means that the energetic runaway electrons are not present anymore. Unlike in the case of the discharge # 39903, where the thermalisation of REs was not achieved and the RE losses on the vessel structures saturate both HXR and FC signals, the current ramp-down in

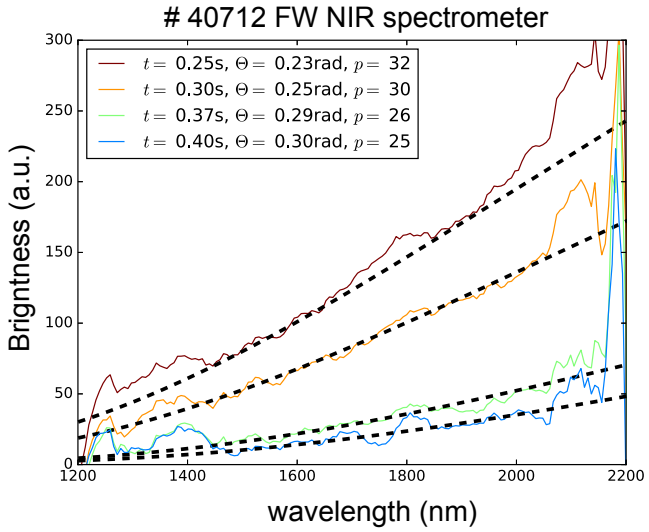

Figure 5.3: *Monoenergetic fitting of synchrotron emission spectra obtained in the RE forward direction with the near-infrared (NIR) spectrometer of the REIS system for the soft-stop discharge # 40712 (the values used for the electron pitch angle, θ, and the normalised (to $m_e c$) electron momentum, p, for the monoenergetic fitting of the spectra at each time are also included).*

the other three discharges was slow enough and with low values of the loop voltage to ensure the RE energy suppression. Frequent MHD mode activity (fourth panel of the figure) in the pulse # 40714 also caused RE expulsions, noted in the HXR time trace. Keeping low values of the loop voltage, by controlling the current of the central solenoid, is the key for achieving the suppression of REs during the current ramp-down in control experiments while the stabilisation of the RE beam is accomplished [86].

Although further investigation is needed, RE active control is considered as alternative/complementary technique to MGI and SPI. Moreover, the real-time methods enable improvement of the estimate of the RE beam radial position and, in addition, the development of diagnostics and tools for more robust runaway beam suppression strategies.

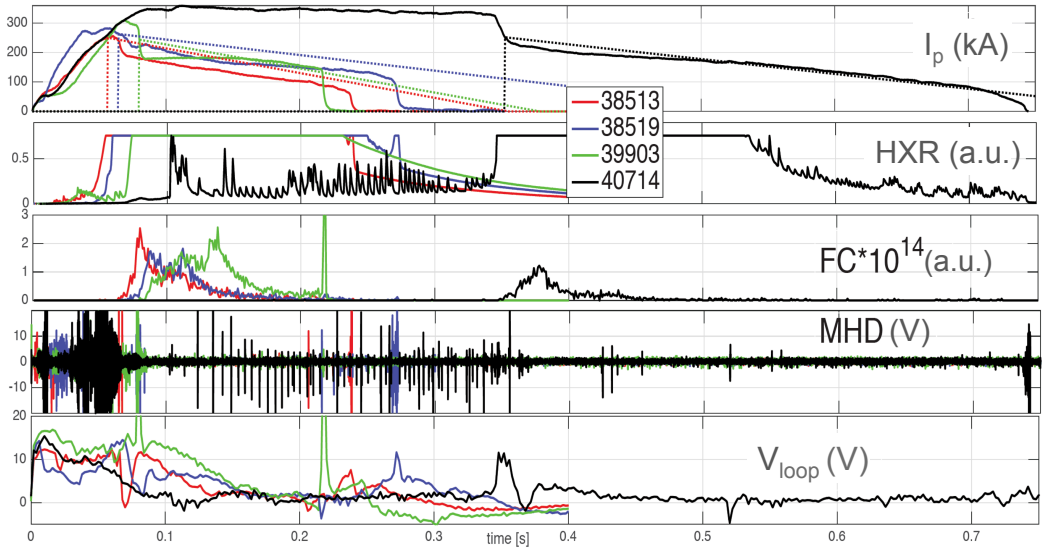

Figure 5.4: *FTU disruptions where post-disruption RE beam control and suppression was achieved with the central solenoid and the new FTU control system. Figure credit [86].*

CHAPTER 5. RUNAWAY ELECTRON CONTROL IN FTU

Part III

Conclusions

Chapter 6

Conclusions and future work

"Living is worthwhile if one can contribute in some small way to this endless chain of progress."

Paul Dirac

This thesis has addressed a few central questions related to the runaway electrons in tokamak plasmas, specifically in the FTU tokamak. The main focus has been directed towards the high-priority issues linked to the ITER project within the FTU experimental campaigns, namely the study of RE energy and distribution combining diagnostic and numerical tools, estimates of the critical electric field for the runaway electron generation, and the post-disruption RE beam current active control and suppression. Here, in the third and final part of the thesis, we gather the most relevant conclusions drawn from this work and call attention to the future work and some open questions.

After a revision of the basic concepts and the physics of runaway electrons was given in the Part I of the manuscript, in the Part II, we have dealt with the RE studies performed in FTU. In Chapter 3 the **runaway electron diagnostics** used in FTU have been presented, with the main focus on two major recently installed systems: the **Gamma Camera (GC)** and the **Runaway Electron Imaging and Spectrometry (REIS) system**. These are essential tools to study and understand the RE electron behaviour in the experiment, which rely on the radiation and particles emitted by REs when they interact with the plasma species or vessel components. An important amount of work carried out in this thesis has been devoted to the

setting-up and validation of these diagnostics in the FTU tokamak:

Gamma camera

The FTU GC system, described in Sec. 3.2, is based on the detection of the hard X-rays and gammas emitted by the REs along 6 radial lines of sight, perpendicular to the plasma equatorial plane. Discerning the HXR emission originating from the RE bremsstrahlung on the plasma particles across various radial positions provides information on the radial distribution and energy of the incoming radiation, and implicitly, information about the runaway electron energy and location. In this work, radial profiles of the HXR emission have been recovered in several experimental scenarios, confirming the findings that the Dreicer generated REs in FTU emerge in the plasma core and then drift outwards. Furthermore, from the analysis of the high energy tail of the spectra of the detected HXRs, the Gamma camera has allowed to obtain estimates of the maximum runaway energy in the experiment. A more elaborated analysis with spectra unfolding, which would yield knowledge about the RE energy distribution, combined with numerical modelling of the RE dynamics, constitutes a part of ongoing studies. Additionally, the availability of the GC signals has served as a baseline for energy estimates and RE dynamics modelling benchmark in the RE onset/suppression experiments described in Chapter 4, as well as for qualitative comparison with other diagnostic systems.

REIS system

In Sec. 3.3, the REIS system has been introduced as a valuable diagnostic tool collecting the electron synchrotron radiation in the visible and near-infrared range, as well as visible images of the plasma poloidal cross-section, in both runaway forward and backward directions. The detected synchrotron emission coming from in-flight REs directly depends on the energy and momentum-space distribution of the runaway electron population. After the REIS system was calibrated, it has been tested and validated in dedicated FTU experiments.

In this work, with the aim of the REIS diagnostics validation, the following data analysis was performed by comparing the spectra measured in a plasma current flat-top discharge with a substantial amount of REs, generated at the beginning of the discharge, with the spectra calculated for such

a runaway population using two approaches. In the first one, the RE pitch angle and energy distribution function was estimated for the conditions of the discharge using a test particle model of the RE dynamics which takes into account the electron acceleration by the electric field, collisional friction due to the Coulomb interactions with the plasma particles, and electron deceleration caused by the synchrotron radiation losses. The resulting RE distribution was then used as input in the code PySYRUP, which is a numerical tool that calculates the synchrotron emission spectra for a given electron distribution, under a chosen approximation for the electron power emission. In the second approach, a fully monoenergetic RE beam was assumed (traditionally used approach), with the energy corresponding to the maximum electron energy.

The results indicated that, for the stable flat-top discharge, when the modelled runaway distribution tends to be monenergetic later during the current flat-top, the measured spectra are closely fitted with the calculated one using both of the approaches (full distribution function or monoenergetic beam), while in the beginning of the discharge, when the energy distribution function is broad, the full electron distribution function should be considered for the simulation of the synchrotron spectra.

These results constitute an experimental confirmation of the findings by theoretical models of synchrotron emission by runaway electrons that, although the full distribution should not be generally approximated by the monoenergetic one, it could still serve as a simple estimate of the maximum electron energy in specific cases.

On the other hand, supporting research in the field, based on the versatile synthetic synchrotron diagnostics toolkit SOFT, shows that the geometrical effects and the detector placement, beyond the corrections included in the calculations here presented, should be taken into account. These and the remaining open questions regarding the REIS system design and related runaway modelling are being addressed with the ongoing development and upgrade of the system and its supporting framework for use in MST devices with RE campaigns dedicated to ITER relevant questions.

A second major part of the work performed in FTU during this thesis has included the determination of the **threshold (or critical) electric field for runaway electron generation** in flat-top Ohmic discharges (Chapter 4).

The threshold electric field for runaway generation not only constitutes an essential parameter of the runaway physics but it also has a large practical importance as it determines to great extent the amount of impurities that would be required for RE suppression by MGI or SPI during disruptions. The knowledge of the most significant mechanisms affecting the value of this critical parameter is essential for the design of adequate RE mitigation schemes during disruptions in future devices. Through inspection of the FTU database and analysis of dedicated experiments carried out in FTU OH discharges in which RE onset and suppression occurs (by decreasing or increasing the density, respectively), we have found upper and lower bounds for the value of the threshold electric field for runaway generation. In our experiments, the measured value of the critical field, E_{thr}, has been found to be larger by a factor $\sim 2-5$ than the predictions relying on the relativistic classical collisional theory which assumes that the threshold field is determined by the electron collisional losses. These results are consistent with those found in a coordinated ITPA joint experiment performed to measure the critical electric field in different tokamaks, where it has become evident that other energy loss mechanisms (in addition to the collisional losses) must be considered to explain the observed increase of the threshold electric field. Moreover, the experiments carried out in FTU have shown that the measured critical electric fields are in agreement (both in magnitude as well as in the dependence on the plasma parameters) with a new threshold for RE generation estimated including the effect of the electron synchrotron radiation losses (E_R^{rad}). In addition, these findings are also in agreement with the results of RE suppression experiments in FTU by means of ECRH.

However, still a small deviation of the experimental threshold with respect to the radiation critical field (E_R^{rad}) has been observed, $E_{thr} \sim (1-1.7) \times E_R^{rad}$, which would imply that, to a lower degree, other mechanisms are also playing a role in RE energy dynamics, causing a further increase in the threshold electric field. It has been found that these additional losses can be described by a characteristic dissipation time $\sim$ 0.05 - 0.3 s which, if it is assumed to be due to the radial diffusion losses associated with the underlying magnetic turbulence, would result in a radial diffusion coefficient and a magnetic fluctuation level consistent with the turbulence levels found from previous studies in the core region of FTU ohmic discharges. Nevertheless, other loss mechanisms (such as kinetic instabilities) cannot be completely discarded.

All these findings suggest that, for the suppression of runaway electrons

by MGI or SPI, lower amount of impurities might be required than initially expected on the basis of the effect of the collisional losses alone. Nonetheless, whether such results, obtained during the flat-top phase of non-disruptive ohmic discharges in medium size devices, would still hold during disruptions in ITER, is still an open question.

Our final matter of interest in this thesis has been the FTU investigation on the **active control and suppression of post-disruption RE beams**, work done in collaboration with FTU active control team, a brief overview of which can be found in Chapter 5. During disruptions, RE beams can rapidly destabilise and end up interacting with the inner structures of the tokamak, causing serious damage. In FTU, the plasma control system (PCS) has been employed for the radial runaway beam position control, while the beam energy dissipation relies on the inductive action on the RE current from the central solenoid. We have reviewed the results obtained with two recently established real-time algorithms that have successfully withheld the RE beam away from the walls, by controlling the plasma external radius. In these experiments, the PCS has maintained the current reference upon the beam stabilisation, so that the current decrease would occur at a slow enough rate, allowing a safe ramp-down and suppression of the high energy RE beam currents. The second advantageous feature implemented in the FTU PCS framework is the soft-stop trigger which is activated when the predetermined safety levels of HXRs are surpassed, prompting a shut-down control algorithm that manages the references of the plasma current and the inner and outer plasma radii. In Chapter 5, such a case has been validated by the interpretation of the measurements made with the REIS diagnostics. As a stable runaway beam is a prerequisite for RE mitigation through densification, the FTU PCS algorithms have proved to be a reliable foundation for further studies. Furthermore, the main advantages of a well developed and verified PCS could be extended and implemented in future tokamak control systems.

All the experimental work described in this thesis has been carried out in collaboration with the FTU team and has included in all the cases my participation in the planning and design of the experiments, setting-up and validation of the runaway diagnostics and data acquisition, as well as data base elaboration, data analysis and interpretation. The work has been car-

ried out within the framework of the european EUROFUSION projects, WP14-MST2-9, WP15-MST2-15 ("Runaway Electron Studies in FTU"; 2014 - 2016), WP18-MST2-15 ("REIS activities"; 2018), MST1-2017 and MST1-2018 ("Medium Sized Tokamaks"; 2017 and 2018), as well as the Spanish National Projects ENE2012-31753 ("ITER-relevant disruption and runaway electron studies"; 2013 - 2016) and ENE2015-66444-R ("Runaway electron generation, control and dissipation during disruptions: implications for ITER"; 2016 - 2019), all of them ITER oriented.

Conclusiones y trabajo futuro

Esta tesis ha abordado algunas cuestiones centrales relacionadas con los plasmas tokamak, en particular en el tokamak FTU. La tesis se enfoca a problemas de alta prioridad para el proyecto ITER relacionados con los electrones runaway durante disrupciones, dentro de las campañas experimentales del tokamak FTU: el estudio de la energía y la función de distribución de los electrones runaway que combina herramientas numéricas y de diagnóstico, estudios sobre el campo eléctrico crítico para la generación de electrones runaway, y el control activo y supresión de haces de corriente runaway durante disrupciones. Aquí, en la tercera y última parte de la tesis, resumimos las conclusiones más relevantes extraídas de este trabajo y llamamos la atención sobre trabajo futuro y algunas preguntas abiertas.

Después de una revisión de los conceptos básicos y la física de electrones runaway en la Parte I de esta memoria, en la Parte II hemos abordado los estudios de electrones runaway realizados en FTU. En el Capítulo 3 se presentaron los **sistemas de diagnóstico** runaway utilizados en FTU, en particular dos de los principales sistemas recientemente instalados: la **Cámara Gamma** y el **sistema REIS (Runaway Electron Imaging and Spectrometry)**. Ambas son herramientas esenciales para estudiar y comprender el comportamiento de los electrones runaway en el experimento, que se basan en la radiación y partículas emitidas por los electrones runaway cuando interactúan con las especies del plasma o los componentes del tokamak. Una cantidad importante del trabajo realizado en esta tesis se ha dedicado a la configuración y validación de estos diagnósticos en el tokamak FTU:

La Cámara gamma

El sistema de cámara gamma de FTU, descrito en la sección 3.2, se basa en la detección de rayos X duros (HXR) y radiación gamma emitidos por los

electrones runaway, a lo largo de 6 líneas de visión radiales, perpendiculares al plano ecuatorial del plasma. Discernir la emisión de rayos X duros que se origina a partir de la radiación de bremsstrahlung de los electrones runaway al interacción con las partículas del plasma a través de varias posiciones radiales proporciona información sobre la distribución radial y la energía de la radiación emitida e, implícitamente, sobre la energía y la localización de los electrones runaway. En este trabajo, los perfiles radiales de la emisión de rayos X duros se han obtenido en varios escenarios experimentales, confirmando hallazgos previos de que los electrones runaway generados en FTU mediante el mecanismo Dreicer se originan en el centro del plasma y después derivan hacia el exterior. Además, a partir del análisis de la región de alta energía de los espectros de rayos X duros, la cámara gamma ha permitido obtener estimaciones de la energía máxima de los electrones runaway en el experimento. Un análisis más elaborado de los espectros, que proporcionaría información sobre la distribución de energía de los electrones runaway, combinado con el modelado numérico de la dinámica de electrones runaway, constituye un área de estudio actualmente en curso. Además, la disponibilidad de las señales de la cámara gamma ha servido de base para estimaciones de la energía runaway y punto de referencia en el modelo de la dinámica runaway en los experimentos de generación/supresión de electrones runaway descritos en el Capítulo 4, así como para la comparación cualitativa con otros sistemas de diagnóstico.

El Sistema REIS

En la sección 3.3, el sistema REIS se introdujo como una valiosa herramienta de diagnóstico que recoge la radiación sincrotrón de los electrones en el rango visible e infrarrojo cercano, así como imágenes de la sección transversal poloidal del plasma, en ambas direcciones del movimiento de los electrones runaway, hacia adelante y hacia atrás. La emisión sincrotrón detectada proveniente de los electrones runaway "en vuelo" depende directamente de la energía y de la distribución en el espacio de momentos de la población de electrones runaway. Una vez que se calibró el sistema REIS, éste se probó y validó en experimentos dedicados en FTU.

En este trabajo, con el objetivo de validar el sistema REIS, se realizó el siguiente análisis comparando los espectros medidos en una descarga estacionaria con una cantidad sustancial de electrones runaway, generados al inicio de la descarga, con los espectros calculados para esa población runaway

utilizando dos enfoques. En el primero, el ángulo "pitch" de los electrones runaway y la función de distribución de energía se estimaron utilizando un modelo de partícula "test" de la dinámica runaway que tiene en cuenta la aceleración de electrones por el campo eléctrico, la fricción colisional debida a las interacciones culombianas con las partículas de plasma, y la desaceleración de los electrones causada por las pérdidas de radiación sincrotrón. La distribución de los electrones runaway resultante se usó como entrada en el código PySYRUP, que es una herramienta numérica que calcula los espectros de emisión sincrotrón para una distribución de electrones dada, bajo una aproximación elegida para la potencia emitida por los electrones. En el segundo enfoque, se asumió un haz runaway completamente monoenergético (enfoque utilizado tradicionalmente), con una energía correspondiente a la máxima energía de los electrones.

Los resultados indicaron que, para la descarga de corriente plana analizada, cuando la distribución runaway modelada tiende a ser monenergética durante la fase estacionaria, los espectros medidos se ajustan bien al calculado utilizando ambos enfoques (función de distribución completa o haz monoenergético), mientras que al inicio de la descarga, cuando la función de distribución de la energía es ancha, la función de distribución completa de los electrones debe considerarse para la simulación de los espectros de sincrotrón en lugar de la aproximación monoenergética.

Estos resultados constituyen una confirmación experimental de hallazgos previos de los modelos teóricos de la emisión sincrotrón, por lo que, aunque la distribución completa no debe ser generalmente aproximada por la distribución monoenergética, aún podría servir como una estimación simple de la energía máxima de electrones en casos específicos.

Por otro lado, la investigación de apoyo a este campo, basada en el versítil kit de herramientas de diagnóstico sincrotrón sintético SOFT, muestra que los efectos geométricos y la ubicación del detector, aparte de las correcciones incluidas en los cálculos aquí presentados, deben tenerse en cuenta. Estas y otras preguntas relacionadas con el diseño del sistema REIS y el modelado de electrones runaway relacionado, se siguen abordando actualmente a través del desarrollo y actualización continua del sistema y de un marco soporte para su uso en dispositivos MST ("Medium Sized Tokamaks") en las campañas dedicadas a electrones runaway en ITER.

Una segunda parte importante del trabajo realizado en FTU durante esta tesis ha incluido la determinación del **campo eléctrico crítico (umbral) para la generación de electrones runaway** en descargas óhmicas estacionarias (Capítulo 4). El campo eléctrico crítico para la generación runaway no sólo constituye un parámetro esencial de la física runaway, sino que también tiene una gran importancia práctica, ya que determina en gran medida la cantidad de impurezas que se necesitarían para la supresión de electrones runaway mediante MGI o SPI durante disrupciones. El conocimiento de los mecanismos más importantes que afectan el valor de este parámetro crítico es esencial para el diseño de esquemas adecuados de mitigación de electrones runaway durante disrupciones en futuros dispositivos. A través de la inspección de las bases de datos en FTU y del análisis de los experimentos dedicados realizados, en los que se generan o suprimen electrones runaway (disminuyendo o aumentando la densidad, respectivamente), hemos encontrado cotas superiores e inferiores para el valor del campo eléctrico umbral para la generación de electrones runaway. En nuestros experimentos, se ha encontrado que el valor medido del campo crítico, E_{thr}, es mayor en un factor $\sim 2-5$ que las predicciones basadas en la teoría clásica colisional relativista de electrones runaway que supone que el campo crítico está determinado por las pérdidas de energía colisionales de los electrones. Estos resultados son consistentes con los encontrados en un experimento coordinado conjunto del grupo ITPA en MHD y disrupciones de ITER realizado para medir el campo eléctrico crítico en diferentes tokamaks, donde se ha hecho evidente que se deben considerar otros mecanismos de pérdida de energía (además de las pérdidas colisionales) para explicar el aumento observado del campo eléctrico crítico. Además, los experimentos llevados a cabo en FTU han demostrado que los campos eléctricos críticos medidos están de acuerdo (tanto en magnitud como en la dependencia de los parámetros de plasma) con un nuevo campo eléctrico umbral para la generación de electrones runaway que incluye el efecto de las pérdidas debidas a la radiación sincrotrón del electrón (E_R^{rad}). Por otro lado, estos hallazgos también están de acuerdo con los resultados de experimentos de supresión de electrones runaway en FTU por medio de ECRH.

No obstante, se han observado en algunos casos pequeñas desviaciones del umbral experimental con respecto al campo crítico de radiación (E_R^{rad}), $E_{thr} \sim (1-1.7) \times E_R^{rad}$, que implicaría que, en un grado menor, otros mecanismos también están afectando la dinámica de la energía de electrones runaway,

causando un incremento adicional en el campo eléctrico umbral. Se ha encontrado que estas pérdidas adicionales se pueden describir mediante un tiempo de disipación característico $\sim$ 0.05 - 0.3 s que, si se supone que se debe a las pérdidas de difusión radial asociadas con la turbulencia magnética subyacente, daría lugar a una coeficiente de difusión y un nivel de fluctuación magnética consistente con los niveles de turbulencia encontrados en estudios previos en la región central de las descargas óhmicas en FTU. Sin embargo, otros mecanismos de pérdida (como las inestabilidades cinéticas) no se pueden descartar por completo.

Todos estos hallazgos sugieren que, para la supresión de electrones runaway mediante MGI o SPI en una disrupción, podría requerirse una cantidad menor de impurezas que las esperadas inicialmente sobre la base del efecto de las pérdidas por colisión solamente. No obstante, si estos resultados, obtenidos durante la fase estacionaria de descargas óhmicas (no disruptivas) en dispositivos de tamaño medio, se mantendrían durante disrupciones en ITER, sigue constituyendo una pregunta todavía abierta.

Nuestro último punto de interés en esta tesis ha sido la investigación en FTU sobre el **control activo y la supresión de haces de electrones runaway creadas durante disrupciones**, trabajo realizado en colaboración con el equipo de control activo de FTU, y que se resume brevemente en el Capítulo 5. Durante las disrupciones, los haces de electrones runaway creados pueden desestabilizarse rápidamente y terminar interactuando con las estructuras internas del tokamak, causando graves daños. En FTU, el sistema de control del plasma (PCS) se ha usado para el control de la posición radial del haz, mientras que la disipación de la energía del haz se basa en la acción inductiva sobre la corriente runaway del solenoide central. Hemos revisado los resultados obtenidos con dos algoritmos en tiempo real recientemente instalados que han mantenido exitosamente el haz de electrones runaway lejos de las paredes, controlando el radio externo del plasma. En estos experimentos, el PCS ha mantenido la referencia actual sobre la estabilización del haz, de modo que la disminución de la corriente se produciría a una velocidad suficientemente lenta, permitiendo una caída segura y la supresión de la corriente runaway de alta energía. La segunda característica ventajosa implementada en el marco del PCS en FTU es el disparador de "caída suave" de la corriente ("soft-stop") que se activa cuando se superan los niveles de seguridad predeterminados de los rayos X duros, lo que provoca

un algoritmo de control de apagado que administra las referencias de la corriente del plasma y de los radios interno y externo del plasma. En el Capítulo 5, tal caso ha sido validado mediante interpretación de las medidas realizadas con el diagnóstico REIS. Como un haz runaway estable es un requisito previo para la mitigación de electrones runaway mediante densificación, los algoritmos PCS de FTU han demostrado ser una base fiable para futuros estudios. Además, las principales ventajas de un PCS bien desarrollado y verificado podrían extenderse e implementarse en futuros sistemas de control.

Todo el trabajo experimental descrito en esta tesis se ha llevado a cabo en colaboración con el equipo de FTU y ha incluido en todos los casos mi participación en la planificación y diseño de los experimentos, la puesta a punto y validación de los diagnósticos runaway y adquisición de datos, así como la elaboración de bases de datos, análisis e interpretación de datos. El trabajo se llevó a cabo en el marco de los proyectos europeos de EUROFUSION, WP14-MST2-9, WP15-MST2-15. ("Runaway Electron Studies in FTU"; 2014 - 2016), WP18-MST2-15 ("REIS activities"; 2018), MST1-2017 y MST1-2018 ("Medium Sized Tokamaks"; 2017 y 2018), así como los proyectos nacionales españoles ENE2012-31753 ("Estudios sobre electrones runaway y disrupciones relevantes para ITER"; 2013 - 2016) y ENE2015-66444-R ("Generación, control y disipación de electrones runaway durante disrupciones: implicaciones para ITER"; 2016 - 2019), todos ellos orientados a ITER.

Bibliography

[1] United Nations Department of Economic and Social Affairs. World population prospects: The 2017 revision, 2017.

[2] G. Kaye and T. Laby. Tables of physical and chemical constants. *(London: Longman), p 546 and following*, 1995.

[3] ENEA Frascati official website.

[4] B. Esposito L. Boncagni P. Buratti et al. *Plasma Phys. Controlled Fusion* **59***, 014044*, 2017.

[5] H. Dreicer. *Phys. Rev.* **115***, 238* (1959); **117***, 329* (1960).

[6] C.T.R. Wilson. *Proc. Cambridge Philos. Soc.* **42***, 534*, 1925.

[7] V.V. Matveev et al. *Sov. Phys.-Tech. Phys.* **8***, 530*, 1963.

[8] J. Wesson. *Tokamaks*. Oxford Science Publications, 4^{th} Edition, 2011.

[9] F. Andersson. *Runaway electrons in tokamak plasmas*. PhD thesis, Chalmers University of Technology, 2003.

[10] J.W. Connor and R.J. Hastie. *Nucl. Fusion* **15***, 415*, 1975.

[11] R. Jayakumar H.H. Fleischmann and S.J. Zweben. *Phys. Lett. A* **172***, 447*, 1993.

[12] I. Fernández Gómez. *Generación y dinámica de electrones runaway en plasmas tokamak*. PhD thesis, Universidad Carlos III de Madrid, 2013.

[13] R.M. Kulsrud Y. Sun N.K. Winsor and H.A. Fallon. *Phys. Rev. Lett.* **31***, 690*, 1973.

[14] H. Knoepfel and D.A. Spong. *Nucl. Fusion* **19**, *785*, 1979.

[15] M.N. Rosenbluth and S.V. Putvinski. Theory for avalanche of runaway electrons in tokamaks. *Nucl. Fusion* **37**, 1997.

[16] L.-G.Eriksson P. Helander F. Andersson D. Anderson and M. Lisak. *Phys. Rev. Lett.* **92**, *205004*, 2004.

[17] H.M. Smith and E. Verwichte. Hot tail runaway electron generation in tokamak disruptions. *Phys. Plasmas* **15**, *072502*, 2008.

[18] J.R. Martín-Solís A. Loarte and M. Lehnen. *Nucl. Fusion* **57**, *066025*, 2017.

[19] J.R. Martín-Solís J.D. Alvarez R. Sánchez and B. Esposito. *Phys. Plasmas* **5**, *2370*, 1998.

[20] J.C. Wiley et al. *Physics of Fluids* **23** *(11), 2193*, 1980.

[21] V. Fuchs et al. *Physics of Fluids* **29** *(9), 2931*, 1986.

[22] G. Fussmann. *Nuclear Fusion* **19** *(3), 327*, 1979.

[23] D. Mosher. *Phys. Fluids* **18**, *846*, 1975.

[24] J. Schwinger. On the classical radiation of accelerated electrons. *Physical Review* **75** *(12), 1912*, 1949.

[25] B. Kurzan et al. Dynamics of runaway electrons in the magnetic field of a tokamak. *Physical Review Letters* **75** *(25), 4626*, 1995.

[26] I.B. Bernstein and D.C. Baxter. *Physics of Fluids* **24**, *108*, 1981.

[27] J.R. Martín-Solís R. Sánchez and B. Esposito. *Phys. Plasmas* **7**, *3814*, 2000.

[28] J.R. Martín-Solís R. Sánchez and B. Esposito. *Phys. Rev. Lett.* **105**, *185002*, 2010.

[29] L. Laurent and J.M. Rax. *Europhys. Lett.* **11**, *219*, 1990.

[30] International Atomic Energy Agency Vienna. Iter eda agreement protocol 2, 1994.

[31] Y. Kawano et al. *Contr. Fusion Plasm. Phys.* **21A**, *501*, 1997.

[32] J.R. Martín-Solís R. Sánchez and B. Esposito. *Phys. Plasmas* **6**, *3925*, 1999.

[33] A.B. Rechester and M.N. Rosenbluth. *Phys. Rev. Lett.* **40**, *38*, 1978.

[34] J.A. Wesson et al. *Nucl. Fusion* **29**, *641*, 1989.

[35] R. Yoshino. *J. Nucl. Mater.* **220-222**, *132*, 1995.

[36] E.M. Hollmann et al. *Phys. Plasmas* **22**, *021802*, 2015.

[37] M. Lehnen et al. *J. Nucl. Mater.,* **39 - 48**, *463*, 2015.

[38] I. Fernández Gómez J.R. Martín-Solís and R. Sánchez. *Phys. Plasmas* **14**, *072503*, 2007.

[39] V. Lukash et al. *Proc. 40th EPS Conf. Plasma Physics P5.167*, 2013.

[40] E.M. Hollmann et al. *Nucl. Fusion* **53**, *083004*, 2013.

[41] O. Tudisco et al. *Chapter 8: The diagnostic systems in the FTU, Fusion Science and Technology* **45**, *402*, 2004.

[42] R. Jaspers. *Relativistic runaway electrons in tokamak plasmas.* PhD thesis, Technische Universiteit Eindhoven, 1995.

[43] L. Bertalot et al. *Rev. Sci. Instrum.* **63**, *4554*, 1992.

[44] B. Esposito et al. *Phys. Plasmas* **10**, *2350*, 2003.

[45] D. Marocco et al. *Fusion Engineering and Design* **96-97**, *852*, 2015.

[46] M. Riva. *Fusion Engineering and Design* **88**, *1178*, 2013.

[47] F. Causa et al. *Rev. Sci. Instrum., accepted for publication*, 2019.

[48] B. Esposito et al. *Proc. 43rd EPS Conf. on Plasma Physics (Leuven, 2016)*, 2016.

[49] D. Marocco et al. *IEEE Trans. Nucl. Sci.* **56**, *1168*, 2009.

[50] B. Esposito et al. *Plasma Phys. Controlled Fusion* **38**, *2035*, 1996.

[51] Y. Peysson et al. *Nucl. Fusion* **33**, *1233*, 1993.

[52] G. Bekefi. *Radiation processes in plasmas*. Wiley, 1966.

[53] G.B. Rybicki and A.P. Lightman. *Radiative processes in astrophysics*. Wiley, 1985.

[54] A. Stahl et al. *Phys. Plasmas* **20**, *093302*, 2013.

[55] I.M. Pankratov. *Plasma Phys. Rep.* **25**, *145*, 1999.

[56] M. Gospodarczyk. *Control, diagnostics and estimation techniques for runaway electrons beams*. PhD thesis, Università degli studi di Roma "Tor Vergata", 2018.

[57] J.H. Yu. *Phys. Plasmas* **20**, *042113*, 2013.

[58] M. Hoppe et al. *Nucl. Fusion* **58**, *026032*, 2018.

[59] A. Perek. Time evolution of the runaway electron energy distribution in a runaway plateau in asdex-u. Master's thesis, Technische Universiteit Eindhoven, 2017.

[60] D.G. Whyte et al. *Phys. Rev. Lett.* **89**, *055001*, 2002.

[61] R.S. Granetz et al. *Phys. Plasmas* **21**, *072506*, 2014.

[62] R. Andreani et al. *Proc. 16th Symp. on Fusion Technology (North-Holland, Amsterdam, 1990), Vol. 1, p. 218*, 1990.

[63] A. Stahl et al. *Phys. Rev. Lett.* **114**, *115002*, 2015.

[64] P. Aleynikov and B.N. Breizman. *Phys. Rev. Lett.* **114**, *155001*, 2015.

[65] P. Aleynikov et al. *in Fusion Energy 2014 (Proc. 25th Int. Conf., St. Petersburg, 2014) (Vienna: IAEA) CD-ROM file TH/P3-38*, 2014.

[66] J.R. Martín-Solís A. Loarte and M. Lehnen. *Phys. Plasmas* **22**, *092512*, 2015.

[67] R. Yoshino and S. Tokuda. *Nucl. Fusion* **40**, *1293*, 2000.

[68] S. Putvinski et al. *Plasma Phys. Controlled Fusion* **39**, *B157*, 1997.

[69] I. Entrop et al. *Plasma Phys. Controlled Fusion* **40**, *1513*, 1998.

[70] H.E. Mynick and J.D. Strachan. *Phys. Fluids* **24**, *695*, 1981.

[71] J.R. Myra and P.J. Catto. *Phys. Fluids B* **4**, *176*, 1992.

[72] D. Carnevale et al. *Proc. 44th EPS Conf. on Plasma Physics, P1.152*, 2017.

[73] N.W. Eidietis et al. *Proc. 45th EPS Conf. on Plasma Physics, O3.107*, 2018.

[74] M. Lehnen et al. *Phys. Rev. Lett.* **100**, *255003*, 2008.

[75] G. Papp et al. *Nucl. Fusion* **51**, *043004*, 2011.

[76] A. Matsuyama et al. *Proc. of the 12th Asia Pacific Physics Conf. (APPC12) JPSCP.1.015037*, 2013.

[77] N.W. Eidietis et al. *Phys. Plasmas* **19**, *056109*, 2012.

[78] J.A. Snipes et al. *Fusion Eng. Des.* **89**, *507*, 2014.

[79] P.B. Aleynikov et al. *Proc. 37th EPS Conf. Plasma Physics P1.1004*, 2010.

[80] D. Carnevale et al. *Plasma Phys. Controlled Fusion* **61**, *014036*, 2019.

[81] L. Boncagni et al. *Fusion Eng. Des.* **89**, *204*, 2014.

[82] A. Astolfi et al. *22nd Mediterranean Conf. Control and Automation p 1088*, 2014.

[83] M. Ariola and A. Pironti. *Magnetic Control of Tokamak Plasmas (London: Springer)*, 2008.

[84] L. Boncagni et al. *IEEE Trans. J. Nucl. Sci.* **58**, *1778*, 2011.

[85] L. Boncagni et al. *Fusion Eng. Des.* **87**, *1917*, 2012.

[86] D. Carnevale et al. *Proc. Int. IAEA Conf.*, 2016.

[87] C. Cianfarani et al. *Proc. 40th EPS Conf. on Plasma Physics, P5.165*, 2013.